Lancaster University

PhD Thesis

Terahertz magnonics in antiferromagnetic iron oxides

by

Ruben A. Leenders

Supervisor:
Dr. Rostislav V. Mikhaylovskiy

This thesis is submitted for the degree of
Doctor of Philosophy

February 2024

Abstract

Antiferromagnets, magnetic materials with antiparallel spin ordering and therefore lacking magnetic moment have for a long time been studied for academic interest only. However, the realization that antiferromagnets possess intrinsic magnetic resonance frequencies in the Terahertz range, which is orders of magnitude higher than the Gigahertz ferromagnetic resonance frequencies, has recently renewed the interest for antiferromagnets for applications in energy efficient data storage and processing.

Moreover waves of spin precession, or magnons, have been proposed as new methods for wave-based computing. The miniaturization of such potential technological devices requires the spin waves to have nanometer scale wavelengths, which has proven to be challenging to achieve in anitferromagnets.

In this thesis, we will study the ultrafast spin dynamics and magnons in a specific class of antiferromagnetic iron oxides, the orthoferrites, $RFeO_3$, where R is a rare-earth element. These antiferromagnets possess a weak ferromagnetic moment due to the canting of the antiparallel spins.

After introducing the field of ultrafast magnetism and magnonics and associated concepts in Chapter 1, in the first part of this thesis, we will describe how the challenge of generating nanoscale spin waves can be overcome by exciting a confined region of spins near the sample face. We will show how strongly absorbed laser pulses will generate a propagating broad-band wavepacket of spin waves.

In Chapter 2, we will introduce the basic concepts behind the experiments performed in this work. We will introduce the principle of ultrafast pump-probe spectroscopy experiments that can be used to measure such spin waves, and describe the design of the setup that allows us to drive the spin dynamics with intense Terahertz pulses.

In Chapter 3, a thorough theoretical description of the technique to launch propagating broadband wavepackets of magnons will be given. Additionally, we will model the detection of these generated packets of spin waves acts in Magneto-Optical Kerr Effect experiments. We find that through the emergence of the Brillouin condition, by the appropriate choice

of the wavelength of the probe pulse, we can select the detected wavenumber component of the wave packet, resulting in a probe wavelength dependent frequency observed in the experiment.

In Chapter 4, we proceed to the experiment and search for the spin wave packets in $HoFeO_3$. We will show that by exciting the spin dynamics with high energy photons above the bandgap energy, we can launch such propagating packets of spin waves. We find the theoretically predicted dependence of the detected magnon frequency on the wavelength of the probe light, and find that we excite a broad range of components of the spin wave packet.

In Chapter 5, we build upon the experiment in Chapter 4, and study how the propagating spin waves can be controlled. We find that we can achieve a nonlinear control of the spin waves by introducing a second pump pulse. From theoretical calculations, we show that the coupling between the propagating magnon and photon acts as an additional nonlinear torque on the spins. We will see that this nonlinear torque allows for the conversion of the low frequency uniform precession mode of the spins into the higher frequency and higher wavenumber modes of the propagating spin wave packet.

In Chapter 6, we will study the spin dynamics in $ErFeO_3$ and $TmFeO_3$ induced by intense THz pulses. Despite the magnetic similarities of these materials, the spin dynamics shows a very different trend at the Spin Reorientation Transition temperatures. In $ErFeO_3$, we observe an unexpected giant enhancement of the amplitude, whereas in $TmFeO_3$, this amplitude is suppressed. We will show that this difference in the dynamics can be attributed to the effect of the coupling between the iron spins and rare-earth ions.

Finally, in Chapter 7, we will conclude our findings, and provide a concise outlook that shows that the intense THz setup is not only suitable for the study of antiferromagnetic oxides, but can also be used to study metallic thin films. We will demonstrate this with a short summary of experimental data measured in the FeRh, which is an antiferromagnet at room temperature and exhibits a phase transition to the ferromagnetic phase at high temperatures.

Acknowledgements

There are many people I wish to acknowledge, without whom the work in this thesis would not have been possible. First and foremost, I would like to express my sincere gratitude to my supervisor Rostislav Mikhaylovskiy for giving me the opportunity to perform this research and his supervision. Rostislav, it has been an honour to be your first PhD student in Lancaster, and it has been a very instructive and challenging experience to build the intense THz setup from scratch. I learned a lot from your expertise in the combination of theory and experiment. Thank you for all your support and guidance during this work.

Also, I am very grateful to Dima Afanasiev and Alexey Kimel, for their collaboration, and having me back in their group in Radboud University in Nijmegen to give me the opportunity to perform the spin wave experiments. Although the experiments did initially not go according to plan and took quite a while longer than we anticipated, I appreciate your patience, and am glad that after all the efforts, the experiments resulted in some interesting results. Dima, thank you for all your experimental help and guidance, and Sergey Semin and Chris Berkhout, many thanks for your technical support during these experiments. All other colleagues at the Radboud University, thank you for welcoming me back into the group.

The lab work in Lancaster became a lot more enjoyable with the expansion of the research group. Farhan Kholid, Oleksandr Kovalenko, Yuichi Saito, Nikolay Vovk, thank you for all your assistance and contributions to the improvements of the experiment, and always being available when I needed some extra hands during the alignment. Rajasekhar Medapalli, thank you for having me collaborate on the FeRh measurements, I am glad they yielded some nice results. I always enjoyed all of your company in the lab, but also outside the lab, for example on trips and conferences. It has been a great pleasure to work with all of you.

I would also like to acknowledge my deputy supervisor Steven Jamison, and Connor Mosley for sharing their advice with the intense THz setup, and lending us the THz camera for testing our alignment. I am grateful to Kirill Grishunin and Thomas Blank as well, for sharing their tips for the intense THz setup, and to Jorrit Hortensius, for sharing his experience with the spin wave experiment and the collaboration leading to the interesting first publication.

I am also indebted to the team from the mechanical workshop and electronics workshop in the department for their contributions to setting up the experiment, and for their nice design of the cryostat holder and setup enclosures.

I should thank my other colleagues in the office as well, especially during my start in Lancaster. The movie nights and the occasional Friday evening board games made me quickly feel welcome in the department. It is a pity that the pandemic and long lockdowns put an abrupt stop to it.

Saba Khan, I am glad you were my house- and office-mate specifically during our first year. Our regular walks around campus during the lockdowns and the times we cooked together helped to get through the long days of working from home. I am happy we continued this occassionally even after the lockdowns.

Dominic Shea, thank you for joining in the enjoyable visits to the baking society and sharing your contagious passion for physics.

Last but not least, I would like to thank my parents, William and Annette, and my brothers, Lars and Olaf. Besides their unconditional love and support, I feel lucky that I could stay with them during my time back in Nijmegen. Without them, the extended duration of the experiments in Nijmegen, and thus a major part of the work in this thesis, would not have been possible.

The research presented in this thesis was in part supported by ERC grant 852050 MAGSHAKE.

Declaration

I declare that this thesis, titled "Terahertz magnonics of antiferromagnetic oxides" is entirely my own work, unless specified otherwise in the form of quotations, and has not been submitted for any other academic award. The work presented in this thesis has resulted in or contributed to the following publications or publications in preparation at the time of writing:

- **Chapter 3**: J.R. Hortensius, D. Afanasiev, M. Matthiesen, R. Leenders, R. Citro, A.V. Kimel, R.V. Mikhaylovskiy, B.A. Ivanov, and A.D. Caviglia, "Coherent spin-wave transport in an antiferromagnet", *Nature Physics*, vol. 17, no. 9, pp. 1001-1006 (2021).
- **Chapter 3**: R.A. Leenders and R.V. Mikhaylovskiy, "Theory of optical generation and detection of propagating magnons in an antiferromagnet", *Physical Review B*, vol. 107, no. 9, p. 094423 (2023).
- **Chapter 4 and 5**: R.A. Leenders, D. Afanasiev, A.V. Kimel and R.V. Mikhaylovskiy, "Altermagnetic platform for ultrafast optical conversion of magnons", *(under review)*
- **Chapter 6**: R.A. Leenders et. al, "Enhanced antiferromagnetic THz-driven spin dynamics in the Spin Reorientation Transition in $ErFeO_3$", *(in preparation)*
- **Chapter 7**: R. Medapalli et. al, *(in preparation)*

Ruben Leenders
February 2024

Contents

List of Abbreviations

AFMR	antiferromagnetic resonance
arb. u.	arbitrary units
BBO	beta Barium Borate
cm	centimeter
emu	electromagnetic unit
(I)CME	(inverse) Cotton-Mouton effect
(I)FE	(inverse) Faraday effect
DFG	difference frequency generation
DMI	Dzyaloshinskii-Moriya Interaction
Dy	Dysprosium
$DyFeO_3$	Dysprosium Orthoferrite
EOS	electro-optic sampling
Er	Erbium
eV	electronvolt
$ErFeO_3$	Erbium Orthoferrite
fs	femtosecond
FWHM	full width at half maximum
G	Gauss
GaP	Gallium Phosphide
GHz	gigahertz
Ho	Holmium
$HoFeO_3$	Holmium Orthoferrite
IR	infra-red
K	Kelvin
km	kilometer
kHz	kilohertz
kV	kilovolt

$LiNbO_3$	Lithium Niobate
LLG	Landau-Lifshitz-Gilbert
mm	millimeter
mJ	milliJoule
nm	nanometer
MV	megavolt
MgO	Magnesium Oxide
MOKE	magneto-optical Kerr effect
OR	optical rectification
OPA	optical parametric amplifier
ps	picosecond
q-AFM	quasi-antiferromagnetic
q-FM	quasi-ferromagnetic
RE	rare-earth
$RFeO_3$	rare-earth orthoferrite
SFG	sum frequency generation
SH(G)	second harmonic (generation)
T	Tesla
THz	terahertz
Tm	Thulium
$TmFeO_3$	Thulium Orthoferrite
SRT	spin reorientation transition
$\lambda/2$	half wave plate
$\lambda/4$	quarter wave plate
μm	micrometer
μJ	microJoule
2D	2 dimensional

List of symbols

a	isotropic exchange coupling between iron and rare earth spins
A_f	amplitude of freely propagating spin wave
A_p	amplitude of driven precession
B	anisotropic exchange coupling between iron and rare earth spins
c	speed of light
$\mathbf{c}$	antiferromagnetic moment components of rare-earth system (Ch. 6)
d	excitation depth
D	Dzyaloshinskii-Moriya
E	electric field
f	frequency (focal length in Ch. 2)
$\mathbf{f}$	weak ferromagnetic components of rare-earth system (Ch. 6)
f_0	uniform antiferromagnetic resonance frequency
f_k	frequency of propagating magnon mode with wave number k
$\mathbf{F}$	weak ferromagnetic moment components of iron system (Ch. 6)
$\mathbf{G}$	antiferromagnetic moment components of iron system (Ch. 6)
h	effective field
H	magnetic field
I	intensity
J	exchange integral
k_{sw}	magnon wavenumber
K	anisotropy constants
L	thickness
$\mathbf{l}$	dynamic component of antiferromagnetic vector
$\mathbf{L}$	antiferromagnetic vector

$\mathbf{M}$	magnetization/weak ferromagnetic moment
$\mathbf{m}$	dynamic component of (weak) ferromagnetic vector
n	refractive index
p	grating periodicity
q	beam parameter
r_{41}	nonlinear optical coefficient of GaP
$\mathbf{S}$	spin
t	time (transmission coefficient in 2.3.5)
T	temperature
U	pulse energy
V	voltage (Verdet constant in Ch. 1.3.1)
W	free energy density
z	spatial coordinate
α	damping parameter (or polarization angle in Ch. 2.3.5)
β	excitation lifetime
γ	gyromagnetic ratio (or pulse tilting angle in Ch. 2.3.2)
ϵ	permittivity
θ_0	angle of weak ferromagnetic moment and a-axis
θ_F	Faraday rotation angle
θ_K	Kerr rotation angle
ϕ	spin deflection angle
λ	wavelength
λ_i	exchange constants in rare-earth system (Ch. 6)
$\boldsymbol{\mu}$	magnetic moment
μ_0	magnetic permeability
ξ	pinning parameter
τ	time delay between two pump pulses (Ch. 5) (or Gaussian FWHM in Ch. 3)
χ	susceptibility
$\omega = 2\pi f$	angular frequency
Ω	frequency with respect to pump delays
$\mathscr{F}$	magnetic free energy density
$\Delta\mathscr{T}$	dynamic torque of rare-earth system on iron system
$\mathscr{L}$	Lagrangian

Chapter 1

Introduction

Magnetism has been fascinating mankind ever since the ancient Greek times [1]. The origin of the attractive (or repulsive) forces between certain materials has been a mystery for tens of centuries afterward, but the attractive forces in an external magnetic fields have already long ago been exploited for the development of, for example, compasses. In the 19th century, great progress in the understanding of electromagnetism was made, and it was understood that magnetism was intrinsically related to electricity. This relation was summarized in the Maxwell's equations.

A breakthrough in the understanding of the origin of magnetism was made in the early 20th century, with the discovery of quantum mechanics [2]. It is now known that magnetism originates from electrons, that carry an intrinsic magnetic moment, that is referred to as spin. The electron spins can order in a variety of ways, giving rise to a wide range of classes of magnetic materials, which are illustrated in figure 1.1. The best known magnetic materials are the ferromagnets, in which the electron spins order parallel with respect to each other. This gives rise to a macroscopic magnetization.

On the other hand, if the spins are aligned in an antiparallel manner and carry compensating magnetic moments, the material is referred to as an antiferromagnet. If the antiparallel aligned spins do not compensate each other, a small magnetic moment remains. Materials in which this occurs are referred to as ferrimagnets. Very recently, a new class of magnetic materials was proposed, which is referred to as altermagnets [3]. The symmetry of these materials is such, that the spin order is not only staggered in the coordinate space, but also in the momentum space, resulting in the splitting of dispersion relations for opposite chiralities of spin precession (see also section 1.7 for a more detailed description on the magnon dispersion relations). Similar to the antiferromagnets, the ordering is antiparallel, but the material exhibits many interesting properties that would otherwise be typical for

ferromagnets. For instance, despite the lack of a magnetic moment, altermagnets may exhibit strong magneto-optics [4] (see section 1.3 for a description of magneto-optics).

The materials that are studied in this thesis, the rare-earth orthoferrites, are proposed to be examples of such altermagnets [5]. The spin ordering of the orthoferrites is antiferromagnetic with a small canting of the magnetic sublattices with each other, resulting in a weak ferromagnetic moment.

In contrast, in the paramagnets, all spins point in random directions. Therefore, all microscopic magnetic moments average out, resulting in the lack of a macroscopic magnetic moment. The magnetic order in such materials occurs only in the presence of an external magnetic field [6].

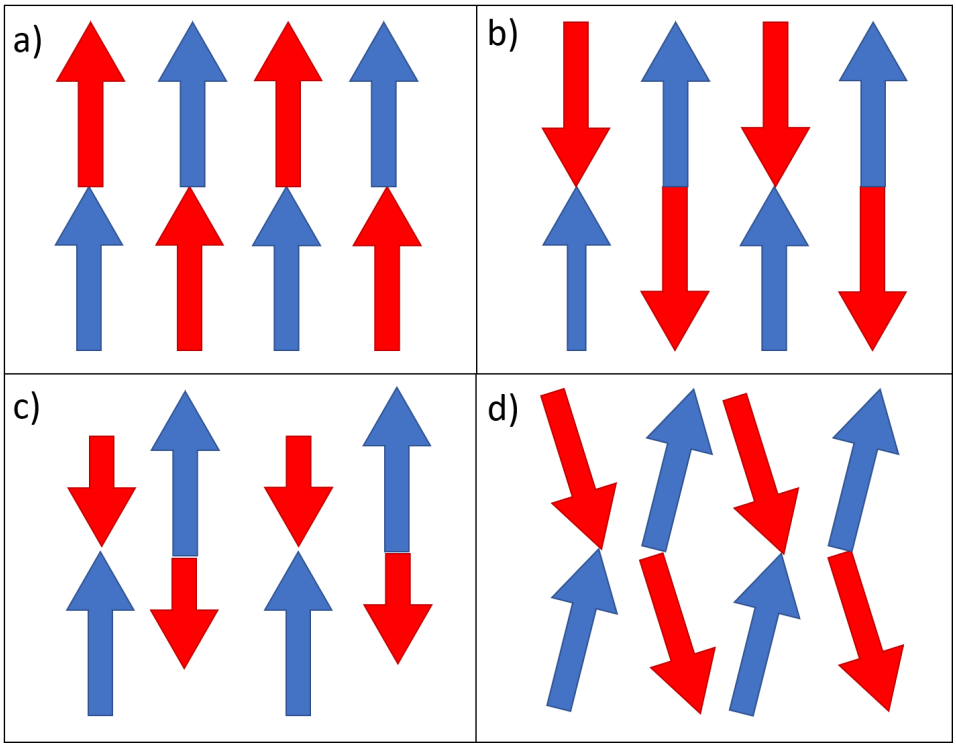

Figure 1.1: Illustration of the ordering of the magnetic moments for a) a ferromagnet, b) an antiferromagnet, c) an ferrimagnet, d) a weak ferromagnet. The arrows and colors represent the orientations of the spins on the different sublattices.

Now, the magnetically ordered materials (in particular the ferromagnets) are at the core of the current technologies for data storage and processing. This chapter will start by highlighting the relevance of magnetism for data processing, and will sketch a general background of the field of ultrafast magnetism. Moreover, some of the fundamental concepts that will be required throughout this thesis will be introduced here.

1.1 Magnetism for data technology

Over the past decades, the fast developments of modern technologies, specifically in the Information (Communication) Technologies, cause data centers to be rapidly rising from the ground [7]. As a result of this increasing demand for data storage and processing, the global energy usage by such data centers is rapidly increasing [8]. This increasing energy consumption is therefore increasingly contributing to the emission of greenhouse gasses [9], and extensive research is going on to reduce the power consumptions of these centers [10].

Thus far, this rapid development has been supported by improving technologies that allow the creation of the smallest computing components, transistors, to ever smaller sizes [11]. Already decades ago, shortly after the invention of the first computing devices, Moore saw an exponential increase in the number of computing units on chips over time, which is the now well known Moore's Law [12]. The smallest feature sizes for the transistors are currently diving below 10 nanometers, thus getting closer and closer to the atomic length scales [13]. Hence, the miniaturization seems to be approaching fundamental limits. Moreover, these small sizes suffer from enormous electric dissipation with the risk of overheating [14], and new fast and energy efficient technologies will be required to continue increasing computing power and speeds.

As a result, a lot of research has been performed to find new ways to manipulate magnetic moments, besides the conventional magnetic fields. This has for instance led to the development of the field of spintronics, which includes spin degree of freedom into electronics [15]. In the field of magnonics, it has been proposed that information can be stored and manipulated with spin waves [16]. However, to efficiently control magnetism on short time scales, ultrafast stimuli are required, that cannot be achieved with conventional electronic current pulses.

The rapid advances in laser technologies in the second half of the last century have given access to ultra-short laser pulses, with durations down to the femtosecond range, by using mode locked laser systems [17]. Ever since, many research fields have rapidly developed, exploiting these ultrashort laser pulses to study the interaction of the electromagnetic light with materials at ultrashort time scales and probe diverse physical phenomena with up to femtosecond or even attosecond resolution [18]. Among these many fields of research is ultrafast magnetism.

The progress in ultrafast magnetism could possibly provide solutions for this current challenge of highly energy efficient and fast data storage and processing. For example, it has already been shown over the last decades that it is possible to manipulate magnetic moments using such short light pulses, and even switch the orientation of the magnetic moments. In

the typical data technology used nowadays, the orientation of the magnetic moments would correspond to the switching of a bit of information from a '0' state to a '1' state. Typically, high magnetic fields are required to achieve this conversion of states, which would require high currents and high energetic losses. Controlling magnetism with light has been shown to be more energy efficient [19], and the availability of light pulses with ultra-short duration allows for the ultrafast control of magnetism.

The following section will highlight the background of the field of ultrafast magnetism in more detail.

1.2 Ultrafast magnetism

It was only shortly after the development of the mode-locked laser [20] that the field of ultrafast magnetism emerged. It was soon realized that the properties of materials, among which magnetism, can be controlled with the electromagnetic field of light. Nowadays, it is widely recognized that the field of ultrafast magnetism was born by the discovery of the ultrafast demagnetization in a ferromagnet [21]. The time-scale at which this demagnetization occurred triggered a wide debate on the physics behind the control of the magnetization at such sub-picosecond timescales. Soon after this discovery, extensive research has been performed and a wide variety of ways to control magnetism were observed [22]. Examples of this include the generation of coherent spin precession [23], light-induced spin reorientation in antiferromagnets [24], or even complete changes in the magnetic ordering, as demonstrated by the laser-induced phase transitions from an antiferromagnetic to ferromagnetic phase [25].

The ultrafast dynamics of spins could be well understood by the fact that the electron carries intrinsic angular momentum **S**, also referred to as spin, giving rise to a magnetic moment $\boldsymbol{\mu} = \gamma \mathbf{S}$, where γ is the gyromagnetic ratio. The time evolution of this angular momentum is given by the torque that the external magnetic field exerts on the spins. This realization resulted in the Landau-Lifshitz equations, which reads in the simplest form (in the CGS or Gaussian system of units) [22]

$$\frac{d\mathbf{M}}{dt} = -\gamma \mathbf{M} \times \mathbf{H} + \alpha \mathbf{M} \times \frac{d\mathbf{M}}{dt}, \tag{1.1}$$

where **M** is the magnetization, **H** is the magnetic field and α is a constant accounting for the damping of the precession. This equation describes the precession of magnetization around a magnetic field, as illustrated in figure 1.2.

Moreover, a lot of research is going on in the direction of the all-optical magnetization

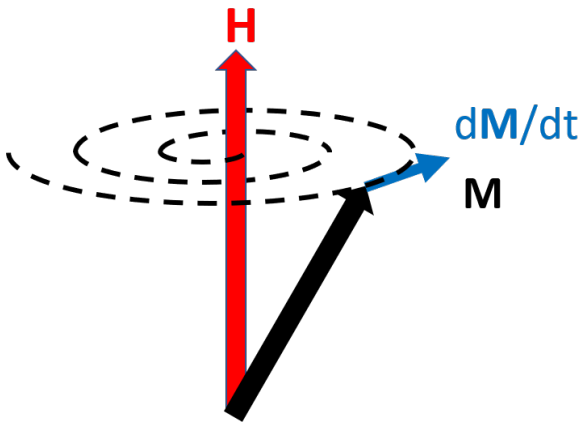

Figure 1.2: Depiction of the Landau-Lifshitz equation of the precession of magnetization **M** (black arrow) around a magnetic field **H** (red arrow). The rate of change of the magnetization orientation d**M**/dt is tangent to the dashed trajectory (blue arrow).

reversal in ferromagnets [26], and ferrimagnets [27], which has yielded results with a high potential for all-optical magnetic recording [28].

For the application in data processing technologies discussed in the previous section, it might seem the most obvious choice to focus the investigations on the ultrafast control of magnetism on the ferromagnets, in which the spins align parallel to each other, giving rise to a magnetic moment. On the other hand, antiferromagnets, in which the spins are ordered in an antiparallel manner have for a long time been considered to be unsuitable for such purposes and were thus only considered out of academic interest [29]. Over the years, this view has changed and the antiferromagnets have gained renewed attention. For instance, the class of antiferromagnets has a much higher natural abundance than the ferromagnets while also exhibiting the spin ordering at much higher temperatures, and the absence of the net magnetization makes the devices insensitive to stray magnetic fields or external magnetic perturbations [30]. Perhaps most importantly, the spins in antiferromagnets typically precess with frequencies in the Terahertz range ($1\,\mathrm{THz} \approx 10^{12}$ Hz), as compared with the typical Gigahertz precession frequencies in the ferromagnets. Thus, to achieve the goal of ever-faster data technologies, the antiferromagnets are now considered a highly promising material of choice.

Thus far, it has been a question if all-optical recording would also be possible in antiferromagnetic systems, due to the fact that the absence of a net magnetic moment makes it challenging to control the magnetization by optical means, and has thus been under extensive investigations [31]. It was recently discovered that the antiferromagnetic order could be written and read out by the use of electric pulses through the effect of spin transfer torques,

where the spins on the electrons in spin polarized currents exert a torque on the magnetic moments. These torques alternate between the individual sublattices of the antiferromagnets, enabling the reorientation of the antiferromagnetic order [32, 33]. Although these observations seem auspicious, the switching and reading out rate is still on the order of miliseconds to seconds [34], thus lacking the ultrafast aspect of the control of magnetism.

Some of the observations in ultrafast magnetism discussed above were explained by thermal effects [24]. For example, the ultrafast heating of the sample can for example temporarily change the magnetic anisotropy of the material, thereby changing the equilibrium orientation of the magnetization [35,36]. As a result, the spins start to precess around the new equilibrium. As the sample cools down, precession continues around the initial equilibrium value [23]. Also, thermal effects were shown to be responsible for the switching dynamics in GdFeCo, as the heating of electrons can bring the system in a strongly non-equilibrium state, thereby driving the spin dynamics [27]. For prospects in ultrafast data technologies, these effects are disadvantageous, as the clock-rate of the magnetization is restricted by the cooling down rate that can be down to nanoseconds [37]. Besides, thermally driven dynamics is incoherent, and the phase of magnetization dynamics cannot be controlled through the phase of the excitation in such processes [38].

On the other hand, it was found that magnetism can also be controlled in a non-thermal manner, by direct coupling of the magnetization with the electric and/or magnetic field of light. This was demonstrated experimentally by the observation of the Inverse Faraday effect in the antiferromagnet $DyFeO_3$ [39]. In the experiment, circularly polarized light pulses were shown to be able to produce a magnetization in the direction of the wavevector of the light, where the helicity of the light determined the direction of the induced magnetization. The dependence on the incident polarization of light demonstrated the non-thermal origin of this effect. In this case, the laser pulses act as an effective magnetic field on the spins. Microscopically, this effect can be seen as impulsive stimulated Raman scattering [40, 41].

The next section will give an more extensive overview of the magneto-optical effects, that allow for both the generation of ultrafast magnetization dynamics and its detection.

1.3 Magneto-optical Effects

Magneto-optical effects encompass a broad class of effects that involve a change in the properties of light as a result from magnetic properties of a material or vice versa. The Zeeman interaction, which results in the splitting of absorption lines in magnetic materials is at the basis of these effects [42]. Similarly, materials with strong spin orbit coupling exhibit a

similar splitting of absorption lines, due to the magnetic field induced by the orbital motion of the electrons, as shown in figure 1.3.

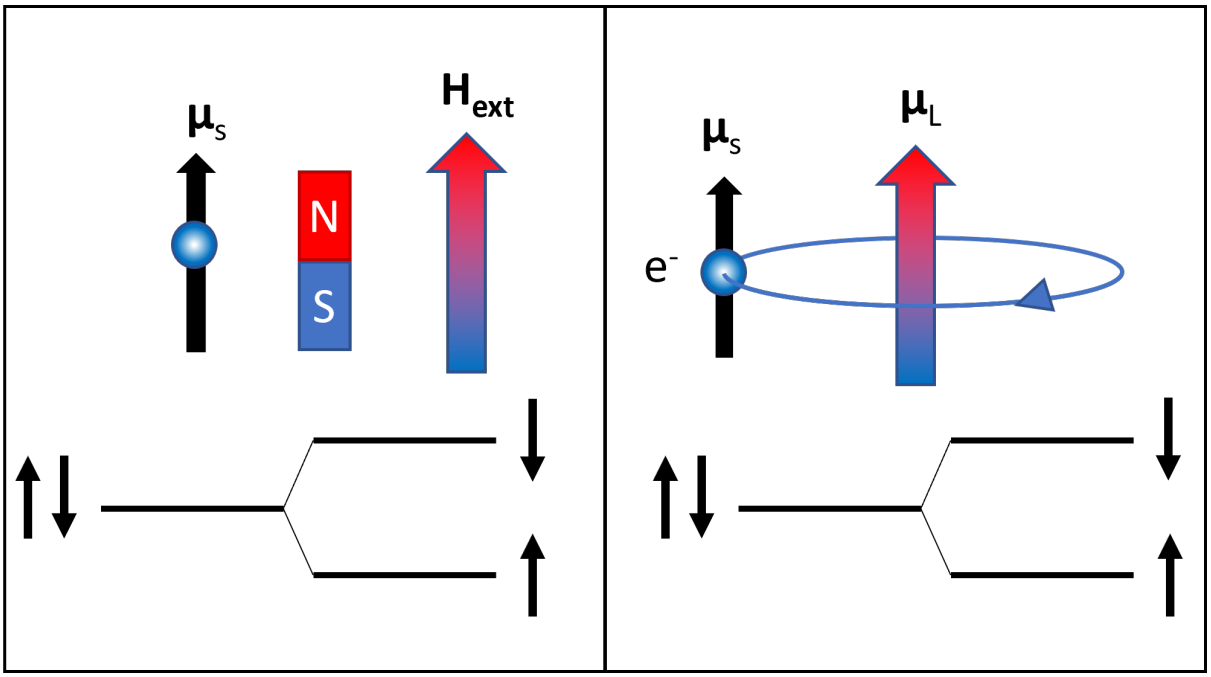

Figure 1.3: Illustration of the energy level splitting in a external magnetic field $\mathbf{H}_{\text{ext}}$ (left panel) or due to spin orbit coupling (right panel). The orbital motion of the electron charge e^- gives rise to a magnetic moment $\boldsymbol{\mu}_{\text{L}}$ that couples with the spin magnetic moment $\boldsymbol{\mu}_{\text{S}}$ resulting in the splitting of the energy levels.

These effects, combined with ultrashort light pulses provide an excellent tool to study magnetism on the ultrafast time-scale. On the other hand, as discussed in the previous section, light pulses can also be used to control the magnetic state of a material. This section will give a short summary of such magneto-optical effects.

To understand the interaction of magnetism with light, it has typically proven convenient to consider the free energy of the spin system interacting with electromagnetic fields [43]. The simplest case to consider is the light-magnet interactions in the electric dipole approximation, for which the free energy is given by

$$F = \frac{1}{2}\left(\chi_{ij}(\omega)E_i^*(\omega)E_j(\omega) + \chi_{ij}^*(\omega)E_i(\omega)E_j^*(\omega)\right) \tag{1.2}$$

The indices i, j denote the x, y, z components and summation over the repeating indices is implied. Note that in the above expression, the free energy is constructed as the product of the electric electric field E and electric polarization P, $F = -\mathbf{P}\cdot\mathbf{E}$, where $P_i = \chi_{ij}E_j$. However,

the polarization can be expanded in higher order terms (e.g. $P = \chi^{(1)}E + \chi^{(2)}E * E + ...$) [44]. Moreover, magnetic dipole and electric quadrupole contributions can be included. The form of the tensor χ_{ij} is strongly related to the symmetry of the material. Thus, material symmetries play an important role in which electro- or magneto-optical effects are observable.

In the subsections below, we will separately highlight the most relevant magneto-optical effects.

1.3.1 (Inverse) Faraday Effect

The Faraday effect was first discovered by Michael Faraday in 1845. He observed that the polarization of light was rotated in a magnetized material, and found that this rotation angle was given by

$$\theta_F = VHL \tag{1.3}$$

Here, V is the Verdet constant, H is the applied magnetic field and L is the thickness of the material.

The Faraday effect is a form of Magnetic Circular Birefringence. This means that the magnetization in the material causes right-handed and left-handed circularly polarized light to experience different refractive indices. As linearly polarized light can be decomposed in right-handed and left-handed polarizations, the polarization rotates if the circularly polarized components experience different refractive indices. Microscopically, this effect can be understood as the affected Larmor-precession eigen-frequency of the electronic orbits in the presence of magnetic fields. Through the Kramer-Kronig relation, that relates the refractive index to the absorption coefficient of a material, the split absorption line will also result in a change of the refractive index.

The Faraday effect can also be described thermodynamically in terms of the Free energy in the basis of circularly polarized light components. Note that cubic or isotropic media are required for this specific effect [45].

$$F = \chi_F H \left(E_{(+)} E^*_{(+)} - E_{(-)} E^*_{(-)} \right) \tag{1.4}$$

Here $E_{(+)}$ and $E_{(-)}$ denote right-handed and left-handed circularly polarized light respectively, and χ_F is the nonlinear susceptibility tensor responsible for the Faraday effect. As the refractive index depends on the susceptibility ($n^2 = 1 + \chi$) [46], we need to retrieve the susceptibility tensor for the right-handed and left-handed circularly polarized components. As the free energy in the electric dipole approximation is given by $F = \chi_{ij} E_i E_j$, we can see that the modulation of the susceptibility tensor can be retrieved by taking the second derivative

with respect to the electric fields of light. As a result, we find that due to the Faraday effect, the susceptibility for the left-handed and right-handed circularly polarized components of light is different by $\Delta\chi = 2\chi_F H$. Consequently, the experienced refractive index by these components is proportional to the externally applied magnetic field. This magnetic field induced birefringence gives rise to the rotation of polarization, which can be shown to be given by [42]

$$\theta_F = \frac{\omega}{2c}\Delta n L, \tag{1.5}$$

where ω and c are the frequency and speed of light respectively, Δn is the difference between the refractive indices for the left- and right handed helicity of light, which is proportional to the magnetic field or magnetization, and L is the thickness of the magneto-optical medium.

Besides the magnetization affecting the properties of light, the inverse effect is also possible. For instance, circularly polarized light pulses can induce a magnetization [39, 47]. In this case, the electric fields of light induce an effective field $\mathbf{H}_{\text{eff}} = -\frac{dF}{d\mathbf{M}}$, which results in the induced magnetization

$$\mathbf{M}(0) = \chi_F \left[\mathbf{E}(\omega) \times \mathbf{E}^*(\omega)\right]. \tag{1.6}$$

1.3.2 (Inverse) Cotton Mouton Effect

The Cotton Mouton Effect shows similarities to the Faraday effect. This effect is an example of magnetic linear birefringence, and describes the changes in the ellipticity and rotation of light polarization if the light is passing perpendicular to an applied magnetic field. This effect can typically be distinguished from the Faraday effect by the polarization dependence of the incident probe light. Whereas the Faraday rotation does not depend on the incident polarization of the light, the Cotton Mouton Effect shows a strong dependence of the obtained signals on the incident polarization plane of the probe [48]. The rotation angle of the light polarization $\Delta\phi$ after passing through a magnetized material is given by [49]

$$\Delta\phi = 2\pi\frac{L}{\lambda}\Delta n \sin(2\theta), \tag{1.7}$$

where L is the thickness of the material, λ is the probe wavelength, Δn is the magnetization-induced birefringence that is proportional to the square of the magnetization, and θ is the angle between the light polarization and the magnetization.

Similarly to the Faraday effect, we can also consider this effect in the terms of free energy. For the effect of magnetic linear birefringence, we can consider a perturbation in the per-

mittivity tensor that is quadratic in the external applied field. As a result, we can retrieve the following expression for the free energy [50, 51]:

$$F = \chi_{ijkl} E_i E_j M_k M_l. \tag{1.8}$$

Again taking the second derivative with respect to the electric fields, we obtain different permittivity for incident light pulses polarized parallel and orthogonal to the magnetization. This causes ellipticity and rotation of linearly polarized light pulses.

Moreover, similarly to the Inverse Faraday effect, we can calculate the light-induced effective field by taking the derivative to the magnetization and find that this field scales proportionally to the magnetization [51].

$$H_{\text{eff},l} = -\frac{dF}{dM_l} = -\chi_{ijkl} E_i E_j^* M_k \tag{1.9}$$

For the case of the Inverse Cotton-Mouton effect, the symmetry of the susceptibility tensor may for instance be such that only E_x and E_y components remain [40, 41]. Thus, one can see that in such a scenario, the light-induced effective field depends on the orientation of the incident pump polarization with respect to the magnetization, which results in a maximum effective field for diagonal polarization.

1.3.3 (Magneto-Optical) Kerr Effect

The Kerr effect is very similar to the Faraday effect and the Cotton Mouton effect, but the Kerr effect results in the polarization rotation of the light that is *reflected* from a magnetic material. There are many variants of the Magneto-Optical Kerr effect, depending on the direction of the incidence of the light with respect to the magnetization in the material. If the probe irradiates the sample at normal incidence, the rotation is described by the polar Kerr effect. The case when the magnetization is parallel or orthogonal to the plane of incidence of the light is described by the longitudinal and transversal Kerr Effect respectively. In Chapter 3, the Magneto-Optical Kerr Effect will be used as a tool for theoretical modeling of pump probe experiments, so a more extensive description will be given there.

1.4 Rare-earth orthoferrites

In this thesis, we will be mainly concerned with the study of anti-ferromagnetic oxides, in particular the rare-earth orthoferrites. The orthoferrites are a special case of the antiferromagnets, that were recently also suggested to be reclassified as altermagnets [5]. Their spin system

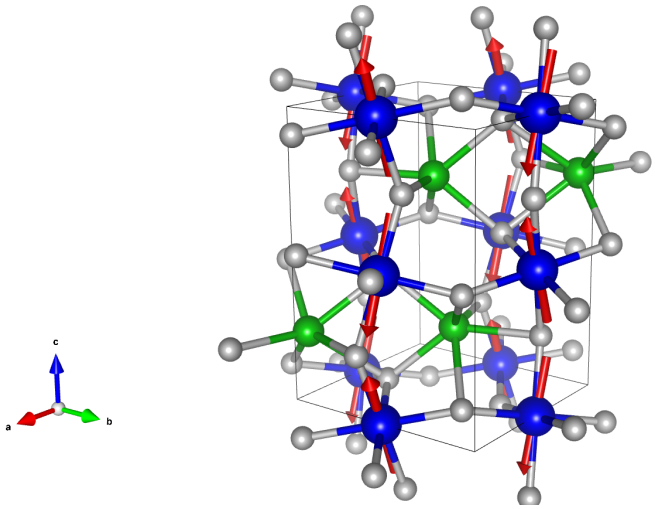

Figure 1.4: Schematic of the orthorhombic crystallographic structure of $RFeO_3$. The blue, green and grey spheres indicate the Fe, R, and O atoms respectively. The spins on the Fe ions are shown for the Γ_2 phase. Note that the spin canting is exaggerated for clarity. The crystallographic a, b, and c axis are represented with the red, green, and blue arrows respectively. Image is produced with the VESTA Software [57].

consists of four sublattices of spins. Two of these sublattices are formed by the electron spins located in the 3d-orbitals of the Fe^{3+} ions and the other two magnetic sublattices are formed by the spins of the electrons in the 4f-orbitals of the rare-earth ions. The spins on the Fe^{3+} ions are ordered antiferromagnetically below the Néel temperature, which typically occurs at high temperatures ($T_N \approx 600-750$ K) [52]. The spins in the rare-earth ions form a second sublattice, that orders only at very low temperatures, depending on the specific rare-earth ion in the orthoferrite. At the higher temperatures, the rare-earth spins are in a paramagnetic state, but they are polarized by the iron spins due to the strong coupling of the iron spins with the rare-earth spins. This interaction between the magnetic moments is responsible for the typical spin reorientation transitions (SRT) [53, 54] and affects the dynamic properties of the spins of the antiferromagnetic iron subsystem [55].

The orthoferrites are particularly interesting systems to investigate, as they exhibit a combination of the properties of antiferromagnets and ferromagnets. Due to the presence of a strong Dzyaloshinskii-Moriya interaction, the spins are not aligned in a perfectly antiparallel manner [56]. As a result of the canting of the spins, a weak ferromagnetic moment emerges. The crystallographic and magnetic structure of an example rare-earth orthoferrite ($RFeO_3$) in the magnetic Γ_2 phase is schematically illustrated in figure 1.4. For illustrative purposes, the spin canting on the iron spins is overemphasized.

To understand the magnetic properties of the orthoferrites, we also need to describe some

details on the electronic structure. In a single atom without any external interactions the electronic orbitals are energetically degenerate. However, when introducing surrounding orbitals, the electron-electron repulsion will lift this degeneracy and split the energy levels. Moreover, in the case of a Kramers rare-earth ion (an odd number of electrons) the exchange between the d-f electrons further breaks the symmetry, resulting in the splitting of Kramers doublets [58]. We will see in Chapter 6 that this electronic structure can play a significant role in the dynamics of the Fe^{3+} spins due to the interaction of these spins with the rare-earth ion spins.

Besides these interesting magnetic properties, the orthoferrites also show very useful optical properties for the experiments presented in this thesis. The orthoferrites show large Faraday rotation resulting from the strong spin-orbit interaction [39].

1.5 Magnetic interactions

This section will give an introduction to the relevant interactions in magnetic materials.

1.5.1 Exchange Interaction

The strongest and most relevant magnetic interaction is the exchange interaction, and is in the first place responsible for the existence of magnetic materials. This interaction follows directly from quantum mechanics. In particular, it is a result of the antisymmetrization of the electron wavefunction. The simplest case is to consider a two-electron system with wavefunctions that are a product of the spatial part and a spin part. Exchanging the two identical particles should result in the same wavefunction, with opposite sign. Calculating the energy of the system, one can find that there is an energy splitting for the symmetric and antisymmetric spatial parts of the wavefunction. This energy splitting is described by the exchange integral J.

The resulting exchange energy may be represented in the following form:

$$W_{\mathrm{ex}} = -\sum_{i,j} J\mathbf{S}_i \cdot \mathbf{S}_j \tag{1.10}$$

Here, i and j are indices that count over the spins. The nature of the magnetic ordering depends on the sign of the exchange interaction. For exchange integral values $J > 0$, the spins are favored to be aligned parallel to each other, thus resulting in ferromagnetic order, whereas for negative values $J < 0$ the spins align antiparallel with respect to each other, resulting in antiferromagnetic order. Antiferromagnetic order with different magnitudes of spin on the

atoms results in ferrimagnetism. Paramagnetism emerges if the exchange energy is smaller than the thermal energy, such that the spins are oriented randomly.

1.5.2 Dzyaloshinksii-Moriya Interaction

To explain the existence of weak ferromagnets, an additional interaction needs to be introduced. The interaction responsible for spin canting was first phenomenologically described by Dzyaloshinskii as a relativistic correction to the exchange interaction and Moriya later identified the microscopic mechanism in terms of spin-orbit coupling [59, 60]. The energy of this interaction is given by

$$W_{\mathrm{DMI}} = -\sum_{i,j} \mathbf{D}_{ij} \cdot \left(\mathbf{S}_i \times \mathbf{S}_j\right) \tag{1.11}$$

Thus, in combination with the exchange energy, a small canting of the spins is favored. Besides weak ferromagnetism, the DMI also gives rise to more exotic magnetic phenomena such as skyrmions, in which spins arrange themselves in vortex-like structures [61].

1.5.3 Magnetic anisotropy

In magnetic materials, the spins have energetically favorable orientations with respect to the crystallographic lattice. These preferred orientations are defined as the easy axis in the crystal structure. This effect is described by the magnetic anisotropy, and has a variety of origins that are strongly correlated with the crystallographic structure. Firstly, the shape anisotropy is a result of the dipolar interactions. Secondly the magnetocrystalline anisotropy depends on the crystallographic structure and originates from spin-orbit coupling. Moreover strain can induce a magnetoelastic anistropy, and the broken symmetry at interfaces induces a surface anisotropy [62].

The magneto crystalline anisotropy energy in an uniaxial crystal is given by [63]

$$W_{\mathrm{ani}} = K_1 \sin^2(\theta) + K_2 \sin^4(\theta) + \ldots \tag{1.12}$$

where $K_{1,2}$ are the anistropy constants, and θ is the angle of the magnetization with respect to the easy-axis.

1.5.4 Zeeman Interaction

The Zeeman Interaction is the most intuitive of the magnetic interactions. It is simply responsible for the tendency of magnetic materials to align with the external magnetic field, such as the alignment of a compass in a magnetic field. The associated energy is

$$W_{\mathrm{H}} = -\mathbf{M} \cdot \mathbf{H} \tag{1.13}$$

When a magnetic material is irradiated with light, an electromagnetic wave, we can interpret that the magnetic moment want to align with the magnetic field component of this wave. In practice however, the magnetic field of the light pulse is too small and fast to explain the amplitudes of spin precession found in experiments. It turns out that instead of the H-field, we need to consider an effective magnetic field. This field can be larger due to photo-induced changes in the magnet, which will acts as an additional torque to bring the spins out of equilibrium. For example, it has been reported that the light pulse can induce an ultrafast change in the equilibrium orientation by changing the ratio of D/J [64] or the magnetic anisotropy [35]. In this manner, the effective fields can reach up to a Tesla.

1.5.5 Dipolar Interaction

Whereas the previous interactions were quantum mechanical in origin, the magnetic dipole interaction can be understood from the classical point of view. One can view the spins as magnetic dipoles, that exert a magnetic field component on the surrounding spins. These spins will then tend to align with this external magnetic field [65]. For two spins separated at a distance $\mathbf{r}$, the dipole-dipole interaction energy is given by

$$W = -\frac{\mu_0 \gamma_1 \gamma_2 \hbar^2}{4\pi |\mathbf{r}|^3} \left[3(\mathbf{S}_1 \cdot \hat{\mathbf{r}})(\mathbf{S}_2 \cdot \hat{\mathbf{r}}) - \mathbf{S}_1 \cdot \mathbf{S}_2\right] \tag{1.14}$$

where $\gamma_{1,2}$ are the gyromagnetic ratios and $\hat{\mathbf{r}} = \mathbf{r}/|\mathbf{r}|$ is the unit vector connecting the two spins. The magnetic dipole interactions typically act over much longer ranges than the exchange interaction.

1.6 Magnetic properties of the orthoferrites

1.6.1 Static magnetic properties

To describe the spin dynamics in the orthoferrites, it is first required to investigate the static properties. Both the static and dynamic properties of any magnetic materials are determined by the interplay of many magnetic interactions. The canted antiferromagnets are most conveniently described in terms of the weak ferromagnetic moment $\mathbf{M} = \mathbf{M}_1 + \mathbf{M}_2$ and the antiferromagnetic moment $\mathbf{L} = \mathbf{M}_1 - \mathbf{M}_2$. Here $\mathbf{M}_1$ and $\mathbf{M}_2$ are the magnetizations on the different sublattices. After applying the continuous medium approximation, converting the individual spins to macroscopic magnetization vectors, the magnetic interactions are summarized by the free energy density of the spin system, which is for the case of the orthoferrite given by [66]

$$W = \frac{1}{2}JM^2 + D[M_xL_z - M_zL_x] + \frac{1}{2}(K_y - K_x)L_y^2 + \frac{1}{2}(K_z - K_x)L_z^2 + \frac{1}{4}K_4L^4 + q'(\nabla\mathbf{M})^2 + q(\nabla\mathbf{L})^2 - \mathbf{M}\cdot\mathbf{h}(t). \quad (1.15)$$

In this expression, J is the exchange constant, D is the Dzyaloshinksii-Moriya constant, $K_{x,y,z,4}$ are anisotropy constant, and q' and q are constants describing the interaction between the inhomogeneously distributed ferromagnetic and antiferromagnetic moments respectively. Considering the uniform state, the equilibrium orientation of the spins in the orthoferrites can be found by minimizing equation 1.15 with respect to the magnetic moments $\frac{\partial W}{\partial M_i} = 0$ and $\frac{\partial W}{\partial L_i} = 0$, where $i = x, y, z$.

$$\begin{aligned}
\frac{\partial W}{\partial M_x} &= JM_x + DL_z = 0,\\
\frac{\partial W}{\partial M_y} &= JM_y = 0,\\
\frac{\partial W}{\partial M_z} &= JM_z - DL_x = 0,\\
\frac{\partial W}{\partial L_x} &= -DM_z + K_4L_x^3 = 0,\\
\frac{\partial W}{\partial L_y} &= (K_y - K_x)L_y + K_4L_y^3 = 0,\\
\frac{\partial W}{\partial L_z} &= (K_z - K_x)L_z + DM_x + K_4L_z^3 = 0
\end{aligned} \quad (1.16)$$

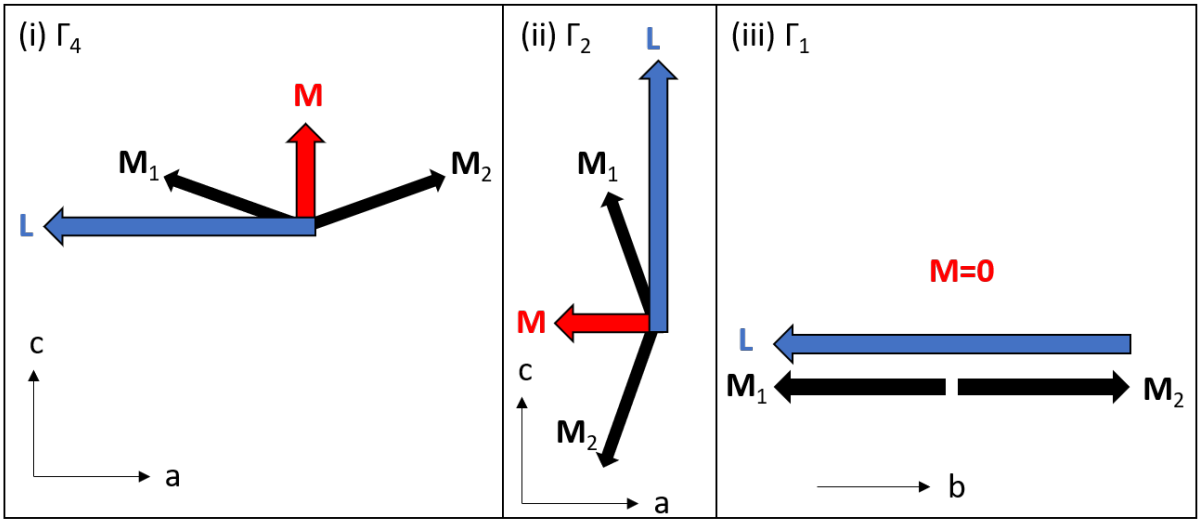

Figure 1.5: Illustration of the (i) Γ_1, (ii) Γ_2 and (iii) Γ_4 equilibrium phases in the orthoferrites. The black arrows indicate the magnetization of the two iron sublattices $\mathbf{M}_1$ and $\mathbf{M}_2$, the blue arrow denotes the antiferromagnetic vector **L** and the red arrow denotes the ferromagnetic vector **M**. The crystallographic axes are denoted by a, b and c.

This system of six equations has three distinct solutions, that correspond to the three common phases in the orthoferrites.

(i) Γ_4 phase: $L_x = L_0^{(\Gamma_{24})}$, $M_z = \frac{D}{J} L_x$

(ii) Γ_2 phase: $L_z = L_0^{(\Gamma_{24})}$, $M_x = -\frac{D}{J} L_z$

(iii) Γ_1 phase: $L_y = \sqrt{\frac{K_y - K_x}{K_4}} \equiv L_0^{(\Gamma_1)}$

The first spin configuration is the Γ_4 phase, where the weak ferromagnetic moment **M** is aligned along the crystallographic c-axis and the antiferromagnetic moment **L** is aligned along the a-axis. The second stable configuration occuring typically at lower temperatures is the Γ_2 phase, where **M** and **L** rotate 90 degrees and orient themselves along the a-axis and the c-axis respectively. The third configuration is the one that is most rarely found and is the Γ_1 phase, where the spin canting disappears and the spins align in perfectly antiparallel manner along the b-axis. These three distinct phases are schematically illustrated in figure 1.5.

1.6.2 Dynamic magnetic properties of the weak ferromagnets

Following up on the static properties of the orthoferrites, in this section, we will introduce the dynamical properties using the Landau-Lifshitz-Gilbert equations, and derive the Klein-Gordon equation for antiferromagnetic spin waves. As an example model, we will describe

the spin dynamics in the Γ_4 phase, although it should be noted that the description for the Γ_2 phase will be equivalent. The Landau-Lifshitz-Gilbert (LLG) equations have been used for many decades to describe the spin dynamics of ferromagnets [67, 68] and reads

$$\frac{d\mathbf{M}}{dt} = \gamma \mathbf{M} \times \mathbf{H}_{\text{eff}} + \alpha \mathbf{M} \times \frac{d\mathbf{M}}{dt}. \tag{1.17}$$

In equation (1.17), the effective field is determined by the derivative of the free energy of the spin system with respect to the magnetization $\mathbf{H}_{\text{eff}} = \frac{\delta W}{\delta \mathbf{M}}$. The solution to this equation has the form of a damped harmonic oscillator, that describes the precession of the magnetization value around the effective field.

In contrast to the ferromagnets, the magnetic order in antiferromagnets needs to be described by at least two sublattices, as a result from the antiparallel arrangement of the spins. As a result, we need to consider the LLG equation for both spins $\mathbf{M}_1$ and $\mathbf{M}_2$. In practice, it is more convenient to introduce two new magnetization vectors, as the difference of the two magnetizations $\mathbf{L} = \mathbf{M}_1 - \mathbf{M}_2$ and their sum $\mathbf{M} = \mathbf{M}_1 + \mathbf{M}_2$. The vector $\mathbf{L}$ is defined as the antiferromagnetic moment, and the $\mathbf{M}$ is the ferromagnetic moment.

The LLG equations for the two-sublattice antiferromagnetic system may then be written as follows [66]:

$$\begin{aligned} \frac{d\mathbf{M}}{dt} &= \gamma(\mathbf{M} \times \frac{\delta W}{\delta \mathbf{M}}) + \gamma(\mathbf{L} \times \frac{\delta W}{\delta \mathbf{L}}), \\ \frac{d\mathbf{L}}{dt} &= \gamma(\mathbf{M} \times \frac{\delta W}{\delta \mathbf{L}}) + \gamma(\mathbf{L} \times \frac{\delta W}{\delta \mathbf{M}}). \end{aligned} \tag{1.18}$$

Note that for simplicity, we have neglected the damping here, but as it is known that the solutions to the equations are harmonic oscillators, the damping can be reintroduced in the final stage of the calculation. The free energy is a function of both $\mathbf{M}$, $\mathbf{L}$ and their derivatives $\nabla\mathbf{M}$ and $\nabla\mathbf{L}$, such that the following definition of the functional derivatives are employed:

$$\frac{\delta W}{\delta \mathbf{M}} = \frac{\partial W}{\partial \mathbf{M}} - \nabla \frac{\partial W}{\partial \nabla \mathbf{M}} = \frac{\partial W}{\partial \mathbf{M}} - \sum_{p=1}^{3} \frac{\partial}{\partial x_p} \frac{\partial W}{\partial (\frac{\partial \mathbf{M}}{\partial x_p})}. \tag{1.19}$$

We can write the coupled equations of motion for each of the magnetization components in equation (1.18), using the expressions for the effective fields as given by equation 1.15 and (1.19).

$$
\begin{aligned}
&\frac{1}{\gamma}\frac{dM_x}{dt} = D(M_xL_y - L_xM_y) + L_yL_z[(K_z - K_y) + K_4(L_z^2 - L_y^2)] \\
&+ q'(M_z\nabla^2 M_y - M_y\nabla^2 M_z) + q(L_z\nabla^2 L_y - L_y\nabla^2 L_z) + M_y h_z(t) - M_z h_y(t), \\
&\frac{1}{\gamma}\frac{dM_y}{dt} = -L_xL_z[(K_z - K_x) + K_4(L_z^2 - L_x^2)] \\
&+ q'(M_x\nabla^2 M_z - M_z\nabla^2 M_x) + q(L_x\nabla^2 L_z - L_z\nabla^2 L_x) + M_z h_x(t) - M_x h_z(t), \\
&\frac{1}{\gamma}\frac{dM_z}{dt} = D(L_yM_z - M_yL_z) + L_xL_y[(K_y - K_x) + K_4(L_y^2 - L_x^2)] \\
&+ q'(M_y\nabla^2 M_x - M_x\nabla^2 M_y) + q(L_y\nabla^2 L_x - L_x\nabla^2 L_y) + M_x h_y(t) - M_y h_x(t), \\
&\frac{1}{\gamma}\frac{dL_x}{dt} = J(L_yM_z - L_zM_y) + D(M_xM_y - L_xL_y) + M_yL_z[(K_z - K_x) + K_4L_z^2] \\
&- M_zL_y[(K_y - K_x) - K_4L_y^2] + q'(L_z\nabla^2 M_y - L_y\nabla^2 M_z) \\
&+ q(M_z\nabla^2 L_y - M_y\nabla^2 L_z) + L_y h_z(t) - L_z h_y(t), \\
&\frac{1}{\gamma}\frac{dL_y}{dt} = J(L_zM_x - L_xM_z) + D(L_x^2 + L_z^2 - M_z^2 - M_x^2) - L_zM_x((K_z - K_x) \\
&- K_4L_z^2) + K_4M_zL_x^3 + q'(L_x\nabla^2 M_z - L_z\nabla^2 M_x) + q(M_x\nabla^2 L_z - M_z\nabla^2 L_x) \\
&+ L_z h_x(t) - L_x h_z(t), \\
&\frac{1}{\gamma}\frac{dL_z}{dt} = J(L_xM_y - L_yM_x) + D(M_yM_z - L_yL_z) + M_xL_y[(K_y - K_x) + K_4L_y^2] \\
&- K_4M_yL_x^3 + q'(L_y\nabla^2 M_x - L_x\nabla^2 M_y) + q(M_y\nabla^2 L_x - M_x\nabla^2 L_y) \\
&+ L_x h_y(t) - L_y h_x(t).
\end{aligned}
\tag{1.20}
$$

In principle, these equations are strongly nonlinear but in practice the spin deflections in antiferromagnets are often restricted to a few degrees [69, 70], such that we can apply the linearization procedure. We can denote the spin deflections induced by the effective field as the sum of the static magnetization and the field induced dynamic magnetization $\mathbf{M}(t) = \mathbf{M}_0 + \mathbf{m}(t)$ and $\mathbf{L}(t) = \mathbf{L}_0 + \mathbf{l}(t)$, where $\mathbf{m}(t) << \mathbf{M}_0$ and $\mathbf{l}(t) << \mathbf{L}_0$. Moreover, we can restrict our description to the spin system in one of the aforementioned phases. We choose to focus on the spin system in the Γ_4 phase, as the spin system in the previously performed experiment was in the Γ_4 phase. Note that from the symmetry of the Γ_2 phase and the Γ_4 phase (the magnetizations rotate by 90 degrees in the xz-plane), the equivalent set of equations will hold in the Γ_2 phase.

We can assume that the constants $J << D << K << q^{(\prime)}$ and in the Γ_4 phase, $M_z = M_0$ and $L_x = L_0$. Applying the linearization procudure, the set of six coupled equations (1.20)

simplifies to two sets of three coupled equations:

$$\begin{aligned}
\frac{1}{\gamma}\frac{dm_x(t)}{dt} &= L_0 D[\frac{q'}{J}\nabla^2 - 1]m_y(t) - \frac{D}{J}L_0 h_y(t),\\
\frac{1}{\gamma}\frac{dm_y(t)}{dt} &= -L_0[(K_z - K_x) + q\nabla^2]l_z(t) - q'L_0\frac{D}{J}\nabla^2 m_x(t) + \frac{D}{J}L_0 h_x(t),\\
\frac{1}{\gamma}\frac{dl_z(t)}{dt} &= L_0[\frac{D^2}{J} + J - q'\nabla^2]m_y(t) + L_0 h_y(t),
\end{aligned} \tag{1.21}$$

and

$$\begin{aligned}
\frac{1}{\gamma}\frac{dl_x(t)}{dt} &= L_0\frac{D}{J}(q\nabla^2 - (K_y - K_x))l_y(t),\\
\frac{1}{\gamma}\frac{dl_y(t)}{dt} &= -L_0(J - q'\nabla^2)m_z(t) + L_0 D(2 - \frac{q}{J}\nabla^2)l_x(t) - L_0 h_z(t),\\
\frac{1}{\gamma}\frac{dm_z(t)}{dt} &= L_0[(K_y - K_x) + \frac{D^2}{J} - q\nabla^2]l_y(t).
\end{aligned} \tag{1.22}$$

Introducing the parameters in equation (1.23),

$$\begin{aligned}
\omega_A^{(\mathrm{qFM})} &= \gamma L_0(K_z - K_x),\\
\omega_A^{(\mathrm{qAFM})} &= \gamma L_0(K_y - K_x),\\
\omega_E &= \gamma L_0 J,\\
\omega_{h_y} &= \gamma h_y(t),\\
\omega_{\dot{h}_z} &= \gamma\frac{\partial h_z(t)}{\partial t},\\
v_{\mathrm{qFM}}^2 &= \gamma^2 L_0^2 q' J,\\
v_{\mathrm{qAFM}}^2 &= \gamma^2 L_0^2 q J,\\
\omega_0^{(\mathrm{qFM})} &= \sqrt{\omega_E \omega_A^{(\mathrm{qFM})}},\\
\omega_0^{(\mathrm{qAFM})} &= \sqrt{\omega_E \omega_A^{(\mathrm{qAFM})}}.
\end{aligned} \tag{1.23}$$

we can combine the equations (1.21) and (1.22) and reintroduce the damping parameter to obtain the two equations (1.24) for harmonic oscillators for the dynamic m_y and l_y components

$$\begin{aligned}\frac{\partial^2 m_y(t)}{\partial t^2} + (\omega_0^2 - v_{\mathrm{qFM}}^2 \nabla^2) m_y(t) + 2\alpha \frac{\partial m_y(t)}{\partial t} &= L_0 \omega_h h_y(t), \\ \frac{\partial^2 l_y(t)}{\partial t^2} + (\omega_0^2 - v_{\mathrm{qAFM}}^2 \nabla^2) l_y(t) + 2\alpha \frac{\partial l_y(t)}{\partial t} &= -L_0 \omega_h \dot{h}_z(t).\end{aligned} \tag{1.24}$$

Here, v_{qAFM} and v_{qFM} represents the maximum propagation velocity of the spin waves. These equations have the form of the wave equation, which is commonly referred to as the Klein-Gordon equation. Thus we see that the two-sublattice magnetic dynamics will be defined by two orthogonal (and therefore non-interacting) modes [71] oscillating with distinct frequencies $\omega_0 = \sqrt{\omega_E \omega_A}$, as the anisotropy constants differ for the the modes. These two modes are referred to as the quasi-ferromagnetic (q-FM) and the quasi-antiferromagnetic (q-AFM) modes. Note that as the anisotropy is typically strongly dependent on temperature [72, 73], the resonance frequency will also depend on the temperature.

1.7 Magnonics

The antiferromagnetic resonance precession can in principle be viewed as spin waves, in the time domain. The quanta of spin waves are referred to as magnons and the field that studies the propagation of such waves is referred to as magnonics. In the case of a strongly uniform excitation, all of the spins will precess with the same phase, but if spins are inhomongeneously excited, the spin waves in the spatial domain can also emerge. These spin waves are defined as the $k = 0$ and $k \neq 0$ magnons. The comparison of such magnons is illustrated in figure 1.6.

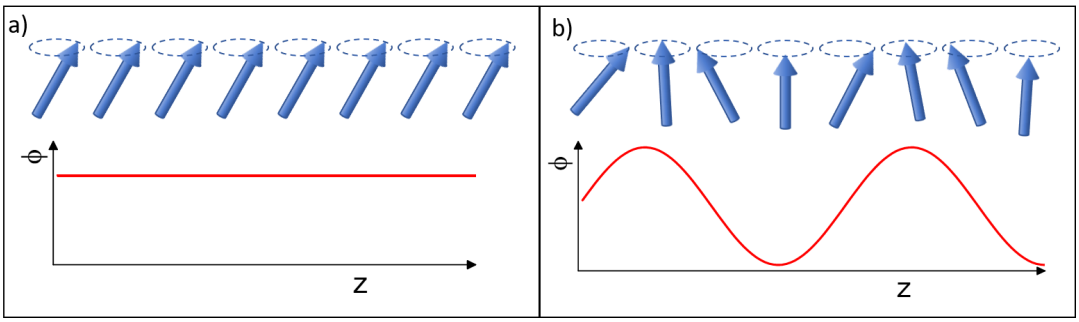

Figure 1.6: Illustration of the difference between the ferromagnetic a) k=0 magnon and b) k≠0 magnon. As the spins precess in phase for the k=0 magnon, the spatial profile of spin deflections is uniform, whereas a spatial wave is formed for the case of the $k \neq 0$ magnon.

Such waves were already predicted in 1930 by Bloch [74]. The precessional frequencies and wavenumbers of the spin waves are related through the dispersion relation. This dispersion

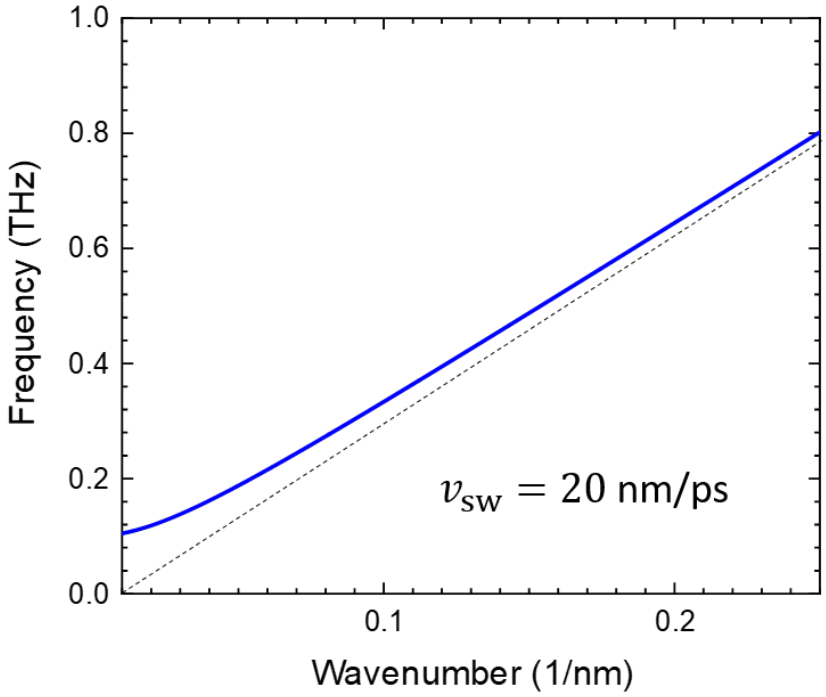

Figure 1.7: Plot of the dispersion relation for magnons in the orthoferrites. The dashed line represents the magnon velocity limit, which is typically around 20 nm/ps in the orthoferrites.

relation is significantly different for ferromagnets and antiferromagnets. As mentioned in section 1.2, the typical precessional frequencies are in the GHz range and the dispersion relation is parabolic and dependent on the bias field [75]. In contrast, in the orthoferrites the frequencies the antiferromagnetic resonance are in the THz range. As will be shown in Chapter 3, the dispersion relation in the orthoferrites is quasi-linear and given by

$$\omega^2 = \omega_0^2 + v_{sw}^2 k^2 + 2i\alpha\omega, \tag{1.25}$$

with ω_0 the frequency of the $k = 0$ mode, v_{sw} the velocity limit of the spin wave, k the wavenumber, and α a term accounting for the damping of the spin precession. Note that the dispersion relation may differ for the q-FM and q-AFM mode. This dispersion relation is plotted in figure 1.7.

These propagating spin waves have attracted high interest for their potential to store and transport information [76–79] and for wave-based computing [80].

Due to the high magnetic moment in ferromagnets, they have been the obvious system for the study of magnons, and a lot of progress in the field of magnonics has been made [79]. For instance, the spin waves have been optically excited in a localized region by focusing a laser pulse [81–83] and magneto-optically probed by tightly focused probe pulses while scanning

over the surface. Alternatively, techniques have been developed to perform (ultrafast) imaging of the spin waves [84–86].

It was realized that the wave-like character of magnons could be exploited to manipulate and steer the spin waves by variation of the magnetic landscape, acting as a sort of varying refractive index for magnons [87], analogous to the control of light. This field in magnonics research is defined as graded-index magnonics. Examples of achievements in graded-index magnonics include the experimental realization of magnonic lenses for the focusing of spin waves [88]. Confinement [89] and steering [90] of the spin waves has also proven possible. Moreover, there have been attempts on the demonstration of magnon-based logic operations. [83, 91]

Despite the rapid progress in the field, one of the challenges that magnonics has been facing, is the miniaturization of such spin waves. In the typical ferromagnets, the spin waves are dominated by the long range magneto-static dipole interactions , which restricts the wavelength of such spin waves to the μm-scale or larger. To make the spin waves suitable for implementation in future computing devices, downscaling the wavelengths to the nm-scale is a prerequisite. Although such short wavelength magnons have been demonstrated as standing waves in thin films [92, 93], such magnons lack the desired propagation.

The alternative is to generate magnons in the antiferromagnets, in which the spin waves are exchange-dominated. The additional advantage here is that the spin wave velocities are much higher than in the ferromagnets [94,95]. Exciting magnons in such systems has however proven difficult, due to the lack of net magnetic moments. Besides, the nanoscale spin waves require a strongly localized excitation spot. The conventional technique of focusing the laser tightly, does not work as the light typically cannot be focused more tightly than tens of μm, due to the diffraction limit. As a consequence, it was only possible to excite the k=0 uniform precession magnon modes. Possible solutions involve the coupling of the magnons to terahertz frequency pulses of light. These hybrid modes are referred to as magnon-polaritons, and enable the transport of the magnon at high speeds of around 1 % of the speed of light in the medium [96–98], but comes at the cost of the increased magnon wavelength on the scale of about 10 μm. Consequently, the realization of spin wave transport was restricted to diffusive propagation of incoherent magnons [99–101] and evanescent modes [102].

Only recently, a way was discovered to achieve coherent spin wave transport in antiferromagnets [70]. This will be highlighted further in Chapter 3.

Although the physics in magnonics is strongly nonlinear, nonlinear effects in antiferromagnetic magnons remain unexplored. For instance, it is highly desirable to be able to amplify (or suppress) magnons through nonlinear interactions for the use in magnon logic

gates, as the spin waves strongly attenuate during their propagation [79]. Such nonlinearities will be investigated in Chapter 5.

1.8 Terahertz spectroscopy

As we have seen above, the spin wave resonances in antiferromagnets are in the THz range. Therefore, it would make sense to use THz light pulses, such that the magnetic field of the light can couple directly and resonantly to the spins by exerting a Zeeman torque [103, 104].

The THz range photon energies are not only in resonance with the magnons, but also for instance with molecular rotations and with phonons, which are vibrations in the crystallographic lattice structure [105]. As phonons and magnetism are closely coupled, the use of resonant pumping of phonons has also been shown to provide an efficient pathway to manipulate magnetism [106, 107]. For instance, it was recently demonstrated that the ferromagnetism can be induced at temperatures above the Curie temperature through optical manipulation of the crystal lattice [108], and switching of the magnetization through resonant phononic excitations by infrared light pulses has been reported [109].

However, the challenge with the use of THz pulses was the lack of powerful THz sources, resulting in the so called THz gap as the frequencies are too high for conventional electronics, but too low for conventional optics [110]. Such pulses can nowadays be generated using Free Electron Lasers in large scale facilities [111], but are therefore very costly with limited availability.

Developments in the field of nonlinear optics [112] has provided a pathway for generating table-top THz sources. By converting laser light by optical rectification, intense THz sources have become available. The details on the nonlinear optical techniques to generate such intense pulses will be described more extensively in Chapter 2.

This has resulted in a wide variety of spectroscopic techniques involving TeraHertz radiation. The main technique involving THz light used in this thesis is the intense THz-pump - optical probe spectroscopy [113].

On the other hand, THz pulses may also be used as a probe for THz frequency dynamics in THz Time Domain Spectroscopy technique. [114] As it is possible to track the temporal profile of the THz pulse using methods as Electro-Optic Sampling (see Chapter 2 for a description), studying the THz profiles after emission from or transmission through a sample provides direct information on the spin dynamics. THz light can also be emitted from magnetic materials as magnetic dipole radiation. This technique is defined as THz emission spectroscopy [64, 115, 116]. Alternatively, broadband THz pulses can be used as a probe and

changes in the THz pulse can be detected, for instance as a result of changes induced by an optical pump [117].

1.9 Outline of this Thesis

The contents of this thesis are distributed as follows: In Chapter 1, we have already illustrated some background to the field of antiferromagnetic magnonics. In Chapter 2, we will introduce the experimental tools, where a more detailed description of the used experimental techniques is given. This Chapter will also guide through the design process of the newly built intense THz generation setup. In Chapter 3, we will describe the generation of coherent propagating magnons, from a theoretical point of view by exploiting the band gap excitation to achieve strong localization of the excitation. Then, in Chapter 4, we performed the experiment based on the theory in Chapter 3, and basic experimental results on the generation and detection of the propagating coherent magnons in $HoFeO_3$ will be given. Chapter 5 will build further upon this experiment, and we will introduce a second pump pulse to search for nonlinear effects in the propagation of magnons. In particular, we will highlight the possibility to convert the $k = 0$ magnon mode to the $k \neq 0$ magnon mode. The intense THz pump - optical probe setup will be employed in Chapter 6, where we will search for high-amplitude spin dynamics in $ErFeO_3$. In Chapter 7, we will draw conclusions and provide an outlook. This will be accompanied by some preliminary results demonstrating that the intense THz pump can also be used to study other systems than iron oxides. More specifically, we will show the THz-induced ultrafast dynamics in the metallic Iron-Rhodium (FeRh).

Chapter 2

Experimental methods

In this chapter, we will provide an introduction to the experimental techniques used for the experiments in the remainder of this thesis. The first part of this chapter will describe the basics of pump-probe spectroscopy, and give details of the setup for the experiment on the generation and detection of THz spin waves in antiferromagnets (Chapter 4). Also, a more advanced setup to investigate nonlinear characteristics of the spin waves by exciting the dynamics with two time delayed pump pulses will be shortly introduced. A more thorough description of this experiment will be given in Chapter 5. In the second part of this chapter, another experimental method for efficient, resonant excitation of the antiferromagnetic spin precession by broadband THz pulses will be discussed (Chapter 6).

2.1 Pump probe spectroscopy

Using ultrafast lasers with sub-picosecond pulse durations allows for the study of a multitude of phenomena at picosecond time scales. Pump-probe spectroscopy is a commonly used technique to study ultrafast dynamics in the time domain. The principle of this spectroscopic technique is as follows: A light pulse from a pulsed laser is split into two beams of photons, for example by the use of a beam-splitter. Typically, one of these portions will have much higher power than the other portion. This high power part acts as the pump pulse, and will launch the dynamics of the sample, for example by inducing spin precession. The second portion of the light pulse is typically strongly attenuated, such that the pulse intensity is much weaker than the pump pulse. This pulse will act as a probe and can measure the state of the sample, for instance through magneto-optical effects. By sending the pulse through a delay line, the time delay $\Delta t = 2\Delta x/c$, with Δx the change in position of the delay line and c the speed of light, can be controlled with sub-picosecond resolution. This allows one to

track the photo-induced ultrafast dynamics. The concept of pump-probe spectroscopy is summarized in figure 2.1.

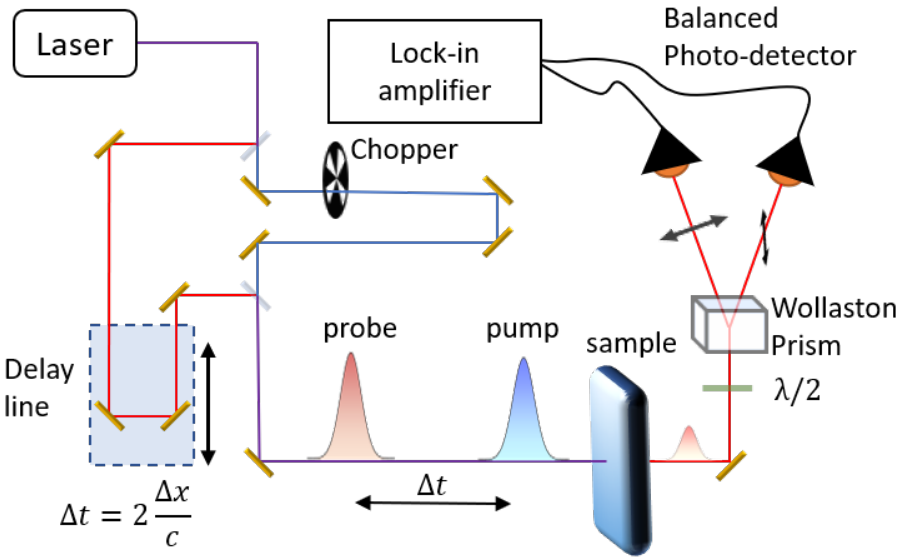

Figure 2.1: Schematic of the pump probe experiment. The concept of the experiment is discussed in the main text.

Note that with a small modification in the setup, it is possible to introduce a second pump, which may for example be used to investigate nonlinear physical phenomena.

In our pump probe experiment, we are most often focused on measuring the Faraday or Kerr effect, thus the polarization rotation of the probe pulse. This pump-induced rotation is measured with a set of balanced photo-detectors and a Wollaston Prism. When the probe pulse passes through the Wollaston prism, the probe pulse is split into two orthogonally polarized beams that propagate with an angle with respect to each other. These separated beams are sent to a pair of photodetectors that measure the intensity of the probe pulse. The photodetectors are balanced in the absence of the pump pulse using a $\lambda/2$ plate to achieve the highest sensitivity to the pump-induced changes (this balanced condition would correspond to diagonal polarization, i.e. equal contributions of horizontal and vertically polarized components). Thus, the polarization rotation will result in a changing intensity on both photo-detectors, and the difference between the signals on these detectors provide a direct measure for the rotation.

We extract only the pump induced signals on the photodetectors with a lock-in amplifier. The next section provides a description of the working principles of the lock-in detection technique.

Lock-in detection technique

The photo-induced magneto-optical signals in pump probe experiments are typically very small, and direct measurement would thus suffer from a poor signal to noise ratio. Moreover, it is important to distinguish the signals that are pump-induced from the static signals. The lock-in technique provides a solution to these two challenges, and thus the signals from the photodetectors are analyzed with a lock-in amplifier. The lock-in amplifier requires modulated input signals with a certain frequency, and filters out all signal and noise occuring at any other frequency. This fact can be exploited to distinguish the pump induced signals from the static signals. To this end, an optical chopper is placed in the path of the pump pulse. This chopper rotates at a frequency of $f_{\text{pump}} = \frac{f_{\text{probe}}}{2} = 500\,\text{Hz}$, such that every other pump pulse is blocked or transmitted. The lock-in amplifier takes this frequency as a reference, and mixes it with the input signal [118]. Assuming the signal is periodic with frequency ω_{in}, and the reference signal is periodic with frequency ω_{ref}, we can write the output signal after mixing in the amplifier as

$$V_{\text{out}} = V_{\text{in}} V_{\text{ref}} \sin(\omega_{\text{in}} t + \phi_{\text{in}}) \times \sin(\omega_{\text{ref}} t + \phi_{\text{ref}}) \tag{2.1}$$

Using trigonometric identities, we can rewrite this product as

$$V_{\text{out}} = \frac{V_{\text{in}} V_{\text{ref}}}{2} \left(\cos([\omega_{\text{in}} - \omega_{\text{ref}}]\, t + \phi_{\text{in}} - \phi_{\text{ref}}) - \cos([\omega_{\text{in}} + \omega_{\text{ref}}]\, t + \phi_{\text{in}} + \phi_{\text{ref}})\right) \tag{2.2}$$

When this signal is passed through a lowpass filter, the second term, which oscillates at high frequency is filtered out. Then, the acquired signals are integrated over time, for the duration of the lock-in time constant.

Due to the orthogonality of the sinusoidal functions, the only components that will remain in the output of the lock-in amplifier will be the signals that oscillate at the same frequency as the reference. Thus, the lock-in amplifier acts as a filter to remove all signals and noise occuring at any other frequencies.

The resulting output will be

$$V_{\text{out}} = \frac{V_{\text{in}} V_{\text{ref}}}{2} \cos(\phi_{\text{in}} - \phi_{\text{ref}}) \tag{2.3}$$

This part of the signal is referred to as the real part of the signal. Similarly, by multiplying the input signal in with the reference that is phase-shifted 90°, the imaginary part is obtained (in equation (2.3), the cosine will be replaced by the sine).

Thus, the lock-in detection is phase sensitive. To obtain the maximum signal amplitude, the phase shift between the reference and the input signal must be chosen appropriately.

Alternatively, the magnitude can be calculated from the real and imaginary part, to remove the phase sensitivity.

To summarize this section, we have seen that the lock-in amplifier can be used to sensitively detect small signals by filtering out all noise and other frequency signals. This principle is very important in pump-probe spectroscopy, as it allows us to be sensitive solely to the pump-induced signals. Although the lock-in amplifier is commonly used in pump-probe spectroscopy, it is important to highlight the operational principle for the understanding of some of the results in this thesis. In particular, in Chapter 5 we will extend the pump-probe scheme by introducing a second pump pulse to search for nonlinear effects. In this scenario, it is important to understand that we are only sensitive to the photo-induced changes to the pumps that are chopped by the chopper. For instance, it is possible to pass both pump pulses through the chopper, in which case we should see the summation of the linear signals, and the nonlinear signal. If we position the optical chopper such that only one of the pump pulses passes through however, we will only be sensitive to the linear signals of the pump, and the nonlinear effect that the pump that is not chopped has on the pump that is chopped. The linear signals of the pump that is not chopped will not be visible in such an experimental configuration.

2.2 THz generation

Besides using the direct output of the laser system as both the pump and probe, it is also possible to convert the laser pulse to different wavelengths through nonlinear optical processes. In this section, we will describe how 800 nm light can be converted to intense THz pulses.

2.2.1 Theory of optical rectification

This section gives an introduction to the nonlinear process of optical rectification, where difference frequency generation occurs within the electric field of a laser pulse. For such processes, high input powers are required.

For very high electric fields, the material response is not linear anymore, but can be Taylor expanded into the following expression:

$$P_i = \chi^{(1)}_{ij} E_j + \chi^{(2)}_{ijk} E_j E_k + ... \tag{2.4}$$

where summation over repeating indices is implied. In this equation the indices represent the x,y or z components of the polarization P and the electric field E. The linear susceptibility of

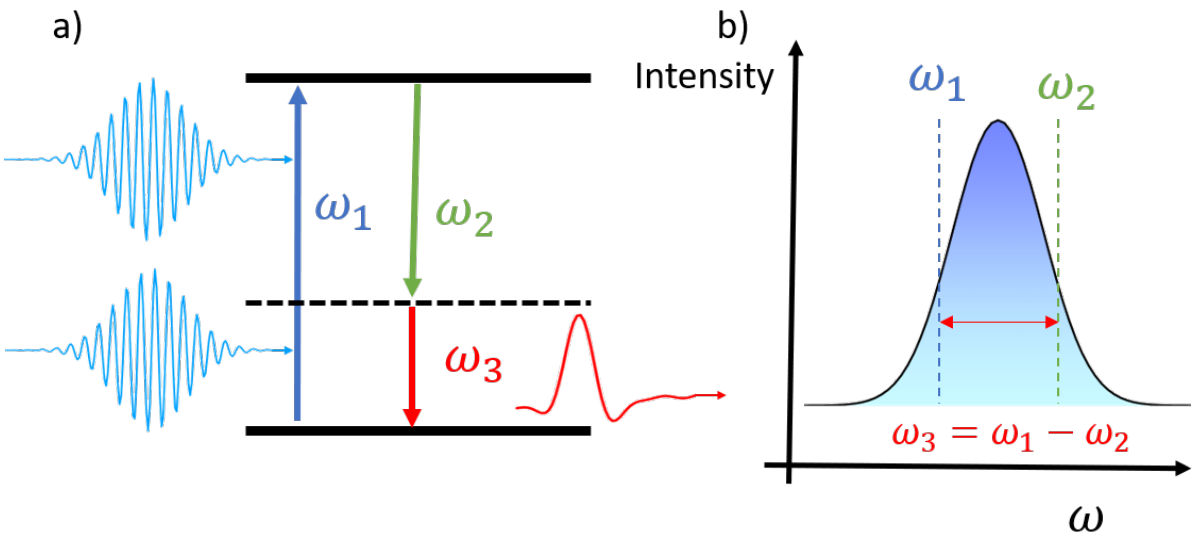

Figure 2.2: a) Schematic of the process of OR. Two identical ultrashort pulses are absorbed and as a result a broadband THz pulse is emitted. b) Representation of the OR process in the spectral domain. This process occurs for all components ω_1 and ω_2 in the pulse, resulting in a broadband THz pulse.

the material is given by $\chi^{(1)}_{ij}$, and $\chi^{(2)}_{ijk}$ is the nonlinear susceptibility. The nonlinear susceptibility gives rise to various nonlinear optical phenomena, such as Second Harmonic Generation (SHG), Sum Frequency Generation (SFG), Difference Frequency Generation (DFG) and Optical Rectification (OR). In SHG, two photons of the same energy are converted to a single photon with double the energy. In SFG, mixing of two light sources with different photon energies result in a photon energy that is the sum of the two energies, whereas in DFG the resulting energy is the difference between the two photon energies.

OR is somewhat comparable to the process of DFG. However, in OR, the resulting photon energy is the difference between energy components within the same broadband pulse [119]. This is illustrated in figure 2.2. This self-interaction of the broadband light pulses typically yields difference frequencies that are in the THz range.

2.2.2 Phase matching

In nonlinear optics, the phase matching condition is essential for efficient conversion processes of light. Due to the dispersion of light in the medium, the input photons and the converted photons typically travel with different velocities through the material, resulting in a relative phase shift. This phase mismatch causes the generated THz waves to interfere with each other destructively, thereby reducing the generation efficiency. The phase matching condition can be written as [120]

$$\Delta\mathbf{k} = \mathbf{k}_1 - \mathbf{k}_2 - \mathbf{k}_3 = 0. \tag{2.5}$$

Here $\mathbf{k}_1$ and $\mathbf{k}_2$ represent the wave vectors of the incoming pump photons at frequencies ω_1 and ω_2, and $\mathbf{k}_3$ is the wave vector of the generated THz photon at frequency ω_3 (see figure 2.2). Whether these conditions are satisfied depends largely on the nonlinear optical crystal of choice and the wavelength. If the phase matching conditions are not satisfied, various techniques are available to achieve phase matching. For instance, the birefringence of the crystal can be exploited to select an appropriate angle of incidence, such that the refractive indices of the input and generated rays [121]. Alternatively, the nonlinearity can be periodically poled after the walk-off length during which the generated light goes out of phase with the input [122]. This technique is suitable for the generation of narrow-band THz pules [123]. In this thesis, the tilted pulse front phase matching technique will be used for efficient THz generation. More details on this technique will be given in the following section containing the description of the experimental setup.

2.3 Experimental Setup

In this section, an overview of the experimental setup is given. The following sections will provide a stepwise guide through the relevant components of the setup. The global schematic of the intense THz pump - optical probe setup is shown in figure 2.3.

2.3.1 Laser system

For the generation of intense THz pulses, we require the use of a laser that can achieve high pump pulse energies. We use a Ti:Sapphire laser system with an OPA, providing laser pulses with a duration of about 40 fs and a repetition rate of 1 kHz. The laser system can provide laser pulses with an energy up to 7 mJ at the center wavelength of 800 nm. We note that the optimal duration of the laser pulses is approximately 300 fs, for which the THz generation efficiency can reach up to 5%. For our laser system, the expected efficiency is $\approx 1\%$ [124]. On the other hand, as can be seen in the description on OR, the pulse width determines the spectral width. The short duration pulses will be broadband in the frequency domain, and thus allow for the generation of a broader band of THz radiation.

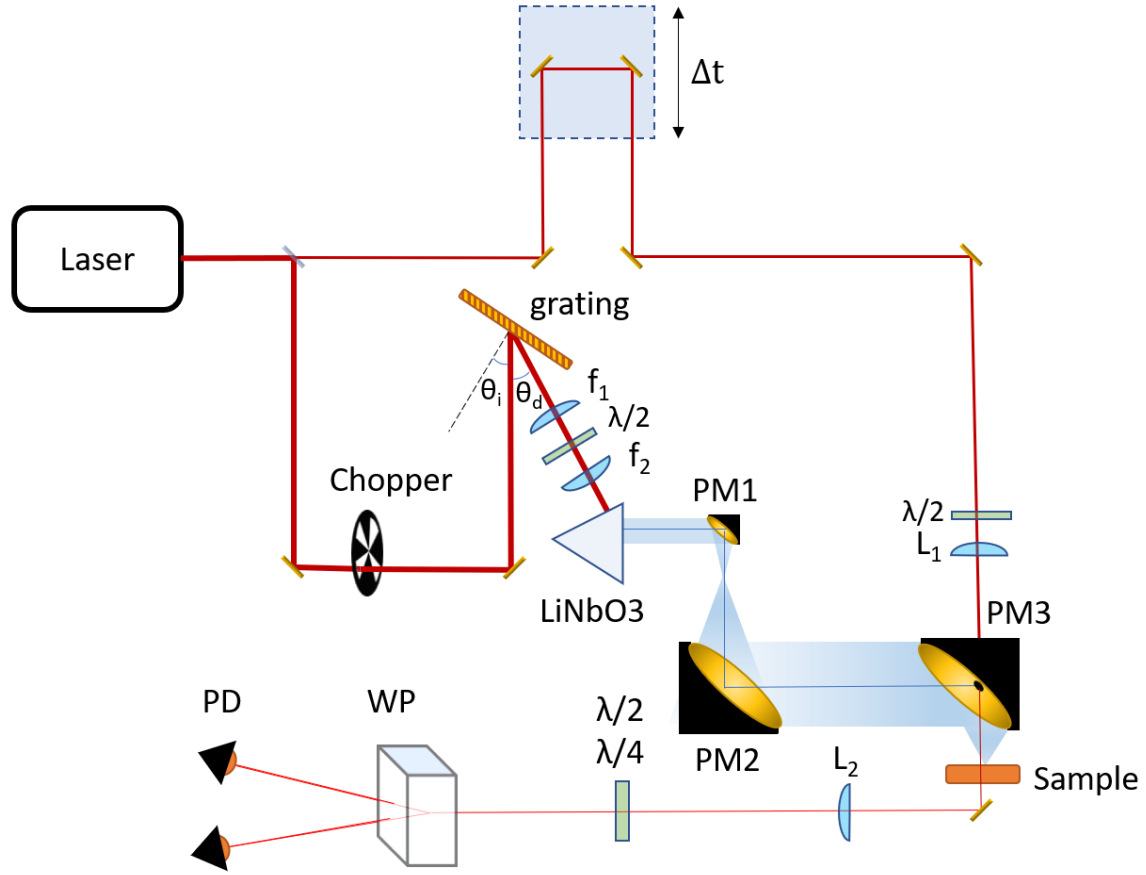

Figure 2.3: Schematic Illustration of the intense THz pump setup. The laser output is split in the pump and probe. The pump is converted to THz radiation with OR in the $LiNbO_3$ prism. More specifics on the involved optics will be discussed in the main text. Cylindrical lenses are denoted by f, and spherical lenses are denoted by L. PM indicate the parabolic mirrors. The angle of incidence on the grating and the diffracted angle are indicated by θ_i and θ_d respectively. The half wave plates are indicated by $\lambda/2$ and the quarter wave plates by $\lambda/4$. WP is the Wollaston prism, and PD represents the photodetectors.

2.3.2 Tilted Pulse Front THz generation

One of the most efficient nonlinear optical materials available is $LiNbO_3$, due to its large nonlinear optical coefficient [125]. However, one of the major difficulties using OR for THz generation in $LiNbO_3$, is the large difference in the refractive index for the near-IR pump and the THz. For the 800 nm near-IR pump pulse, the refractive index is about 2.2 [126], whereas the refractive index for the THz is about 5 [127]. As a result, the pump pulse and the THz pulse propagate with drastically different velocities through the medium, which causes a large phase mismatch.

Recently, a technique for highly efficient THz generation has been developed, namely THz generation using a tilted pulse front. As illustrated in figure 2.4, the phase matching condition is satisfied by introducing a tilting angle of the pulse front. To match the projection of the group velocity of the pump pulse with the velocity of the generated THz, the following tilt angle of the pulse front is required [128]:

$$n_{\mathrm{p}}^{\mathrm{gr}} = \cos(\gamma)\, n_{\mathrm{THz}}^{\mathrm{ph}}. \tag{2.6}$$

Here $n_{\mathrm{p}}^{\mathrm{gr}}$ is the refractive index for the group velocity of the pump pulse and $n_{\mathrm{THz}}^{\mathrm{ph}}$ is the refractive index for the velocity of the generated THz pulse and γ is the tilting angle of the pulse front, as illustrated in figure 2.4.

Using the aforementioned refractive indices for the $LiNbO_3$ crystal, we find that the optimal tilt angle is about 64°.

In our experimental setup, we use a $LiNbO_3$ crystal, which is cut at an angle of 62°. The dimensions of the input faces are 10 mm × 10 mm. The $LiNbO_3$ prism is doped with MgO to increase the damage threshold. We create the tilted pulse front by using a diffraction grating, and two cylindrical lenses to produce the image of the diffraction grating on the $LiNbO_3$ crystal. A theoretical study has been performed by Tokodi et al. [129] to optimize the parameters of the tilted pulse front THz generation setup containing a two-lens telescope. In our experimental design, we closely follow the optimization described in this paper. From this they found that the optimal angle of incidence θ_i on the diffraction grating is given by

$$\sin(\theta_i) = \frac{\lambda_0}{d}\left(1 - \frac{a}{n n_g}\right). \tag{2.7}$$

Here, d is the spacing between grooves on the diffraction grating, λ_0 is the pump wavelength, and n and n_g are the refractive indices of the $LiNbO_3$ crystal for the phase and group velocities respectively. The parameter a is as follows:

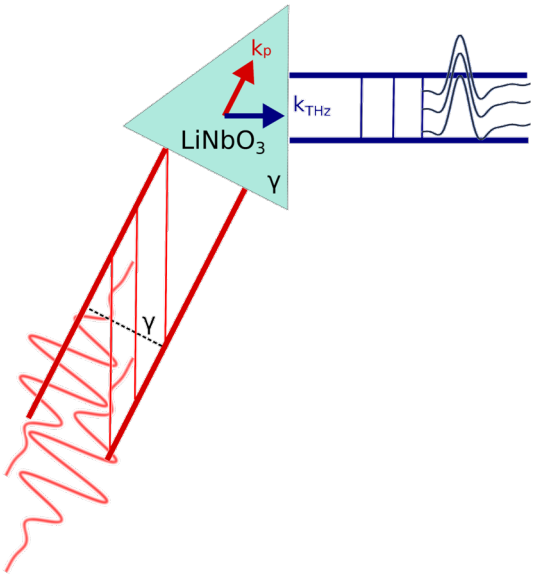

Figure 2.4: Sketch of the tilted pulse front technique for efficient THz generation by Optical Rectification. The propagation direction of the pump pulse is given by k_p and the propagation direction of the THz pulse is indicated by k_{THz}. The red and blue waves represent the pump and output THz profiles respectively, and the vertical lines indicate the constant phase wave fronts.

$$a = \frac{n^2 n_g p}{2\lambda_0}\sqrt{\frac{\lambda_0^2}{n_g^2 p^2 \tan^4(\gamma)} + \frac{4}{n^2}} - \frac{n^2}{2\tan^2(\gamma)}. \tag{2.8}$$

In this equation γ is the pulse front tilting angle corresponding to the angle of the $LiNbO_3$ prism and $p = 1/d$ is the grating periodicity.

The diffraction angle θ_d is directly obtained from the diffraction equation

$$\sin(\theta_i) = \frac{\lambda_0}{d} - \sin(\theta_d). \tag{2.9}$$

In addition, the optimal ratio between the focal lengths of the two cylindrical lenses is [130]:

$$\frac{f_1}{f_2} = \sqrt{a}. \tag{2.10}$$

Finally, we chose the optimal groove density on the grating for the highest THz generation efficiency, which is given by [129]

$$p = \frac{\lambda_0}{2}\sqrt{1 + \frac{2n}{n_g \tan^2(\gamma)}}. \tag{2.11}$$

We use a 1800 grooves/mm grating to create the tilting of the pulse front. We employ the above equations to find the optimal ratio $f_2/f_1 = 0.6$. This ratio is typically used for the imaging optics for intense THz generation using a tilted pump pulse front. Hence, we use cylindrical lenses with focal lengths of $f_1 = 100$ mm and $f_2 = 60$ mm. In addition, we place a half-wave plate in between these lenses, to allow control of the polarization state of the pump pulse. The half-wave plate allows us to rotate the polarization of the pump pulse along the z-axis of the $LiNbO_3$ crystal, for which the THz generation is found to be optimal [131].

The diffraction angle was set such that the angle of incidence was 38°, such that the pulse front would be tilted by 62°. All of the optics are aligned using a pyroelectric THz detector. The maximal THz pulse energy found using this pyroelectric detector is approximately 4.5 µJ.

After generation of the THz pulse, it needs to be transported to the sample. As the water molecules in humid air have absorption bands around the center of the THz pulse (1.2 THz [132]) (see next section), the pathlength of this transport should be as short as possible, or the THz should propagate through dry air. To this end, we designed a purging box enclosing the THz generation setup, through which dry air flows.

Finally, the generated THz signal is transported to the sample. Due to the internal reflections in the $LiNbO_3$ crystals, we need to make sure these reflections are blocked and cannot accidentally reach the sample, as the high power may damage the sample. To this end, we place a stack of two 1 mm thick teflon plates directly after the $LiNbO_3$ prism, as this blocks 800 nm light and transmits THz well ($T_{\text{teflon}} \approx 95\%$). Finally the beam is transported to and focused on the sample. To this end, we use three parabolic mirrors, with focal lengths of 1 inch, 6 inch and 2 inch respectively. In the next section, more details will be given on the choice for the parabolic mirrors.

We use a set of two wire-grid polarizers to control the polarization of the THz pulse. As the transmitted electric field through such a polarizer is $E = E_0 \cos(\theta)$, where θ is the angle between the polarization of light and the transmissive axis of the polarizer, the use of the polarizers allows us to control the intensity of the THz pulses irradiating the sample.

Finally, we have the possibility to place the sample in a closed-cycle liquid Helium cryostat, that allows us to control the sample temperature down to 3 K.

2.3.3 Focusing of the THz pulse

One of the major challenges in the field of THz optics is the relatively long wavelength of THz radiation. The wavelength of the THz sources lies in the sub-millimeter range (1 THz ≈ 0.3 mm).

Because the minimal achievable beam waist is proportional to the wavelength of the

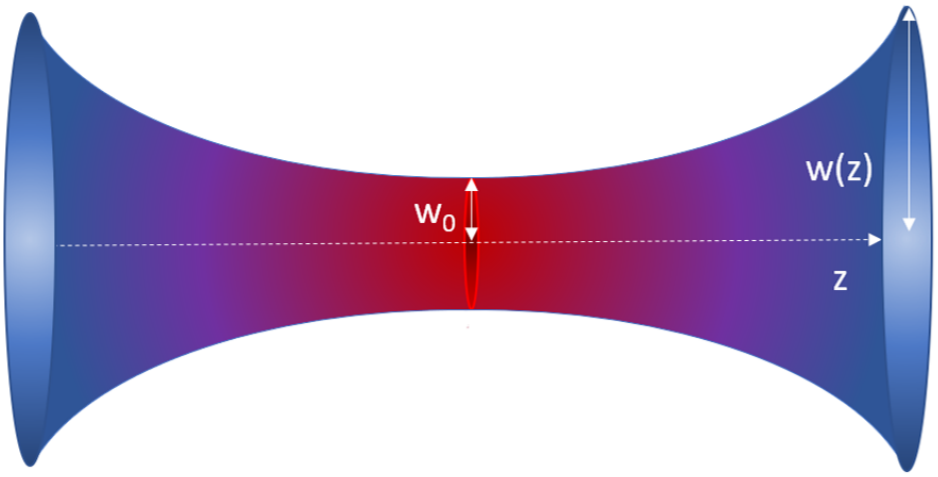

Figure 2.5: Illustration of the propagation of a Gaussian beam going through a focus. The beam radius is indicated with $w(z)$, and the radius of the beam waist is w_0.

light, it is significantly more challenging to tightly focus THz frequency light than the more commonly used visible or near-infrared light pulses. Besides, the THz beams experience a strong divergence due to their long wavelength, as can be seen from equation (2.12) [133].

$$w(z) = w_0 \sqrt{1 + \frac{\lambda z^2}{\pi w_0^2}} \tag{2.12}$$

Here $w(z)$ is the spot size at distance z from the beam waist w_0 (figure 2.5).

The minimal spot size of a Gaussian laser beam after focusing with an optic is given by

$$w_0 = \frac{4 f \lambda}{\pi w^2} \tag{2.13}$$

and is thus proportional to the ratio of the focal length of the focusing optic and the beam diameter before the focusing optic. This fact needs to be exploited to reach the highest peak electric fields of the THz light as possible, by using the optic with the shortest focal length, and THz beam with the largest diameter possible. However, the focal distance and the expansion of the beam are restricted by geometric limitations in the setup.

The above equations can be written in a more general form in terms of a beam parameter q, transformed after propagation through space or after passing through an arbitrary optical element. This beam parameter is defined as

$$\frac{1}{q} = -i \frac{\lambda}{\pi w^2} + \frac{1}{R}. \tag{2.14}$$

Thus, we see that the beam parameter is a complex value, where the imaginary part

describes the waist of the beam and the real part describes the radius of curvature of the beam. Therefore, to find the optimal set of parabolic mirrors, we performed numerical calculations on the evolution of this beam parameter during propagation between the parabolic mirrors using 2x2 ray transfer matrices, also referred to as the ABCD matrices [134].

The ABCD transformation matrices for beam propagation over distance z (M_{prop}) and focusing by a parabolic mirror (M_{pm}) are given by

$$M = \begin{pmatrix} A & B \\ C & D \end{pmatrix}, \quad M_{\text{prop}} = \begin{pmatrix} 1 & z \\ 0 & 1 \end{pmatrix}, \quad M_{\text{pm}} = \begin{pmatrix} 1 & 0 \\ -\frac{1}{f} & 1 \end{pmatrix} \tag{2.15}$$

Defining the beam parameter as the vector $\mathbf{q} = \begin{pmatrix} q \\ 1 \end{pmatrix}$, the beam parameter then transforms as

$$q' = \frac{Aq + B}{Cq + D}. \tag{2.16}$$

Using such matrices is convenient, as the resulting transformation matrix can simply be obtained by matrix multiplication. After transformation of the beam parameter, we can then finally retrieve the spot size at any point in the propagation path from the imaginary part of the beam parameter, as seen from equation (2.14).

$$w = \sqrt{\frac{-\lambda}{\pi \text{Im}(1/q(z))}} \tag{2.17}$$

In our simulations, we assume that the radius of curvature of the wavefront of the THz is negligible after the generation. We assume an initial spot size of $w_i \approx 3$ mm directly after the $LiNbO_3$ prism, as was found with knife-edge measurements (see following section). The results of this simulation are shown in figure 2.6.

Care must be taken during the alignment of parabolic mirrors. With improper alignment, the resulting beam spot may become elliptical. As THz is invisible by the human eye and challenging to visualize without advanced equipment, we used an auxiliary HeNe laser to align the parabolic mirrors.

The size and profile of the THz pulse can be determined experimentally using a variety of methods. For instance, the THz beam profile can be imaged with a THz camera to estimate the THz beam diameter. Alternatively, for more accurate beam size determination, knife-edge measurements can be performed. For illustration, an example of THz camera measurement and a knife-edge measurement in the focal spot of the THz beam is shown in figure 2.7.

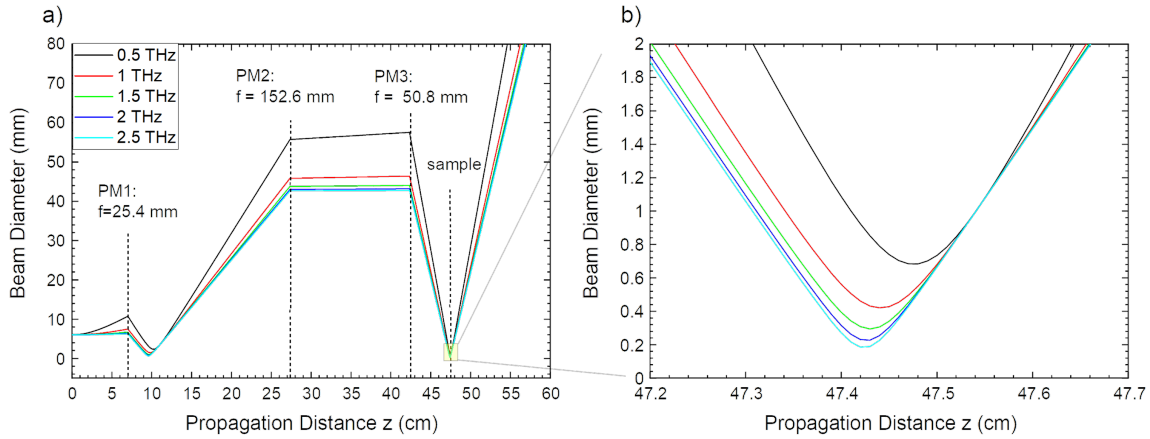

Figure 2.6: a) Simulation of the evolution of the beam size after propagation and focusing with the parabolic mirrors for various frequencies in the THz pulse. The positions and the focal lengths of the three parabolic mirrors (PM) and the position of the sample is indicated. b) Zoom-in around the sample position, indicating the spot sizes in the focus.

The image taken with the THz confirms that the THz pulse is focused properly in a circular spot. To obtain the spot size in the THz focus, we fit the knife-edge measurement with the Error Function (the integral of a cut-off Gaussian), and found that the FWHM of the Gaussian profile is 0.5 mm.

2.3.4 Electro-Optic Sampling

The generated THz pulses can be resolved in the time domain by electro-optic sampling (EOS). The technique of EOS is a nonlinear optical technique where the birefringence of the crystal is modified under external electric fields. As a result of the electric field component of the THz pulse that passes through the crystal, the probe passing through the detection crystal will become slightly elliptically polarized. Similarly to how the half-wave plate is used to balance the polarization rotation, we use a quarter-wave plate to balance the ellipticity. The THz-induced ellipticity will similarly result in a change in the difference in signal on the photo-detectors. Thus, by varying the delay between the THz and the probe pulse, the profile of the THz pulse in the time domain can be revealed.

For our EOS measurements, we used a 100 µm thick GaP nonlinear detection crystal, for the relatively high response and broad detection bandwidth [135]. This crystal was placed in the sample position in the experimental scheme that was illustrated in figure 2.3.

The THz profiles measured in this way are shown in figure 2.8. The spectra under normal circumstances and when the setup is enclosed and purged with dry air are compared.

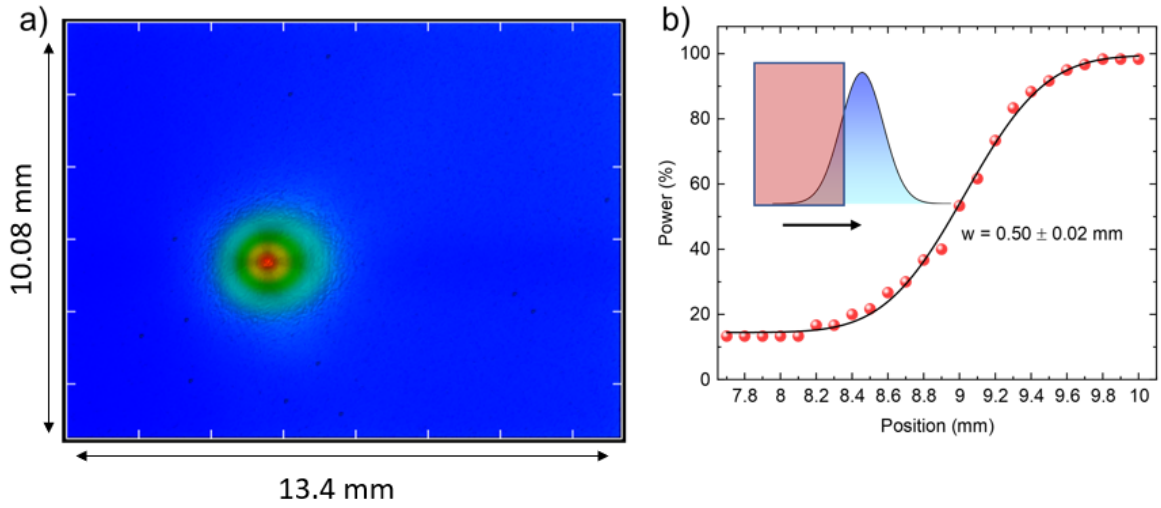

Figure 2.7: a) Image of the THz spot in the focus measured with a THz camera. b) Measurement of the diameter of the beam with the knife-edge method. The result is fitted with the Error Function, and the resulting FWHM of the Gaussian is indicated.

2.3.5 Calibration of the THz Electric field

In this section, we discuss how the THz electric field can be calibrated. Note that in this section, the equations will describe the calibration is SI units. The ellipticity induced in the probe pulse by the THz pulse as measured in EOS scales linearly with the THz electric field. Knowledge of the proportionality factor will thus allow for a proper calibration of the THz electric field strength.

For the arbitrary orientation of the input polarization direction of the THz (α) and probe (ϕ) with respect to the crystallographic c-axis of the detection crystal, the ellipticity induced by the THz pulse is given by [136]

$$\frac{\Delta I}{I_0} = \frac{\omega n^3 E_{\mathrm{THz}} r_{41} L}{2c}\left(\cos(\alpha)\sin(2\phi) + 2\sin(\alpha)\cos(2\phi)\right). \tag{2.18}$$

Here, ΔI is the difference signal due to the ellipticity on the photo-detectors for a static detector signal I_0, ω is the angular frequency of the probe pulse, $r_{41} \approx 0.5\,\mathrm{pm/V}$ is the nonlinear optical coefficient of GaP [137], L is the crystal thickness, and c is the speed of light. Due to the large refractive index of the THz in the detection crystal, a large fraction of pulse will be reflected. The transmission of the THz into the detection crystal is

$$t = 1 - r = 1 - \left|\frac{n_1 - n_2}{n_1 + n_2}\right|. \tag{2.19}$$

Assuming the refractive index of THz in GaP is approximately 3.4 [138], we find that only

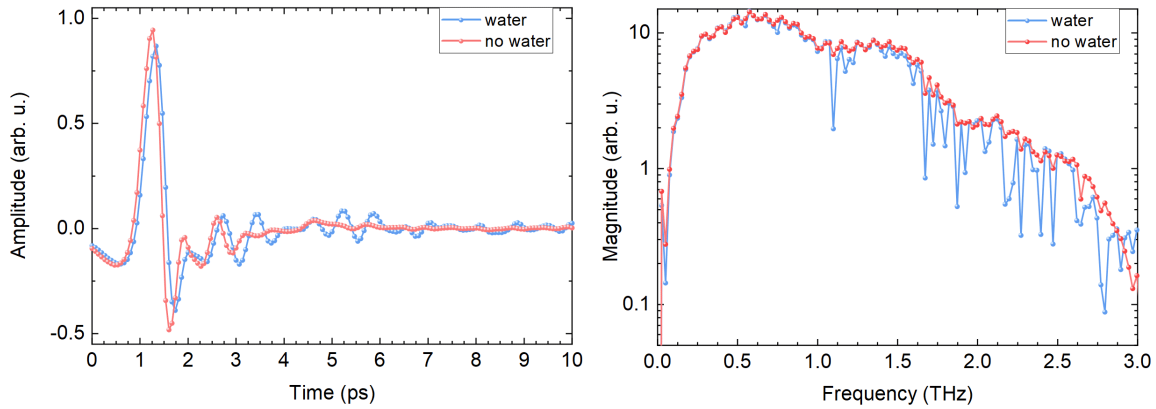

Figure 2.8: THz pulses (a) and their spectrum (b) generated with the tilted pulse front and measured with EOS, in humid and dry air.

45% of the THz field passes into the detection crystal.

Also accounting for the absorption by the teflon plates,and setting the pump and probe polarization ideal ($E_{\mathrm{pr}}||c$,$E_{\mathrm{THz}} \perp c$) we find that the THz field is

$$E_{\mathrm{THz}} = \frac{\Delta I}{I_0} \frac{2c}{\omega n^3 r_{41} L t_{\mathrm{tef}} t}. \tag{2.20}$$

where t_{tef} is the transmission coefficient of the THz through the teflon plates. The electric field that we typically retrieve using this method, is 300 kV/cm. We noted that THz electric field after extensive optimization of the setup is always lower than the previously reported values of more than 1 MV/cm for similar experimental configurations [130].

Therefore, we decided to compare this calibration with an alternative approach with the measured power. The energy of the THz pulse U can be expressed as the spatial integral of the square of the electric field.

$$U = \int_{-\infty}^{\infty} \frac{1}{2} \epsilon_0 E^2(\mathbf{r}) dV \tag{2.21}$$

We can assume the transverse profile of the pulse to be Gaussian with the FWHM determined from the beam profiling measurements and the longitudinal profile can exactly be probed through EOS. Knowing the integral over the Gaussian, we get

$$E_0 = \sqrt{\frac{2U}{\epsilon_0 \pi d^2 \int E(z) dz}}. \tag{2.22}$$

We calculate the integral over $E(z)$ numerically using the experimentally obtained EOS scans.

As a result, we find that for the measured spot size of 0.5 mm FWHM, the resulting electric field is approximately 1 MV/cm, more closely matching the previously reported values.

2.3.6 Outlook

After extensive usage of our setup, we believe that the setup is still susceptible to some improvements. We found that in practice, the parabolic mirrors are not completely filled yet, allowing us to expand the THz beam more by changing the focal length of the parabolic mirror that collects the THz from the prism. A recent improvement involved the replacement of this parabolic mirror to one with shorter focal length (25 mm $\rightarrow$ 15 mm). This allows for the further expansion of the beam, and thus tighter focusing. Indeed, we found that the EOS signals with GaP improved by approximately a factor of 2, and confirmed the reduction of the spot size by a factor 2, both with the knife-edge and THz camera measurements

Moreover, the diameter of the parabolic mirrors may be increased further to 3 inch to allow for even further beam expansion and thus tighter focusing. However, such a configuration would come with spatial restrictions in the experimental setup.

Additionally, we noticed that the output power of the THz does not depend strongly on the input power of 800 nm, implying that the THz generation is in the saturation regime. Therefore, we may consider to expand the input 800 nm beam further using a telescope and use a bigger $LiNbO_3$ prism, for example with dimensions 20 mm$\times$20 mm.

Chapter 3

Theory of the generation and detection of propagating THz magnons in antiferromagnets

In this chapter, we theoretically describe the optical generation and detection of propagating packets of spin waves in antiferromagnets, by solving the equations of motions for the spin system in response to a light induced effective magnetic field. The model discussed in this chapter will be valid for small spin deflections, thus in the linear regime. We apply the model to a variety of pulses that can launch spin excitations, from simple approximations to realistic experimentally available light pulses, and analyze the waveforms of the resulting spin waves. Then we theoretically show the selective detection of the spin waves by the magneto-optical Kerr Effect.

3.1 Introduction

Propagating waves of spin precession, whose quanta are referred to as magnons have attracted a lot of interest over the last decades, for their potential to replace to current electronic based techniques of storing and processing information [139]. However, until recently it has proven to be extremely challenging to generate such spin waves. Currently, ferromagnets have been mostly studied, where the resonance frequencies lie in the GHz range, whereas antiferromagnetic materials exhibit much faster spin dynamics, in the THz range. Moreover, to compete with the miniature scales at which data can be stored and processed today, it is crucial to excite magnons with nanoscale wavelengths [140]. This has been particularly challenging by optical means, as the minimal spot size of an optical excitation is typically

restricted to be on the micrometer scale.

As a result, the spin waves that were excited in ferromagnetic systems typically had long wavelength as characterized by the magnetic dipole interaction. Exchange dominated spin waves can however go down to the nanometer wavelength scale. It has been proposed that such exchange dominated magnons in ferromagnets can be realized by fabricating an antiferromagnetic layer on top of a ferromagnetic layer. These layers are strongly coupled by the exchange bias, and the excitation of the antiferromagnetic layer acts as a strongly localized effective field in the ferromagnetic layer, resulting in the emission of spin wave with nanometer scale wavelength, propagating normal to the interface [141]. Theoretical studies have also shown that it is possible to generate short wavelength spin waves in ferromagnets by a microwave excitation at the interface of two coupled ferromagnetic layers. The inhomogeneity due to this interface allows spin waves to be emitted in the material, with their amplitudes depending on the difference between the magnetic susceptibility of the two materials. As the resonance frequencies of antiferromagnets is far from the resonance frequency of the ferromagnets, spin wave generation from the interface of ferromagnets and antiferromagnets has been considered highly promising [142].

However, the excitation of short wavelength and high frequency spin waves in antiferromagnets has proven another challenge. Although short wavelength and high frequency magnons have recently been achieved in thin films, these magnon modes involved only standing waves, thus these spin waves do not propagate [143]. A breakthrough was made in 2021, when propagating packets of spin waves were reported for the first time in $DyFeO_3$ by the optical excitation with photons having energies exceeding the band gap energy of the antiferromagnet [70]. As a result, the photons responsible for the excitation of the magnons remain confined in a nanoscale region near the sample boundary. As a result of this strongly inhomogeneous excitation, a propagating wavepacket of spin waves will propagate away from this region, into the material. This concept is illustrated in figure 3.1.

The concept of the laser confinement is illustrated in figure 3.1a). A pump pulse with photon energy of 3.1 eV (400 nm) excites the spin precession. As the inset shows, this photon energy corresponds to an electronic transition, that results in the strong absorption of the photons in a region of approximately 50 nm to the boundary. The spin precession launched in this region transfers to the neighboring spins in the form of propagating spin wave with supersonic velocity v_0. The spin dynamics is then detected by a second weaker probe pulse. As seen from figure 3.1b) and 3.1c), the detected dynamics will occur at very different frequencies depending on whether the dynamics is detected in a transmissive or reflective configuration.

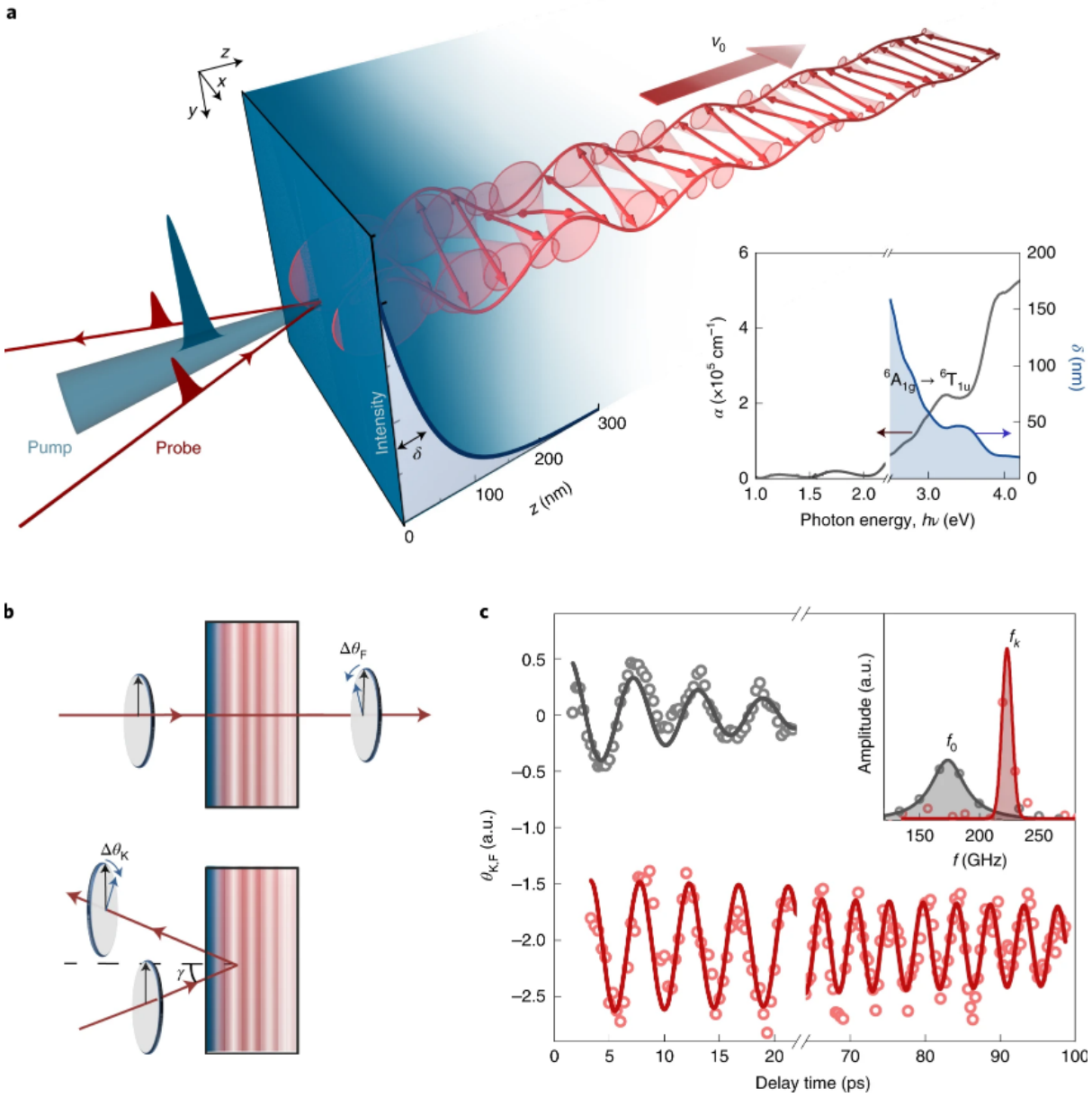

Figure 3.1: Illustration of the first observation of propagating THz spin waves in an antiferromagnet. Figure from reference [70].

In this chapter, a thorough description from a theoretical viewpoint will be given to explain the previously performed experiment. The first part of the chapter will discuss numerical simulations on the generation of these spin waves, whereas the second part of the chapter will focus on the detection of these spin waves, and explain how different frequencies are observed in the pump-probe experiment with the transmissive and reflective configuration.

3.2 Model

In figure 3.2, a schematic of our model is depicted. As mentioned before, we consider the canted antiferromagnet in the magnetic Γ_4 phase, where the ferromagnetic moment **M** is oriented along the z-axis and the antiferromagnetic moment **L** is oriented along the x-axis. The spins are excited with a strongly absorbed laser pulse, that is therefore confined to a region of $d = 50$ nm near the boundary. The light pulse acts as an effective magnetic field by changing the magnetic parameters of the system [64]. As discussed in Chapter 1, such effective fields may for instance arise from thermal effects such as the light-induced changes to the magnetic anisotropy [144, 145], exchange interaction [146, 147] or other internal magnetic interactions, but also from non-thermal effects such as the Inverse Faraday Effect or the Inverse Cotton Mouton Effect. The spin waves are thus launched by the effective magnetic field component of the laser pulse $\mathbf{h}(z, t)$ traveling in the z-direction (normal to the sample boundary). As the characteristic wavelength of the THz magnons (~ 100 nm) is much shorter than the typical diameter of a focused laser spot (> 1 μm), we can neglect the lateral Gaussian distribution of the laser pulse and may assume the excitation of the surface to be uniform. We account for the absorption of the laser pulse, resulting in an exponentially decaying spatial distribution of the effective field $h(z, t) = h_0 e^{-z/d}$ (see figure 3.2a). We consider only the spin wave propagation from the first boundary, as the penetration depth of the excitation is much smaller than the thickness of the sample. In addition, we assume that the lifetime of the spin wave is short enough for the spin wave to fully decay before reaching the boundary at the back of the sample, such that reflections of the spin waves may be ignored.

In the following section, we will first generally describe the solution and then consider the propagation of the spin waves for more specific examples of effective field profiles. After this, we model their detection in a typical pump probe experiment, where the polarization rotation induced by the dynamic magnetization is tracked as a function of the time delay after excitation by the pump pulse (figure 3.2b).

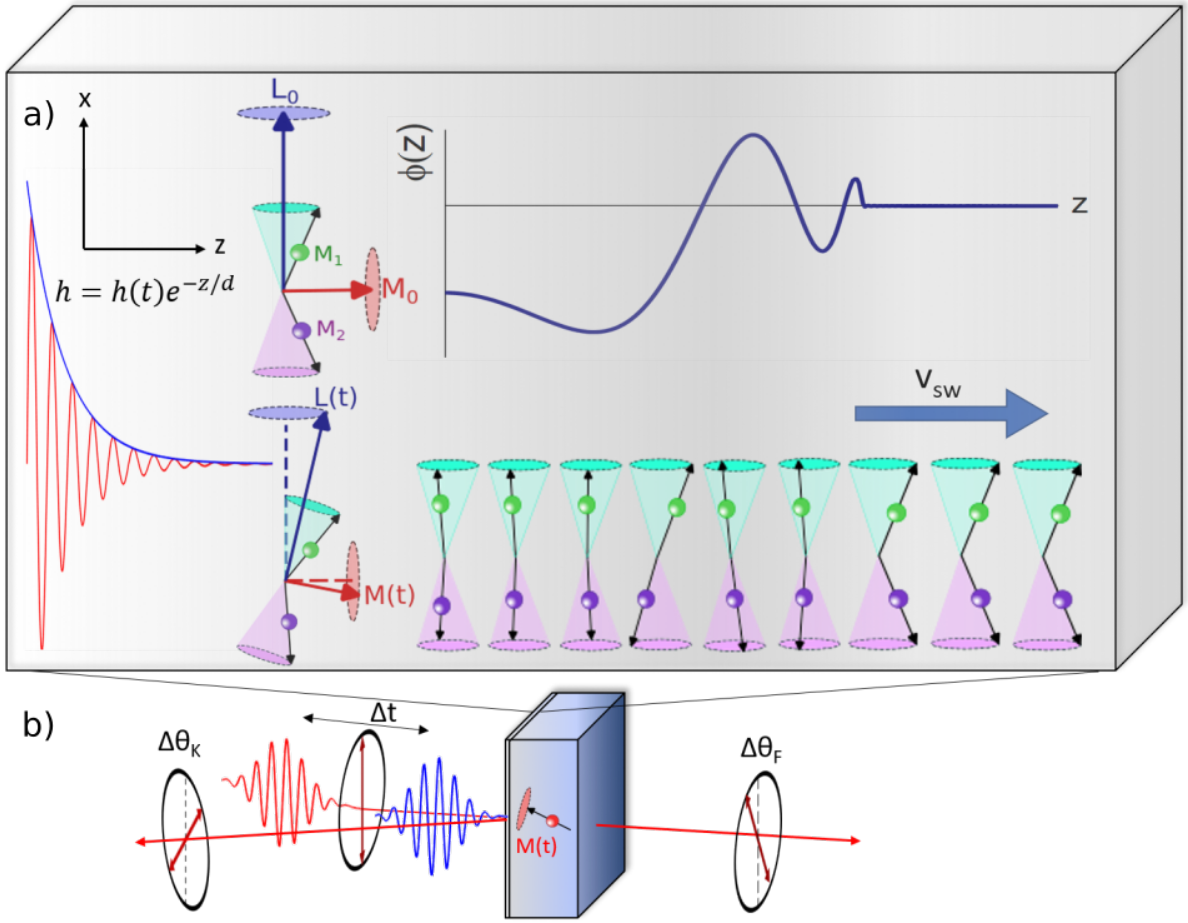

Figure 3.2: Schematic of the modeling of spin dynamics in a (canted) antiferromagnet. The spin dynamics is excited by the effective magnetic field induced by a laser pulse h(z,t), which is assumed to have an exponential decay into the medium as it is absorbed. The spin excitations near the boundary propagate into the medium as waves with velocity v_{sw}. b) The spin waves are magneto-optically detected by a second laser pulse arriving after a time delay Δt. The dynamic magnetization gives rise to the Faraday rotation $\Delta\theta_F$ in the transmission configuration, or the Kerr rotation $\Delta\theta_K$ in the reflective configuration.

3.3 Spin wave generation

3.3.1 General solution

With the obtained Klein-Gordon for both modes in the antiferromagnets, we can model how the spin waves propagate after excitation with a laser pulse. As the mode that was observed experimentally most closely matched to the q-AFM mode, we will describe in the following only the equation for this mode. We take the last equation of equation (1.24) and convert the component l_y into the angle of spin deflection as $l_y = L_0 \sin(\phi) \approx L_0 \phi$ for small deflection angles and obtain the following:

$$\frac{\partial^2 \phi(z,t)}{\partial t^2} + 2\alpha \frac{\partial \phi(z,t)}{\partial t} + (\omega_0^2 - v_{\mathrm{sw}}^2 \nabla^2)\phi(z,t) = -\omega_h \frac{\partial h(z,t)}{\partial t}. \tag{3.1}$$

In the absence of the effective field, the solution of this equation will be a plane wave $Ae^{i(\omega t - k(\omega) z)}$. By substituting this plane wave expression in equation (3.1) the dispersion relation for antiferromagnets is obtained:

$$\omega^2 = \omega_0^2 + v_{\mathrm{sw}}^2 k^2 + 2i\alpha\omega, \tag{3.2}$$

where ω is the angular precession frequency, and k is the wave number of the propagating magnon.

The full solution to equation (3.1) can most easily be found in the frequency domain, after performing the Fourier transformation

$$-\omega^2 \tilde{\phi}(z,\omega) + 2i\alpha\omega\tilde{\phi}(z,\omega) + (\omega_0^2 - v_{\mathrm{sw}}^2 \nabla^2)\tilde{\phi}(z,\omega) = -i\omega\omega_h \tilde{h}(z,\omega), \tag{3.3}$$

where $\tilde{\phi}(z,\omega) = \int_{-\infty}^{+\infty} \phi(z,t) e^{-i\omega t} dt$ denotes the Fourier Transformation of the spin deflection and $\tilde{h}(z,\omega)$ denotes the Fourier transform of the effective field. Only the profiles of the effective fields will be considered that can be driven as a product of a time- and a space-dependent functions. The spatial dependence of the effective field will be an exponential decay resulting from the absorption of the laser pulse:

$$\tilde{h}(z,\omega) = \tilde{H}(\omega) e^{-z/d}. \tag{3.4}$$

Here d is the penetration depth of the laser excitation. Since the diameter of the laser spot is much larger than the excitation depth and the wavelength of the spin waves, we assume that the spin waves propagate uni-directionally, normal to the sample surface. We can then see that the full solution for the spin deflection is

$$\tilde{\phi}(z,\omega) = A_f(\omega)e^{-ik_{\mathrm{sw}}(\omega)z} + A_p(\omega)e^{-z/d}. \tag{3.5}$$

The first term in equation (3.5) corresponds to the solution for freely propagating magnons, where $A_f(\omega)$ is the spectral amplitude of the freely propagating waves and $k_{\mathrm{sw}}(\omega)$ is the wavevector determined by the dispersion relation (equation (3.2)). The value of $k_{\mathrm{sw}}(\omega)$ is complex, and the imaginary part is responsible for the spatial decay of the spin wave. To ensure this, the complex value of k_{sw} is defined as $k_{\mathrm{sw}} = \kappa - i\eta$, where κ and η are real. The second term in equation (3.5) corresponds to the forced spin precession driven by the effective magnetic field of the laser pulse. The spectral amplitude $A_p(\omega)$ of this driven spin precession is directly obtained from equation (3.3).

$$A_p(\omega) = \frac{-i\omega\omega_h\tilde{H}(\omega)}{-\omega^2 + \omega_0^2 + 2i\alpha\omega - v_{\mathrm{sw}}^2/d^2} \tag{3.6}$$

To find the amplitude of the freely propagating spin wave, it is required to specify the boundary conditions. We apply the exchange boundary condition, which reads [148]

$$\frac{\partial\phi}{\partial z}(z=0) + \xi\phi(z=0) = 0. \tag{3.7}$$

The pinning parameter ξ determines the stiffness of the spins at the surface. In the case of $\xi = 0$, spin deflections can occur freely at the boundary, whereas for $\xi \to \infty$, spin deflections at the surface are forbidden. Applying these boundary conditions to expression (3.5) allows us to relate the amplitudes of the free and forced solutions:

$$A_f(\omega) = A_p(\omega)\frac{1/d - \xi}{\xi - ik_{\mathrm{sw}}(\omega)}. \tag{3.8}$$

Finally, the inverse Fourier transform can be applied numerically to equation (3.5) to obtain the evolution of the spin waves in the time domain. In the remainder of this section, the results of these calculations will be discussed for several indicative effective magnetic field profiles. The general method of obtaining the results is as follows: The spectrum of the exciting field $\tilde{H}(\omega)$ is calculated (for most cases this can be done analytically), and the spectrum of the spin deflection is calculated for each of the coordinates z, using equation (3.5). Then, all these spectra are separately inverse Fourier transformed into the time domain, to obtain the spin deflection at each spatial coordinate as a function of time. Thereby, we create a two dimensional map, with the spatial coordinate on the horizontal axis and the temporal coordinate on the vertical axis as illustrated in figure 3.3. By selecting the horizontal cross-sections of this map, we thus obtain the spatial profile of the spin wave deflections at a

given time. By shifting the cross-section continuously, movies that illustrate the propagation of the wave packet can be made. Such movies are available in the supplemental materials to reference [149].

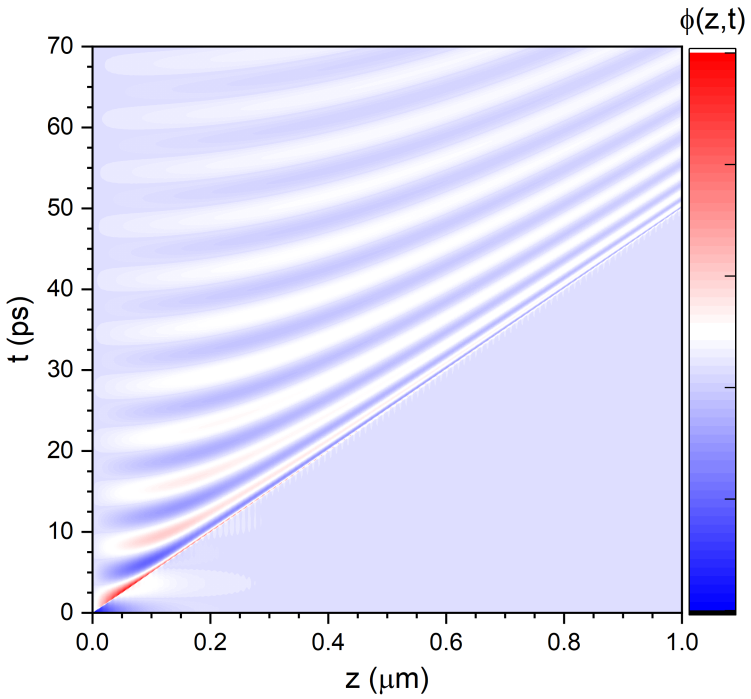

Figure 3.3: Example 2D map of the spin deflection $\phi(z,t)$ with the time coordinate along the vertical axis and the spatial coordinate along the horizontal axis for the impulsive excitation.

3.3.2 Impulsive excitation

The simplest case that can be considered is the impulsive excitation, where the laser pulse is modelled to be infinitesimally short in time: $h(t) = \tau h_0 \delta(t)$, where the typical laser pulse duration $\tau = 0.1$ ps is used to normalize the Dirac delta function. This approximation describes well typical experiments with femtosecond pump pulses acting as opto-magnetic fields, which are much shorter than the period of antiferromagnetic modes. Performing the Fourier transform of the effective field $h(t)$, we obtain for the driven solution:

$$A_p(\omega) = \frac{-i\omega\tau\sqrt{\pi}\omega_h}{-\omega^2 + \omega_0^2 + 2i\alpha\omega - v_{\mathrm{sw}}^2/d^2}. \tag{3.9}$$

In our simulations, we choose the following set of parameters: $\omega_0 = 2\pi \times 0.15$ THz, $\alpha = 10^{-2}\omega_0$, $d = 50$ nm, $c = 20$ nm/ps [66, 70]. The results of the simulations are shown in figure 3.4a) for the pinned boundary condition and figure 3.4b) for the free boundary condition.

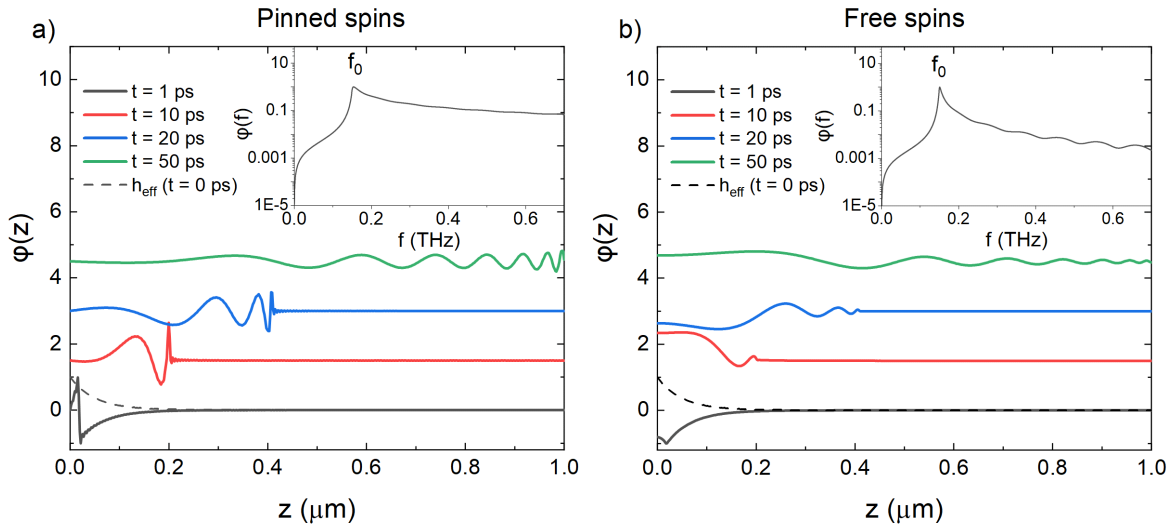

Figure 3.4: Snapshots of the spin waves for an impulsive excitation profile. a) The spin waves at various time points for the pinned boundary condition. b) The spin waves at various time points for the free boundary condition. In both panels, the dashed lines represent the profile of the effective field acting at t=0 ps and the insets show the corresponding spectra at a distance of $z = 0.2\,\mu$m from the boundary. All snapshots are normalized to the maximum absolute value of the spin deflection at $t = 1$ ps.

The main panels display the snapshots of the propagating packets of the spin waves, as obtained by the numerical inverse Fourier transform of equation (3.5). Note that these plots are normalized to the maximum absolute value of the magnetization of the snapshot at $t = 1$ ps. In the insets, the spectra at a point of $z = 0.2\,\mu$m from the boundary are shown. We notice that the spectrum in the pinned boundary condition is much wider than the spectrum in the free boundary condition, giving rise to higher frequency components and a more pronounced wavepacket with slightly shorter wavelengths as compared to the spin waves in the free boundary condition.

3.3.3 Displacive excitation

The next pulse profile that we consider is the displacive excitation, where the spin deflection is continuously excited, but with a over time decaying excitation amplitude: $h(t) = \Theta(t)e^{-\beta t}$, where $\Theta(t)$ is Heaviside step function and $1/\beta$ is the lifetime of the excitation. This model accounts for the abrupt photoinduced change in magnetic anisotropy, which may slowly decay in time [150]. We take the same modelling parameters as for the impulsive excitation, with a modified frequency distribution

$$A_p(\omega) = \frac{-i\omega\omega_h}{(\beta + i\omega)(-\omega^2 + 2i\alpha\omega + \omega_0^2 - v_{sw}^2/d^2)}. \tag{3.10}$$

If we consider the case $\beta >> \omega_0$, the lifetime of the excitation is much shorter than a single oscillation, and as a result the excitation can again be approximated by the Dirac delta function. We confirmed that indeed for these short lifetimes of the effective fields, our simulation yields identical results to the ones shown in figure 3.4. For the case $\beta << \omega_0$, the decay of the excitation is slow, and the effective field will act during many spin oscillations. The resulting spin waves for $\beta = 0.001\omega_0$ are depicted in figure 3.5.

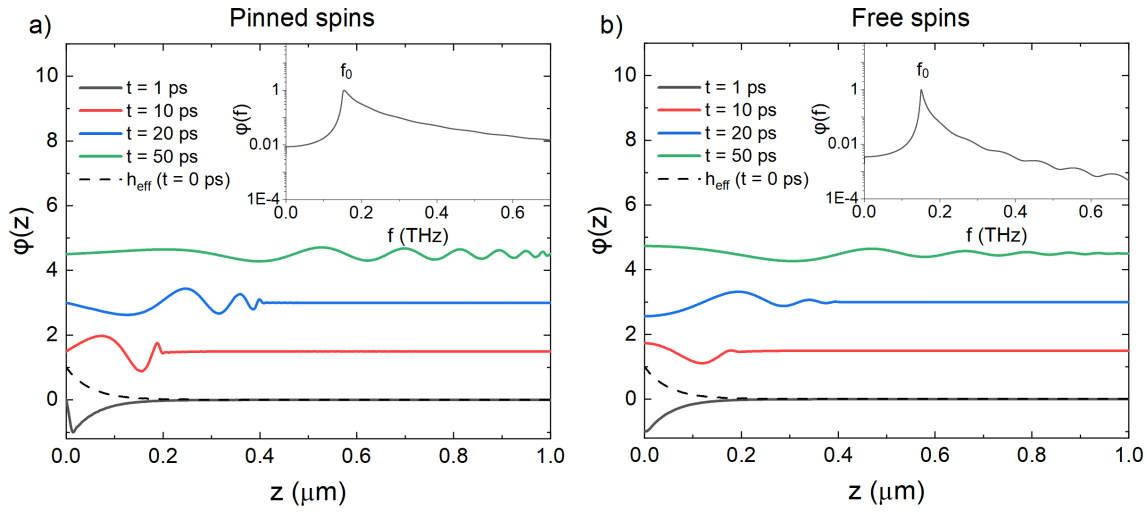

Figure 3.5: Snapshots of the spin waves excited by the displacive excitation for a) the pinned boundary conditions and for b) the free boundary conditions, and the excitation damping parameter $\beta = 0.001\omega_0$. The dashed lines represent the profile of the effective field acting at t=0 ps. The insets show the corresponding spectra at a distance $z = 0.2\,\mu$m from the boundary. The spin waves are normalized to the maximum absolute value of the spin wave at $t = 1$ ps.

Note that these conditions also quite closely correspond to the impulsive excitation of the q-FM mode, as the derivative of the slowly decaying step function can be approximated as the Dirac delta function, and the driving torque of the q-FM mode is proportional to the effective field, whereas the driving torque of the q-AFM mode is proportional to the derivative of the effective field.

3.3.4 Propagating Gaussian excitation

Here we consider a more experimentally realistic scenario, exciting the spin dynamics with a propagating Gaussian laser pulse, propagating through the medium with the velocity of

light $v_{\text{opt}} = c/n$. We again account for the absorption of this pulse near the boundary, and approximate the refractive index of the medium to be $n \approx 2.3$, which is a typical value for the antiferromagnetic oxides such as $DyFeO_3$. We model the propagating Gaussian pulse as

$$h(z,t) = h_0 e^{-(t-z/v_{\text{opt}})^2/\tau^2} e^{-z/d}. \tag{3.11}$$

In the Fourier domain, the solution is then given by

$$\tilde{\phi}(\omega,z) = A_f(\omega) e^{-ik_{\text{sw}}z} + A_p(\omega) e^{-z/d} e^{i\omega z/v_{\text{opt}}}. \tag{3.12}$$

The effect of propagation slightly modifies the relation between $A_f(\omega)$ and $A_p(\omega)$ through the boundary conditions:

$$A_f(\omega) = A_p(\omega) \frac{\frac{1}{d} - \xi + \frac{i\omega}{v_{\text{opt}}}}{\xi - ik_{\text{sw}}(\omega)}. \tag{3.13}$$

The spectral amplitude of the field-driven spin oscillations is now determined by the Fourier transform of the Gaussian envelope of the laser pulse, which is thus given by

$$A_p(\omega) = \frac{-i\omega\omega_h \tau\sqrt{\pi} e^{-\omega^2\tau^2/4}}{\omega_0^2 - \omega^2 - v_{\text{sw}}^2/d^2 + 2i\alpha\omega}. \tag{3.14}$$

To observe the effect of the propagation of the light pulse, we consider a transparent configuration by setting the confinement region of the effective field to $d = 0.5\,\text{cm}$. For the pulse width of the Gaussian pulse, we choose $\tau = 100\,\text{fs}$, which is a commonly used pulse duration in ultrafast pump-probe experiments. The spin waves launched by this propagating pulse are shown in figure 3.6.

As the velocity of light is much larger than the propagation velocity of the magnon, the oscillations as a result of the free magnon propagation and the driven spin precession by the effective field occur on very different length scales. Therefore, we distinguish the spin waves on the micrometer length scales in figure 3.6a) and on the centimeter length scale in figure 3.6b). These results are again shown for the pinned boundary conditions. From these results, we confirm that the propagating packets of spin waves decay within of a few micrometers. We can see these waves as the magnonic analogue to electro-magnetic transition radiation, arising from a discontinuity in the medium [151]. We see that the forced oscillations occur on the centimeter time scale, and this driven precession manifests itself as the quasi-uniform in-phase precession of the spins in the micrometer length scale. In the typical transmission pump probe experiments, the forced oscillations in the bulk dominate the measured response. As a consequence, in most experiments to date only these zero-wavenumber quasi-uniform

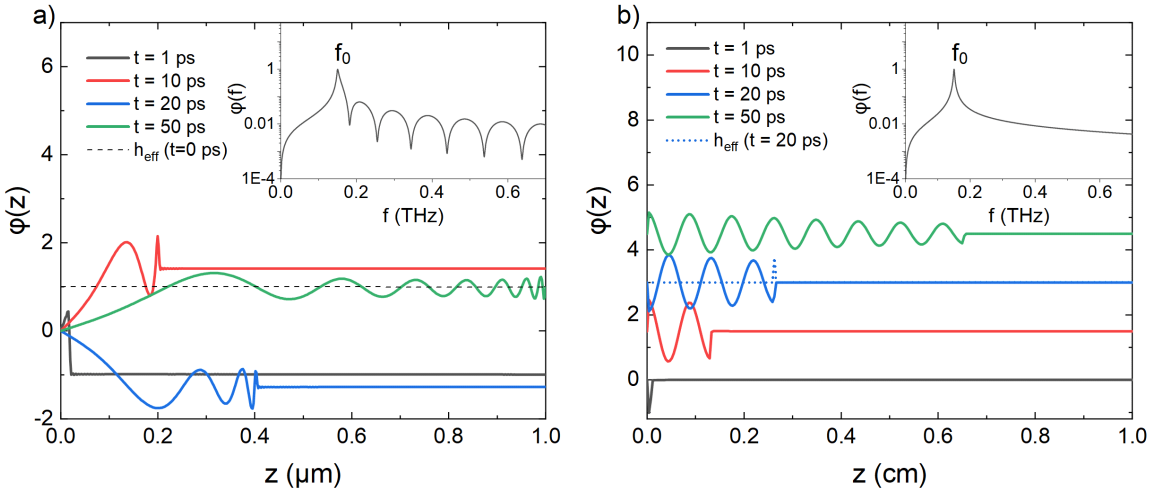

Figure 3.6: Snapshots of the propagating spin waves for a Gaussian propagating excitation in the pinned boundary condition a) in a region of a micrometer near the boundary and b) in a longer region of 1 cm into the bulk of the antiferromagnet. The wavelength of the spin wave in panel a) is determined by the inhomogeneity resulting from the pinned boundary condition, whereas the oscillating offset is a result from the uniform precession. In panel b), the wavelength is determined by the driven uniform precession and the propagation of the Gaussian pulse. The black dashed lines in a) and the blue dashed line in b) represent the effective fields at t=0 ps and t=20 ps respectively. The inset in a) shows the spectrum of the spin oscillation at a distance of $z = 0.2\,\mu$m from the boundary, and the inset in b) shows the spectrum at a distance $z = 0.4\,\mu$m from the boundary. The spin waves are normalized to the maximum absolute value of the spin wave at $t = 1$ ps.

oscillations were reported.

Furthermore, we note that in the absorptive configuration, ($d = 50$ nm) the spin profiles similar to the impulsive excitation mechanism are retrieved (figure 3.4) and we can conclude that the experimentally realistic laser pulse can be well approximated as an instantaneous impulsive excitation.

3.3.5 Propagating single cycle THz pulse

Although all the above cases allow for an analytical solution in the Fourier domain, any field profile may be used, simply by plugging the spectrum of this profile in equation (3.6). One of the most interesting cases to consider is the resonant excitation with a THz field, that oscillates on a picosecond time scale, comparable to the time scale of the spin oscillations. In this case, the spins are driven through the Zeeman torque induced by the magnetic field of the THz pulse [152]. The method of obtaining the spin wave profile is similar as described for the Gaussian excitation, with the amplitude of the driven solution now defined by the spectrum of the THz pulse. Again, we assume that the THz pulse propagates with the speed of light in the orthoferrite. For the refractive index of the THz pulse, we take $n \approx 5$ [153]. The simulation results are shown in figure 3.7.

In figure 3.7a), the THz pulse as we measured in the experiment (see Chapter 2 for more details) and its spectrum is shown. Although the measured pulse contains no propagation, we build in the propagation of the pulse in a similar manner to the Gaussian pulse, namely by introducing the phase factor $e^{i\omega z/v_{\mathrm{THz}}}$ to the Fourier transform, and then performing the inverse Fourier transform back to the time domain. Again, we separately consider the transmissive ($d = 0.5$ cm) and absorptive ($d = 50$ nm) configurations. Figure 3.7b) shows the snapshots of the propagation of the spin wave in the bulk in the free boundary condition for the transmissive configuration and see a similar result as for the propagating Gaussian excitation, with a small modification due to the fact that the spatial distribution of the propagating Gaussian will be slightly broader, and thus affects the field driven oscillation in the region near the wavefront. Finally, we shift our attention back to the region near the boundary for different conditions, and compare the spin waves in the pinned boundary conditions and the free boundary conditions for both the absorptive configuration and the transmissive configuration. In figures 3.7c-f) these cases are compared. We see that in the pinned boundary conditions, the waves are modified and the spatio-temporal features become visible. These features are most pronounced for the snapshots at short time delays, as the magnon wavefront is still close to the boundary. In the free boundary conditions, these ripples in the wavefront are not as clearly visible. Note that the freely propagating spin waves

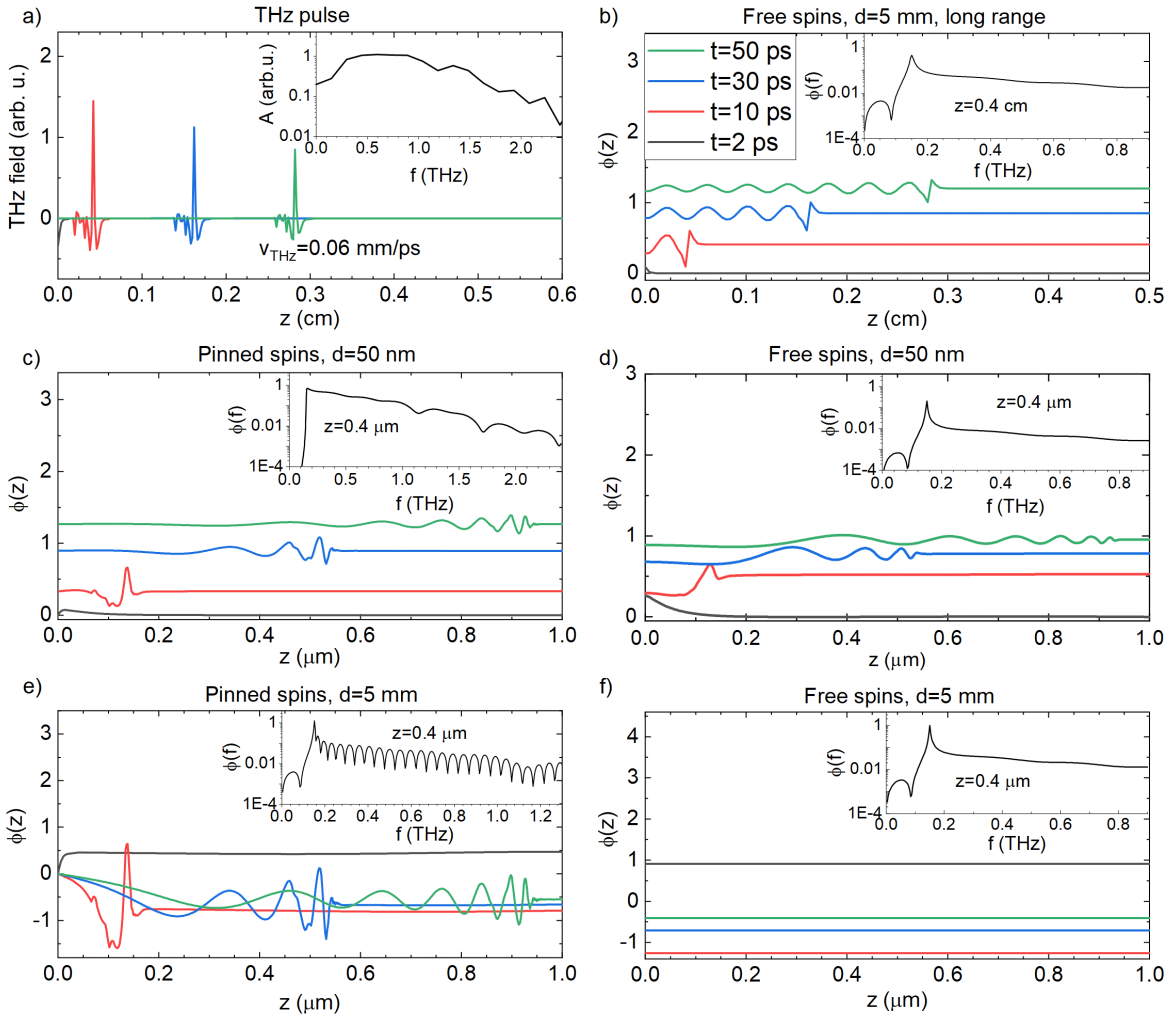

Figure 3.7: Spin waves induced by a propagating single cycle THz pulse. a) Snapshots of the propagation of an experimentally measured THz pulse, with its spectrum shown in the inset. b) Snapshots of the spin wave in the bulk for the free boundary condition, and a transparent configuration ($d = 0.5$ cm), induced by the propagation of the THz pulse. The inset shows the spectrum at $z = 0.4$ cm. c-f) Snapshots of the spin waves close to the boundary, for both boundary conditions, and for the transmissive and absorptive configurations.

in the transmissive configuration are only observed in the pinned boundary condition, as this boundary condition introduces a inhomogeneity in the spin excitation. In the free boundary condition, all spins, including the spins at $z = 0$ are allowed to precess, whereas in the pinned boundary condition, the spins at $z \neq 0$ will be deflected, and the spin at $z = 0$ remains in its equilibrium. This strong inhomogeneity gives rise to the freely propagating spin wave. Again, because the propagation velocity of the THz pulse is much faster than the propagation velocity of the free spin wave, all spins near the boundary are excited homogeneously, and the wavepacket becomes invisible. This highlights the essence of the inhomogeneity of the spin excitation, which may thus also be achieved by pinning the spins to the surface. As a result, the propagating packets of spin waves can also emerge in the transmissive configuration, without the need for the localization of the effective field driving the spins near the boundary. Finally, we note that for the same values of the effective magnetic field as were used in the previously discussed temporal excitation profiles, no significant changes in the amplitude of the spin waves are observed.

3.3.6 Effect of various parameters

In this section, we consider the excitation profiles discussed before, and investigate the effect of various parameters. In particular, the effect of the excitation depth d, the spin wave velocity limit v_{sw}, the pinning parameter ξ and the lifetime of the displacive excitation $1/\beta$ will be discussed. Comparisons of the spin wave profiles for a variety of these parameters are summarized in figure 3.8.

These figures confirm expectations about the behavior of magnons. Firstly, we see in figure 3.8a) that the confinement of the excitation to the boundary affects the spin wave profiles, as for reducing values of d, the exponential decay arising from the quasi-uniform driven precession disappears, and a stronger contribution of the freely propagating packet of spin waves emerges. Long excitation depths result in the emergence of a background on the oscillations, as the spins are getting more homogeneously excited by the driving field. If the excitation depth is much shorter than the wavelength of the magnons, $d << \lambda_{\mathrm{sw}}$, the contribution of the driven precession fully disappears, and only the freely propagating packet remains. The small excitation depth also results in a diminished amplitude. The inset in figure 3.8a) shows a normalized zoom of the spin wave for $d = 0.1\,\mathrm{nm}$. We note that the fast and small amplitude oscillations appear as the result of artifacts in the simulations and become noticeable when the spin wave amplitude is small.

Secondly, in figure 3.8b) we observe expected behavior upon the variation of the spin wave velocity: As the velocity is increased, the spin wave propagates further from the boundary in

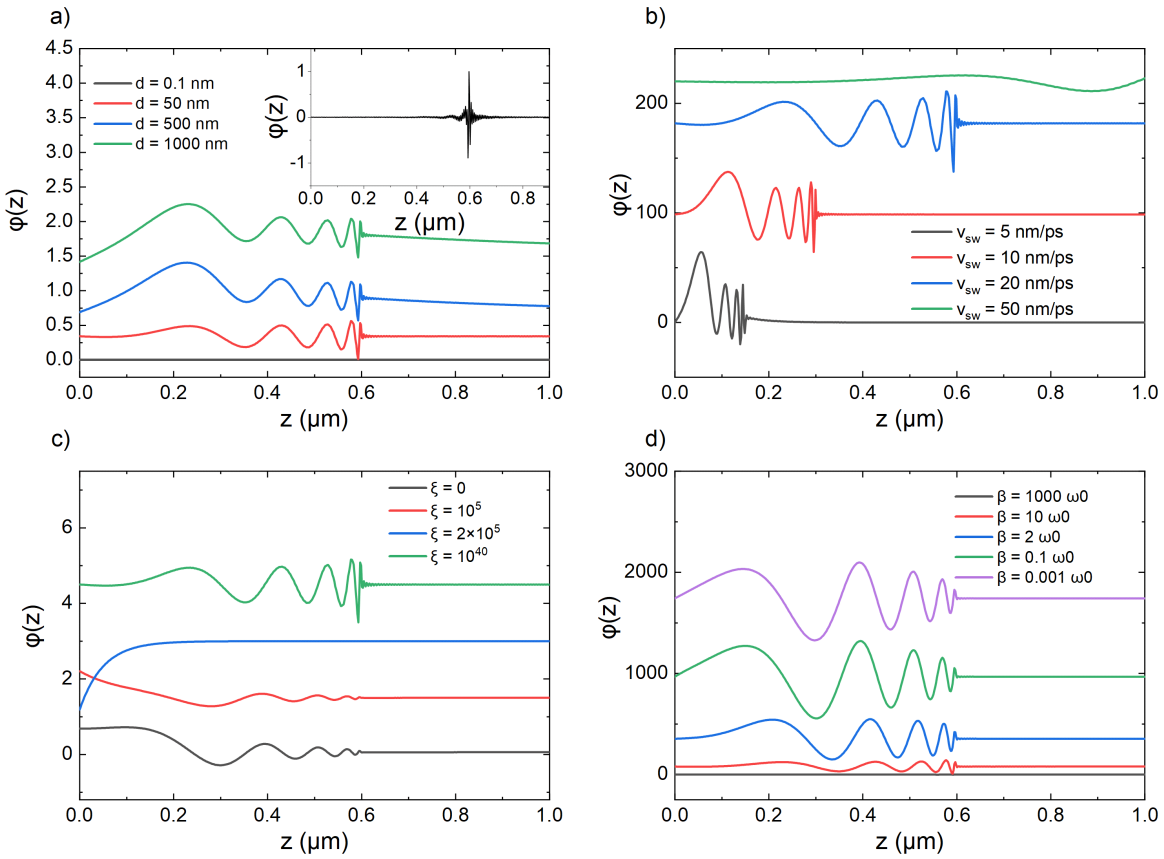

Figure 3.8: Spin wave profiles under variation of several parameters: a)Variation of the optical excitation depth d. The inset shows a zoom in for the excitation depth of $d = 0.1$ nm. b) Variation of the spin wave velocities v_{sw}. c) Variation of the pinning parameter ξ. d) Variation of the optical excitation decay parameter β for the displacive excitation. All spin waves are shown at time $t = 30$ ps.

the same time span.

Thirdly, in figure 3.8c) the effect of the pinning parameter is illustrated. We see that this parameter strongly affects the profile of the spin waves. For the free boundary conditions ($\xi = 0$), we see that the at the boundary can freely oscillate, and the spatial derivative of the spin wave at the boundary is zero. In the pinned boundary condition ($\xi \to \infty$, which we approximate as $\xi = 10^{40}$ in our numerical code, spin precession at the boundary is restricted. The pinning parameter affects the ratio between the amplitudes of the freely propagating and the driven quasi-uniform spin precession. For the special case where the pinning parameter is close to the inverse of the penetration depth of the light pulse ($\xi = 1/d$), no freely propagating wavepacket is observed. We can explain this directly with equation (3.8), from which it can be seen that for such pinning parameters, the spectral amplitude of the freely propagating component is suppressed.

Finally, we can see that the amplitude and the wavelength of the wavepacket are affected by the time during which the spins are exposed to the effective field. For long lifetimes (small values of β) we obtain short wavelengths with high amplitudes, whereas upon decreasing the lifetime of the excitation, the wavelength becomes slightly longer and the amplitude diminishes. For the very short excitation times $\beta << \omega_0$, the amplitude becomes negligible compared to the longer lifetime spin waves, and as mentioned previously, the profile of the spin becomes similar to the impulsive excitation.

3.3.7 Excitation at infinitesimal region near the boundary

We have previously seen that the width of an experimentally realistic Gaussian laser pulse can be neglected and that the spin waves are localized to the boundary of the material. As our interest is primarily on the freely propagating component of the spin wave, we conclude our investigations of the generation of these spin waves by considering the impulsive excitation in an infinitesimally thin slab at the boundary, by modelling the excitation profile as a Dirac-delta function in both space and time $h(z,t) = \delta(z)\delta(t)$. This approximation ensures that the driven solution is absent everywhere, except at $z = 0$, allowing us to focus solely on the freely propagating wave. In this model, we need to alter our boundary conditions. To this end, we assume that the spin wave is reflected at a distance δz from the boundary, such that we can write the full wave as the sum of a wave propagating to the right, and a wave propagating to the left in the region $z < \delta z$. We can then write:

$$\begin{cases} \tilde{\phi}(z,\omega) = Ae^{-ik_{\mathrm{sw}}z} + Be^{ik_{\mathrm{sw}}z} & z < \delta z \\ \tilde{\phi}(z,\omega) = Ce^{-ik_{\mathrm{sw}}z} & z > \delta z \end{cases} . \tag{3.15}$$

To find the amplitudes, we integrate equation (3.3) over an infinitesimal region around the material boundary. We find from this that $\tilde{\phi}(z,\omega)$ is continuous and its derivative $\partial\phi(z,\omega)/\partial z$ is discontinuous at the boundary. This discontinuity is determined by the amplitude of the excitation. We may then also apply the pinning boundary conditions. In the final step of the calculation, we can take the limit $\delta z \to 0$. We then find that the spin wave propagating in the material is given by

$$\phi(z,\omega) = \frac{i\omega\omega_h}{v_{\mathrm{sw}}^2(\xi - ik_{\mathrm{sw}})}e^{-ik_{\mathrm{sw}}z}. \tag{3.16}$$

These propagating spin waves are depicted in figure 3.9 for both the pinned boundary conditions and the free boundary conditions, with their spectra shown in the insets.

We see a drastic difference in the spectra, as in the pinned boundary conditions, the

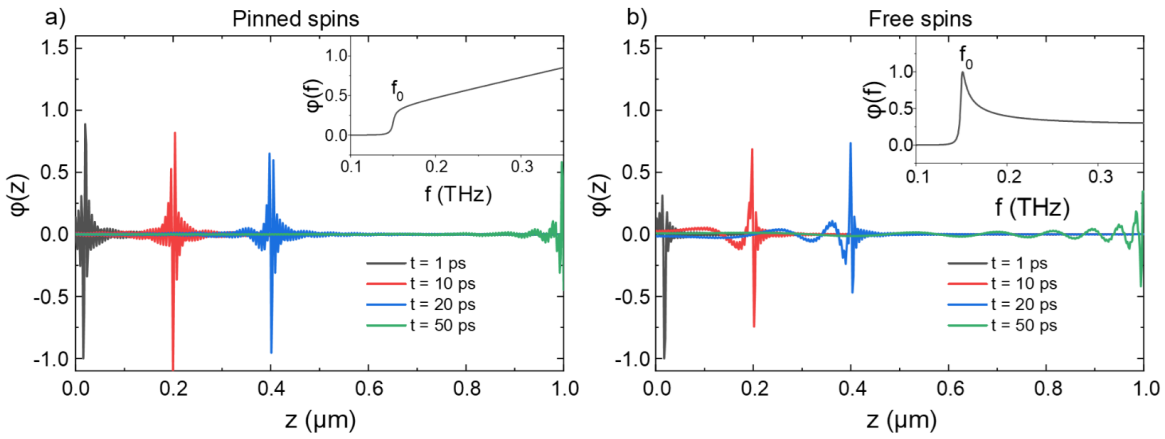

Figure 3.9: Snapshots of the propagating spin wave in a) the pinned boundary condition and b) the free boundary condition. The excitation exists solely at the boundary $z = 0$, such that $h(z,t) = \delta(z)\delta(t)$. Insets show the corresponding spectra at $z = 0.2\,\mu$m.

spectral weight increases above the resonance frequency whereas in the free spins boundary condition, the spectral weight is distributed as the more typical peak shape around f_0. As the oscillation at the boundary is allowed in the free boundary condition, the wave profile is more pronounced than for the pinned boundary condition.

We finally note that, as expected, these results show an excellent match with the simulations for the case of the exponential decay with optical penetration depths much shorter than the characteristic magnon wavelength $d << \lambda_{sw}$, as was shown in figure 3.8a).

The situation modeled here may be realized in an antiferromagnet capped by a thin ferromagnetic metal layer of a few nm coupled to the antiferromagnetic order through for example exchange bias [154]. The laser pulse can instantaneously heat the metal and destroy its magnetization, thereby exerting a torque on the antiferromagnetic spins at the interface. It is therefore possible that in previous pump-probe studies of metal-antiferromagnetic bilayers, magnetic modes with unusual frequencies could actually be attributed to the propagating spin waves launched from the boundary between the metal and antiferromagnet, instead of for example magnetic impurities [155].

3.4 Detection of antiferromagnetic spin waves

In the typical pump-probe experiments, the spin dynamics is detected with magneto-optical effects. The dynamic magnetization may for example induce a rotation of the polarization of incoming linearly polarized light. These effects can be found in both the transmissive and reflective configuration. We will refer to the polarization rotation in the transmissive configu-

ration as the Faraday rotation and to the polarization rotation in the reflective configuration as the Kerr rotation. We have shown before that the propagating spin waves decay within a region of a few μm to the boundary. Hence, we focus here on the reflective detection scheme, such that only the spin dynamics in the region close to the sample surface is probed.

In this section, we will calculate the rotation of the polarization of the probe pulse, as a result from the Magneto-Optical Kerr Effect (MOKE). This effect arises from the helicity dependent refractive index in materials with broken time reversal symmetry. For example, this time reversal symmetry can be broken by the magnetization. We start our calculation by considering a linearly polarized light pulse, that is perfectly polarized along the x-axis. The (normalized) incident electric field vector of the probe light can then be written as the superposition of a right-handed and a left-handed circularly polarized component:

$$\mathbf{e}_i = \frac{1}{2}\mathbf{e}^+ + \frac{1}{2}\mathbf{e}^- = \frac{1}{2}\begin{pmatrix}1\\-i\end{pmatrix} + \frac{1}{2}\begin{pmatrix}1\\+i\end{pmatrix} \tag{3.17}$$

As both of these components experience a different refractive index, both components are reflected differently. We denote the reflectivity of the right-handed helicity as r^+ and of the reflectivity of the left-handed helicity as r^-, such that the reflected electric field vector will be:

$$\mathbf{e}_r = \frac{1}{2}r^+\mathbf{e}^+ + \frac{1}{2}r^-\mathbf{e}^- = \frac{1}{2}\begin{pmatrix}r^+ + r^-\\ i(r^- - r^+)\end{pmatrix} \tag{3.18}$$

Assuming the polarization rotation is small, we can then see that the angle of rotation θ is given by:

$$\theta \approx \tan(\theta) = \frac{i(r^- - r^+)}{r^- + r^+} \tag{3.19}$$

We can write the reflectivity as the sum of a static and dynamic contribution, where the dynamic part is induced by the spin wave:

$$\begin{aligned} r^+ &= r_0^+ + \Delta r^+ \\ r^- &= r_0^- + \Delta r^- \end{aligned} \tag{3.20}$$

Now that the polarization rotation is expressed in terms of the reflectivity of the circularly polarized components, we need to find exactly how the dynamic magnetization affects the the reflectivity of the circularly polarized light. In a medium with magnetization along the

z-axis, the magnetization modulates the permittivity of the material, thereby affecting the refractive index of the left-handed and right-handed polarized component as follows [42]:

$$n_{\pm}^2 = \epsilon \pm g = \epsilon + \Delta\epsilon. \tag{3.21}$$

Here g is the gyration term, which is typically proportional to the magnetization ($g = aM$). Thus, we see that the permittivity of the material is modulated by the dynamic magnetization as

$$\Delta\epsilon(z,t) = \pm aM(z,t). \tag{3.22}$$

The change in reflectivity due to the modulation in the permittivity has previously been derived for the ultrafast detection of acoustic phonons, in which the reflectivity was affected by the phonon-induced strain [156], which reads:

$$r = r_0 + \frac{ik_0^2}{2k} t_0 \tilde{t}_0 \int_0^{\infty} dz' e^{2ikz'} \Delta\epsilon(z,t). \tag{3.23}$$

In this expression, r_0 is the static reflection coefficient and t_0 and $\tilde{t}_0$ are the transmission coefficients into the medium and into free space respectively, in the absence of perturbations in the permittivity. The wave-vector of the probe pulse in vacuum is given by $k_0 = \frac{2\pi}{\lambda}$ and by $k = \frac{2\pi n}{\lambda}$, with λ the probe wavelength and n the corresponding refractive index.

As our interest is on the dynamic part, we can simplify our model and consider a pure antiferromagnet, with a negligible static magnetization, such that the static components of the reflectance and transmittance are the same for both helicities. Using equation (3.22) we can then simplify equation (3.23) to

$$r^{\pm} = r_0 \pm \Delta r, \tag{3.24}$$

where

$$\Delta r = i \frac{ak_0^2}{2k} t_0 \tilde{t}_0 \int_0^{\infty} dz' e^{2ikz'} M(z',t). \tag{3.25}$$

For the magnetization in this expression, we can use the previously derived and calculated spin wave profiles, by taking the Inverse Fourier Transform of equation (3.5). Note that the solution to the Klein-Gordon equation was technically valid for the l_y component, whereas in our detection scheme, we assumed that the dynamic ferromagnetic moment was along the z-axis. Therefore, we can perform the numerical conversion of the l_y component to the m_z component as seen from the full Landau-Lifshitz equations [64].

$$\frac{\partial m_z(t)}{\partial t} = (\omega_A - \frac{v_{sw}^2}{\omega_E}\nabla^2) l_y(t) \tag{3.26}$$

We can then also relate both components in the frequency domain for both the freely propagating and driven parts of the solution:

$$\begin{aligned} f_{m_z}(\omega) &= \frac{1}{i\omega}(\omega_A + \frac{v_{sw}^2 k_{sw}^2(\omega)}{\omega_E}) f_{l_y}(\omega) \\ p_{m_z}(\omega) &= \frac{1}{i\omega}(\omega_A - \frac{v_{sw}^2/d^2}{\omega_E}) p_{l_y}(\omega). \end{aligned} \tag{3.27}$$

The Inverse Fourier Transform of the magnetization of equation (3.5) is now substituted in equations (3.25) and (3.24) and subsequently inserted in the expression for the polarization rotation angle (equation (3.19)). As the wave-vector of the spin wave is complex and was written as $k_{sw} = \kappa - i\eta$ ($\eta \neq 0$), the forward propagating spin waves decay, such that the integral over z converges, and the spectrum of the dynamics in the Fourier domain is obtained. The dynamics in the time domain is then found by applying the Inverse Fourier Transform.

$$\theta(t) = \frac{ak_0^2}{2kr_0} t_0 \tilde{t}_0 \int_{-\infty}^{\infty} d\omega e^{i\omega t} (A_f(\omega) \frac{1}{2k - k_{sw}(\omega)} + A_p(\omega) \frac{1}{2k + i/d}). \tag{3.28}$$

Here, the integral over the frequency ω represents the Inverse Fourier Transform, and $A_f(\omega)$ and $A_p(\omega)$ represent the spectral weights of the m_z components, as given by equation (3.27). One can see that in the detected spectrum, a pole emerges for magnon wave-vectors of $k_{sw}(\omega) = 2k$. For this condition, the pole $1/(2k - k_{sw}(\omega))$ would diverge, but the inclusion of damping (imaginary part of the magnon wave-number) prevents the expression from diverging. In terms of wavelengths, the spin waves with wavelengths of $2\lambda_{sw} = \lambda_{probe}$ are detected, which may be recognized as the Bragg condition. Consequently, magnons with a specific wavenumber can be selectively detected by choosing the probe wavelength, and the peak in the spectrum will arise at the frequency corresponding to this wavenumber as determined through the magnon dispersion (equation (3.2)). This condition of selective detection is referred to as the Bragg or Brillouin condition [157]. The emergence of this Brillouin condition can be interpreted by considering the propagating spin wave to effectively act as a propagating diffraction grating due to the spatial modulation of the permittivity, enhancing the reflectivity of certain wavelengths of the probe pulse [158].

3.5 Calculated magneto-optical detection spectra

In this section, we will calculate the predicted spectrum of the Kerr rotation angle by evaluation of the integrand in equation (3.28) for various wavelengths of the probe pulse. The time domain signal may then be obtained by the Inverse Fourier Transformation. As we saw before that the realistic laser excitation can well be approximated as an impulsive excitation, we again our pulse to be infinitesimally short in time. We model the detection of the spin waves for both the pinned and the free boundary condition, for the excitation depth of $d = 50\,\text{nm}$. The results are shown in figure 3.10a) for the pinned boundary condition and in figure 3.10b) for the free boundary condition.

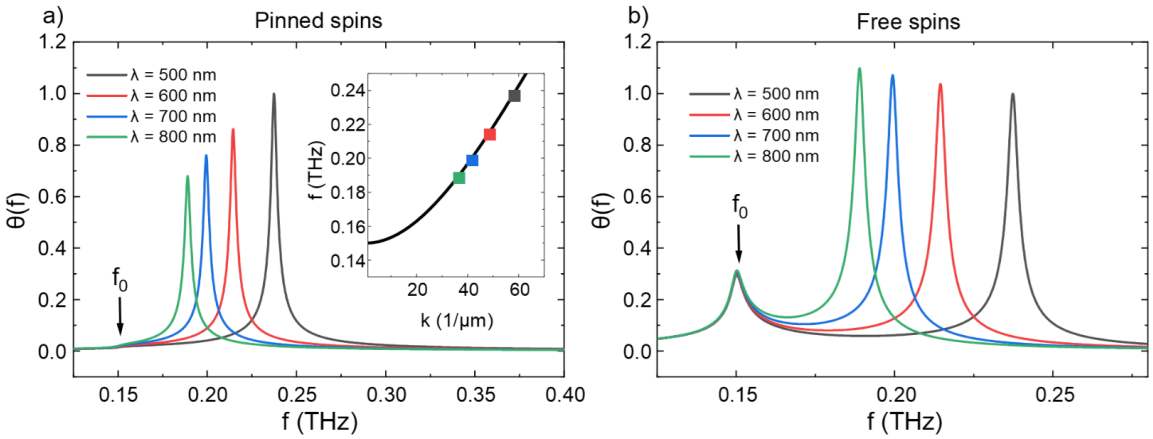

Figure 3.10: Spectra for an impulsive spin wave excitation as would be detected in a MOKE experiment. The spectra are calculated for multiple probe wavelengths λ. a) Calculated spectrum in the pinned boundary condition. In the inset, the dispersion relation is shown, with the colored points indicating the selected wave-vectors (and thus frequencies) by the various probe wavelengths. b) Spectra in the free boundary condition.

These results show that there is a noticeable difference between the spectra in the free and pinned boundary conditions. The spectral amplitude at the fundamental resonance frequency of 0.15 THz disappears completely when the spins are perfectly pinned to the surface, whereas this feature remains if the spins are allowed to precess freely at the surface. Also, we observe that if we detect the spin dynamics in a reflective configuration, the most prominent spectral feature is a peak at a blue-shifted frequency, which corresponds to the Bragg-selected wave-vector components of the broadband wave-packet f_k. As expected from the Brillouin condition, the frequency of this peak is dependent on the wavelength of the probe pulse. The wave-vector of the probe pulse selects which wave-vector of the propagating magnon wavepacket is detected. As illustrated in the inset in figure 3.10a), the peaks then appear at the frequencies that are matched to these wave-vectors as determined

by the dispersion relation. The results of this model are in excellent agreement with the experimental data reported in Ref. [70].

Additionally, we investigated the effect of the laser excitation confinement on the detected dynamics, by performing simulations for various excitation depths. The results are shown in figure 3.11a) and 3.11b) for the pinned and free boundary conditions respectively.

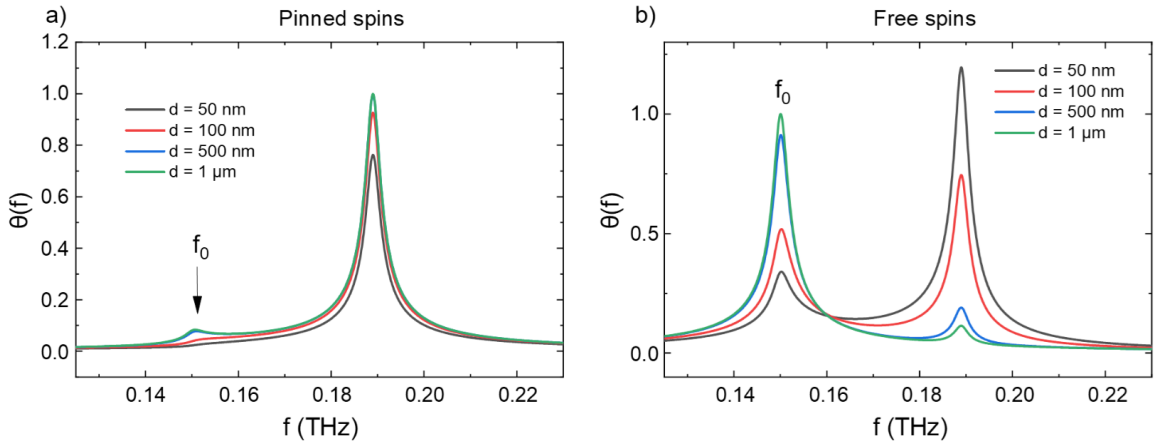

Figure 3.11: Spectra of the spin waves for various values of the excitation depth d. The probe wavelength is 800 nm. a) Spectra in the pinned boundary condition. b) Spectra in the free boundary condition.

Again, the reduced spectral amplitude at the resonance frequency can be seen in the pinned boundary condition. For long excitation depths, a very small feature at the frequency f_0 may become observable. The excitation depth only has a minor effect on the spectral amplitude of the Brillouin condition selected frequency, which may likely be attributed due to the small difference in amplitudes of the waves, that was also observed in figure 3.8a). In the free boundary condition, the effect of the confinement on the detection is much more pronounced. We see that the ratio between the peak at the fundamental $k = 0$ peak and the f_k peak is strongly affected by the excitation depth. For long excitation depths, the detected oscillations occur mainly at the frequency f_0, whereas the oscillations for short excitation depths are primarily at the higher f_k frequency. For intermediate excitation depths, that become comparable to the magnon wavelengths ($d \approx 100$ nm), we see that the amplitudes become comparable, and beatings in the signals in the time domain may be expected. This implies that with the appropriate choice of the excitation confinement, the character of the boundary condition can be experimentally determined.

Finally, we study the effect of the pinning parameter on the detection scheme. This effect

is shown in figure 3.12.

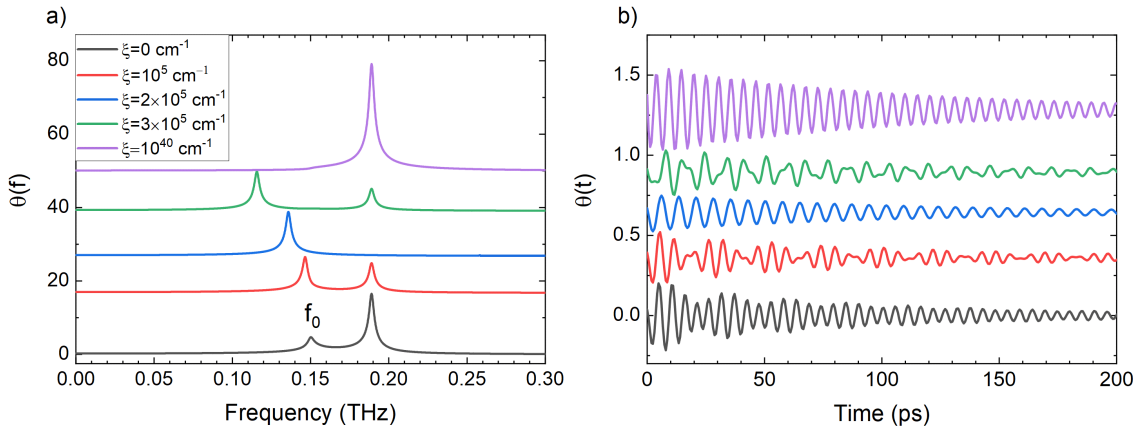

Figure 3.12: a) Calculated MOKE spectra for a variety of pinning parameters and the predicted signals in the time domain, as obtained by the Inverse Fourier Transform by the spectra in a). Simulations are performed for a probe wavelength of $\lambda = 800\,\text{nm}$ and an excitation depth of $d = 50\,\text{nm}$.

As was already discussed before, in the free boundary condition, the spectrum consists of a feature at the f_0 frequency and at the f_k frequency, whereas in the pinned boundary condition, the peak at the f_0 frequency fully disappears. As we already noticed in figure 3.8c), in the special case when the pinning parameter is equal to the inverse of the excitation depth $\xi \approx \frac{1}{d}$, the freely propagating solution is fully suppressed. As there is no freely propagating wave-packet in this case, only the peak at the $k_{\text{sw}} = 0$ is observed in the spectrum. Note that the frequency of this peak is red-shifted as a result of the damping and the confinement of the pump pulse. For intermediate pinning parameters, that are in the same order of magnitude as the inverse penetration depth, we observe further red-shifting of the $k_{\text{sw}} = 0$ mode. We understand this as the emergence of an extra pole in the spectral amplitude $A_f(\omega)$ in the detection equation (3.28). As can be seen from equation (3.8), the additional pole will occur where $\xi \approx i\,k_{\text{sw}}(\omega)$ yielding the low-frequency peak in the MOKE spectrum. Thus, this peak will appear at the frequency where the imaginary part of the magnon wave-vector is equal to the pinning parameter. As the wave-vector of the spin wave is imaginary for the angular frequencies $\omega < \omega_0$, these red-shifted peaks indeed appear at frequencies $f < f_0$. In figure 3.12b), some characteristic waveforms in the time domain are shown, as obtained by Inverse Fourier Transformation of the spectra. This illustrates how the waveforms may depend on the spectra. In the pinned boundary condition (purple curve), and for $\xi = 1/d$ (blue curve) we see a monochromatic oscillation, whereas in the free boundary condition (black curve) a small beating pattern becomes visible. For the pinning parameters close to, but not equal to $1/d$ (red and green curves), the amplitudes of the two modes become comparable, and

characteristic beating patterns can be observed in the time domain.

3.6 Conclusions

In this chapter, we have discussed a model for the optical generation of propagating packets of spin waves and their detection. We considered multiple cases of excitation, among which we approximated the effective field to act as an impulsive and displacive excitation, but we also considered experimentally realistic cases, namely excitations by a Gaussian laser pulse and a (nearly) single-cycle THz pulse. We found that for experimentally realistic parameters, the laser excitation can be appropriately approximated to act as an infinitesimally short excitation. When the pulse frequency or duration become comparable with the precession frequencies (as the case for the THz excitation), slight modifications in the spin waves can be observed. We found that these optical excitations launch packets of spin waves that travel much slower than the light pulses, and decay in a region of a few μm near the boundary. Therefore, propagation effects may be neglected.

Furthermore, a formalism for the magneto-optical detection of the magnons was derived, by calculating the magneto-optical Kerr rotation in reflective geometry, which demonstrated that the components of the wavepacket are selectively detected through a Brillouin condition. As a consequence, the detected frequency of the spin wave blue-shifts with increasing probe light frequency. The observations in our model can be confirmed experimentally by varying the probe pulse or angle of incidence. The results of the model are in excellent agreement with the recently performed experiment of optical generation and detection of propagating magnons in an antiferromagnet [70]. Furthermore, we have identified differences in the detection of the spin waves in the pinned boundary conditions. This implies the theoretical possibility to distinguish these boundary conditions experimentally. As the boundary conditions are strongly determined by the non-uniformity of the exchange field and the surface anisotropy of the material, experimental observation of these boundary conditions could provide further insight in the material properties [148].

As a final note, we remark that this develop formalism is applicable very generally. Although we considered the orthoferrites as an example system, the equations used in this model should be valid for any antiferromagnetic system. In principle this model is able to describe the spin dynamics for any form of the excitation, and may therefore be used in future experiments on antiferromagnetic magnonics.

Chapter 4

Experimental observation of propagating packets of spin waves in $HoFeO_3$

4.1 Introduction

This chapter will discuss the pump-probe experiment used to excite and detect propagating packets of spin waves that was theoretically described in Chapter 3. Here, we will be restricting ourselves to the regime of linear spin excitations, as was approximated in the previously described model. More specifically, we will be considering the rare-earth orthoferrite $HoFeO_3$. We find that we can map out a broad band of frequencies and wavenumbers, thereby demonstrating the realization of packets of spin waves propagating at high velocities close to their limit. Furthermore, we explore in more detail the excitation mechanism and find that despite relying on absorptive features to confine the light excitation, the spin wave excitations occur through non-thermal, coherent effects. Here, only the basic experiments involving a single pump beam will be discussed, which will act as preliminary data for the following chapter, in which we extend on this concept by introducing second pump pulse.

4.2 Experimental Setup

A more detailed description of the general concepts of the pump probe setup was given in Chapter 2, but a short summary will be given here.

The schematic of the setup used to launch and detect the propagating spin waves in $HoFeO_3$ is illustrated in figure 4.1.

In our experiment, we used a 800 nm amplified Ti:Sapphire laser system with pulse duration of 100 fs and a repetition rate of 1kHz. The majority of this laser beam was sent to an

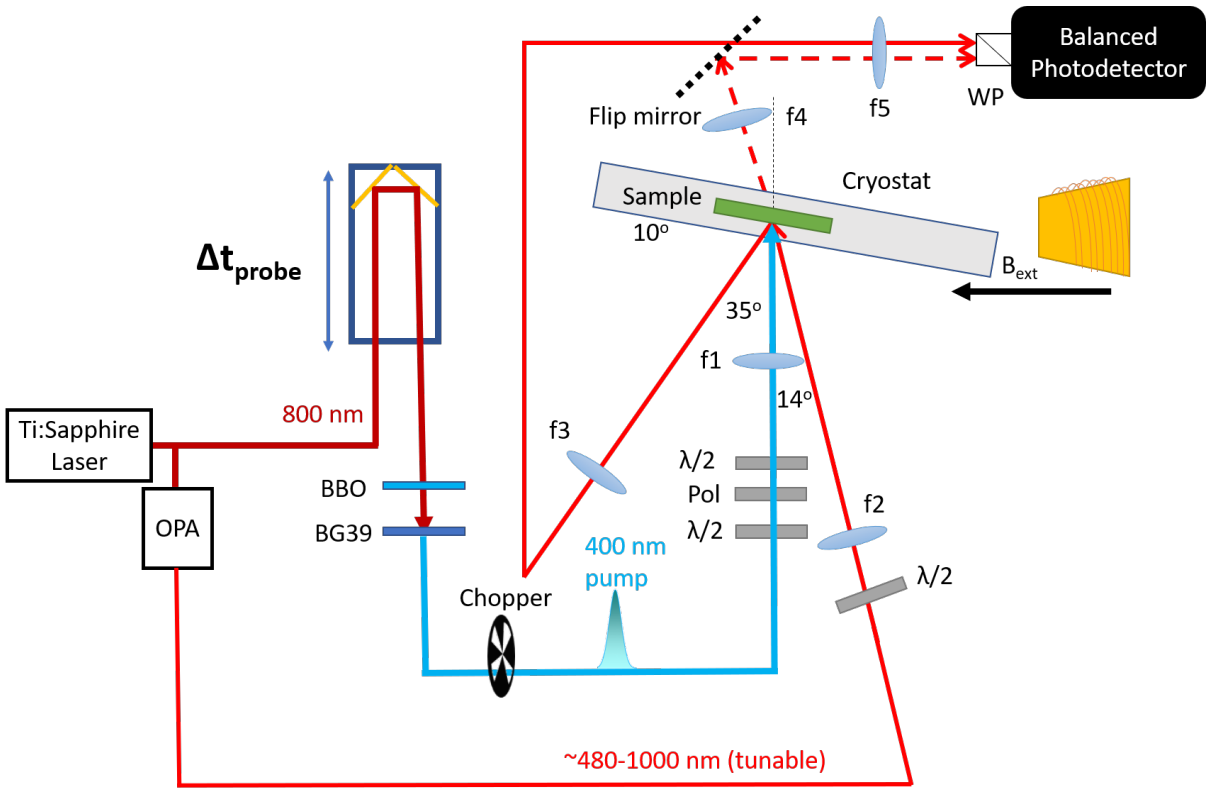

Figure 4.1: Illustration of the experimental setup to demonstrate the spin waves in $HoFeO_3$. The lenses in the setup are indicated by f_1 to f_5. Pol and $\lambda/2$ denote the polarizer and the half wave plates respectively. WP represents the Wollaston Prism, and BBO is the nonlinear crystal converting the 800 nm pulse to a 400 nm pump pulse through SHG. The remaining 800 nm is removed by a BG39 bandpass filter. The pump pulse passes through a delay line creating time delay Δt_{probe} between pump and the probe with tunable wavelength generated in the OPA. An electromagnet applies a magnetic field B_3 in the plane of the sample (see also main text).

Optical Parameteric Amplifier (OPA), that converts the near-infrared photons into UV-visible photons, with tunable wavelength. We used this tunable output of the OPA as the probe pulse. The remainder of the 800 nm was split off and converted through Second Harmonic Generation (SHG) into the 400 nm pump pulse by focusing this light on a beta Barium Borate (BBO) crystal. The remainder of the 800 nm was filtered out with a BG39 Schott filter. A set of filters attenuated the power of the 800 nm beam incident on the BBO crystal and the pair of half wave plate ($\lambda/2$) and polarizer was used to further control the pulse energy of the pump beam. A second $\lambda/2$ plate was used to control the polarization of the pump beam incident on the sample. The pump beam was focused on the sample by a lens that was placed slightly away from the focal distance, to irradiate a large spot of the sample of approximately 1 mm, as confirmed by a knife-edge measurement. The probe beam was attenuated with filters and focused to a tighter spot, and spatially overlapped with the pump beam. Also the probe polarization was controlled with a $\lambda/2$ plate. The sample was placed in a open cycle cryostat, and was cooled down with liquid Helium to temperatures down to 5 K. A small magnetic field of B_{ext}=25 Gauss was applied to saturate magnetic domains. The transmitted probe light and the reflection from the sample were collimated with lenses and guided to a balanced photo-detector. A flipper-mirror allowed us to quickly change between the transmissive and reflective configuration. A built-in Wollaston prism separated the orthogonally polarized components of the probe beam. The signals could be balanced by rotation of the balanced photo-detector, and the rotation of the polarization due the dynamic magnetization was obtained with the pump-induced change of the signals on the photo-detectors. The signals on the detector were analyzed with a lock-in amplifier, with the input reference frequency synchronized with the frequency of the optical chopper (500 Hz), to enhance the sensitivity to only the pump-induced signals.

4.3 Properties of $HoFeO_3$

The weak ferromagnet $HoFeO_3$ is a quite unique material in its class, due to its relatively complex phase structure. It exhibits antiferromagnetic ordering of the spins below the Neel temperature of $T_N \approx 650$ K. In the low temperature phase $T < T_1 \approx 38$ K, the spins are in the Γ_2 phase. At $T_1 < T < T_2 \approx 52$ K the spins are in the Γ_{12} phase, where the antiferromagnetic moment gradually rotates in the bc-plane. As the temperature reaches T_2, the antiferromagnetic moment instantaneously jumps to the ac-plane and enters the Γ_{24} phase. At high temperatures $T > T_3 \approx 58$ K the spins are in the Γ_4 phase, and the weak ferromagnetic moment is aligned along the crystallographic a-axis [159]. In our experiment, we use a c-cut

$HoFeO_3$ sample, and we oriented the sample such that the a-axis was horizontal and aligned with the external magnetic field. The sample thickness is 60 µm. Moreover, $HoFeO_3$ is an insulator with a large bandgap of approximately 3 eV [160], which is a characteristic for most orthoferrites [161]. Thus, illumination of the $HoFeO_3$ sample with 400 nm (3.1 eV) photons can result in interband excitations, resulting in strong absorption bands for these photon energies.

4.4 Temperature dependence of the spin dynamics

The frequencies of the spin dynamics in the orthoferrites are typically strongly dependent on temperature. To observe the propagating packets of spin waves, it is necessary to know exactly the frequency of the quasi-uniform precession f_0. We therefore measured the spin dynamics at a variety of temperatures, in both the transmissive and the reflective configuration. The transmissive configuration allows us to obtain the frequency f_0, whereas the reflective configuration allows us to pick up the higher frequency components corresponding to the non-zero magnon wavenumbers $k_m(\omega)$ through the Brillouin condition. The Brillouin condition was derived in Chapter 3, and is given by equation (4.1) for oblique incidence of the probe pulse.

$$k_m(\omega) = \frac{2\pi n \cos(\gamma)}{\lambda_{pr}} \tag{4.1}$$

The wavelength, refractive index and the angle of incidence of the probe pulse are represented by λ_{pr}, n and γ respectively. The results of this experiment are shown in figure 4.2.

The time domain signals are typically associated with a step, due to a light-induced phase transition. [159] Our focus is only on the oscillations, and therefore we subtract the background after the temporal overlap by fitting the data with a polynomial function and considering the residuals of this fit. In figure 4.2a) the dynamics detected in reflection and transmission are compared at the temperature T=37 K. The confinement of the laser pulse and the spin precession in a micrometer scale region close to the sample surface makes it challenging to detect dynamics in the transmissive configuration. Therefore, we interchanged the pump and probe and launched the spin dynamics with the 480 nm output from the OPA and probed with the 800 nm light. In the reflective configuration, we used the 660 nm output from the OPA for the probe and the 400 nm for the pump. The signals were Fourier transformed and the spectra are shown in figure 4.2b). A clear shift in oscillation frequencies can be observed, as a result of the selective detection with the Brillouin condition of the $k \neq 0$ components of the wavepacket. Figure 4.2c) shows the extracted frequencies in transmission (black spheres)

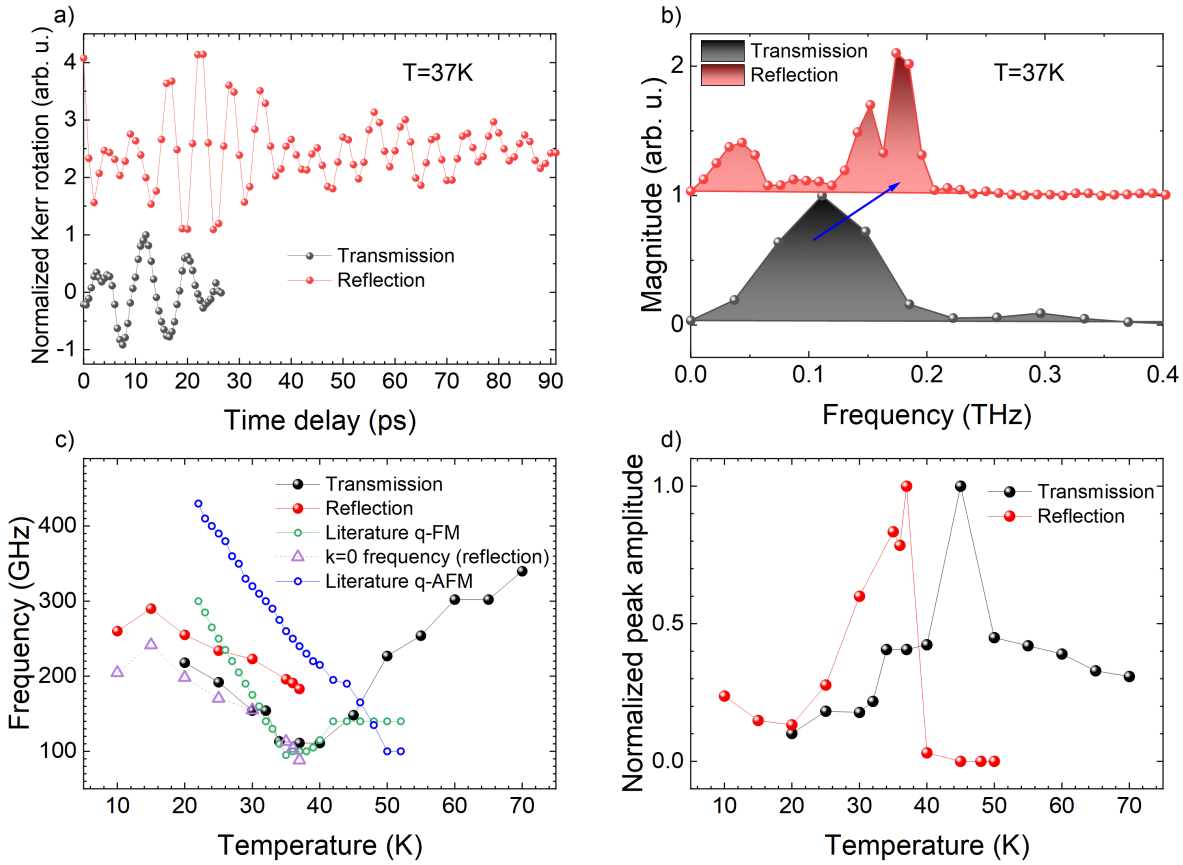

Figure 4.2: Temperature dependence of the spin dynamics in $HoFeO_3$ in both the transmissive (black) and reflective (red) experimental geometries. a) Example of the oscillations in the transmissive and reflective configuration at temperature T=37 K. b) Spectra of the oscillations in a). c) Dependence of the extracted frequencies on the temperature. d) Dependence of the extracted amplitudes on the temperature. The amplitudes are normalized.

and reflection (red spheres)as a function of temperature. The detected frequencies in the reflective geometry f_k were converted to the $k = 0$ frequencies using the Brillouin condition and the dispersion relation (purple triangles). The expected $k = 0$ frequencies from the data measured in reflection match closely with the $k = 0$ frequencies found in the transmissive geometry. We also compared the data with the literature values of the q-FM (green circles) and q-AFM (blue circles) modes [55] and found that the data matches most closely with the q-FM mode. The resemblance is closest in the range of 30-45 K and deviates for the lower temperatures, likely due to inaccuracies of the temperature control in the cryostat at the low temperatures. Finally, the amplitudes of the oscillations are plotted in figure 4.2d). We see that the amplitudes of the measured oscillations increases with increasing temperature, up to 37 K, and then rapidly drops. On the other hand, the transmission signal increases around this temperature. One could argue that this is demonstration of the spin reorientation transition, as the weak ferromagnetic moment rotates out of plane with increasing temperature. When measuring the MOKE, the probe is expected to be more sensitive to the in plane component, whereas when measuring the Faraday effect in transmission the probe becomes more sensitive to the out of plane component.

4.5 Probe wavelength dependence

The key experiment to demonstrate the propagating packet of spin waves is the measurement of the spin dynamics for a variety of probe wavelengths. Figure 4.3 shows the results of this experiment.

Figure 4.3a) shows an example scan measured at 37 K with the corresponding spectrum shown in figure 4.3b). This spectrum displays the emergence of two peaks, where the low frequency peak at 80 GHz the peaks at 190 GHz corresponds to the $k = 0$ uniform precession mode, and the high frequency peak corresponds to the $k \neq 0$ component of the wavepacket. Similar scans were measured for probe wavelengths ranging from 480 nm to 1000 nm, and the frequency f_k was tracked. The Brillouin condition (4.1) allows the conversion of the probe wavelength to the detected wavenumber. We found that a broadband range of almost 100 GHz could be mapped out, indicating the presence of high wave number components in the magnon wavepacket. The detected frequencies are well fitted with the magnon dispersion relation (3.2) (blue solid line). The fitted dispersion relation shows that the magnons can propagate with supersonic velocities of up to 22 nm/ps. We note that we achieved the high wavenumber regime, where the dispersion relation becomes quasi-linear. The magnons in this range are therefore expected to exhibit relativistic behaviors, similar to photons.

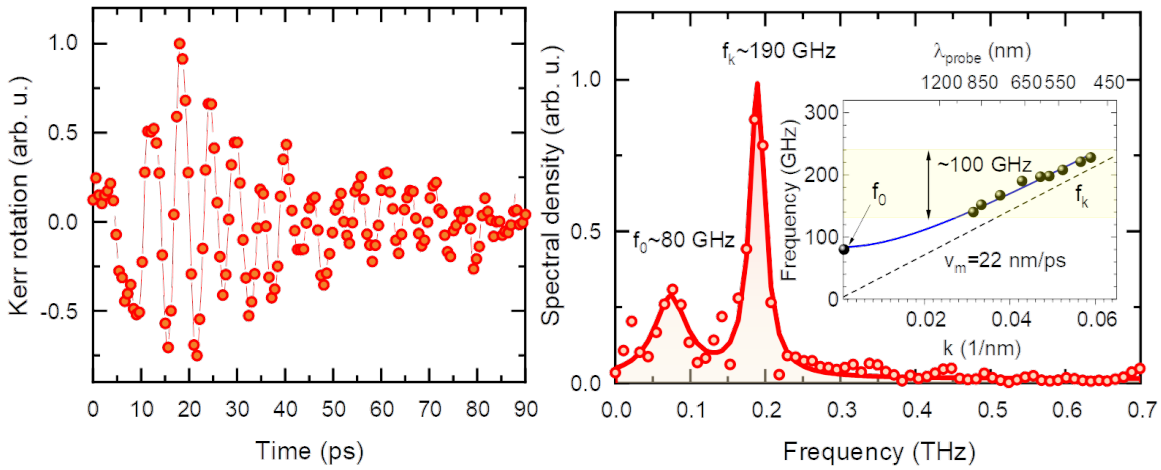

Figure 4.3: Single pump-probe MOKE signal for a probe wavelength of 660 nm. The signal is normalized and the non-oscillatory background signal is subtracted. b) Fourier transform of the data in panel a). The spectrum is fitted with the sum of two Lorentzian functions. Inset b): the retrieved magnon dispersion, which is fitted with the solid blue line based on the dispersion relation.

4.6 Pump polarization dependence

To investigate the mechanism through which the spin waves were excited, we excited the spin waves with the linear pump polarization at various angles with respect to the crystallographic b-axis. Example scans are shown in figure 4.4a) and the extracted amplitudes are shown in figure 4.4b).

The apparent dependence of the amplitudes on the linear polarization angle demonstrates that the spin dynamics is excited through a non-thermal effect. The amplitudes of the spin dynamics is maximal for diagonal polarization, which matches most closely with the Inverse Cotton Mouton Effect (ICME). [40] For this particular effect, the effective field is given by

$$H_{\text{eff}} \propto E_x E_y \,, \tag{4.2}$$

which is maximized for diagonal pump polarization.

4.7 Fluence dependence

Finally, we investigated whether the excitation of the magnons exhibits any nonlinearity by measuring the effect of the pump fluence on the amplitudes. The results of these measurements are shown in figure 4.5.

We see that the spin wave amplitude already saturates at relatively low fluences of

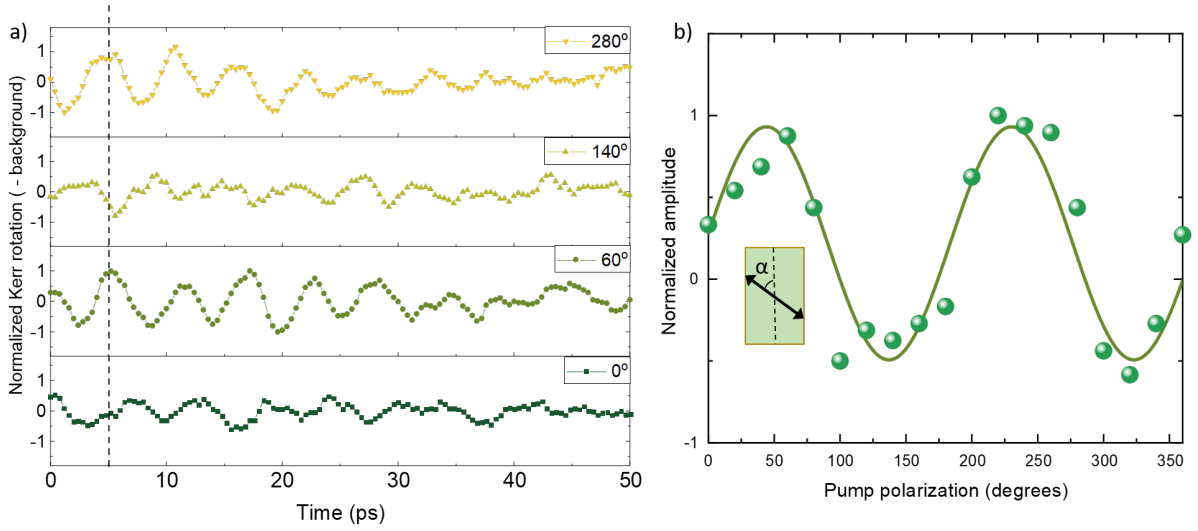

Figure 4.4: Pump polarization dependence of the measured spin wave signals. Example scans are shown in panel a) and the amplitude at the dashed line in tracked in panel b).

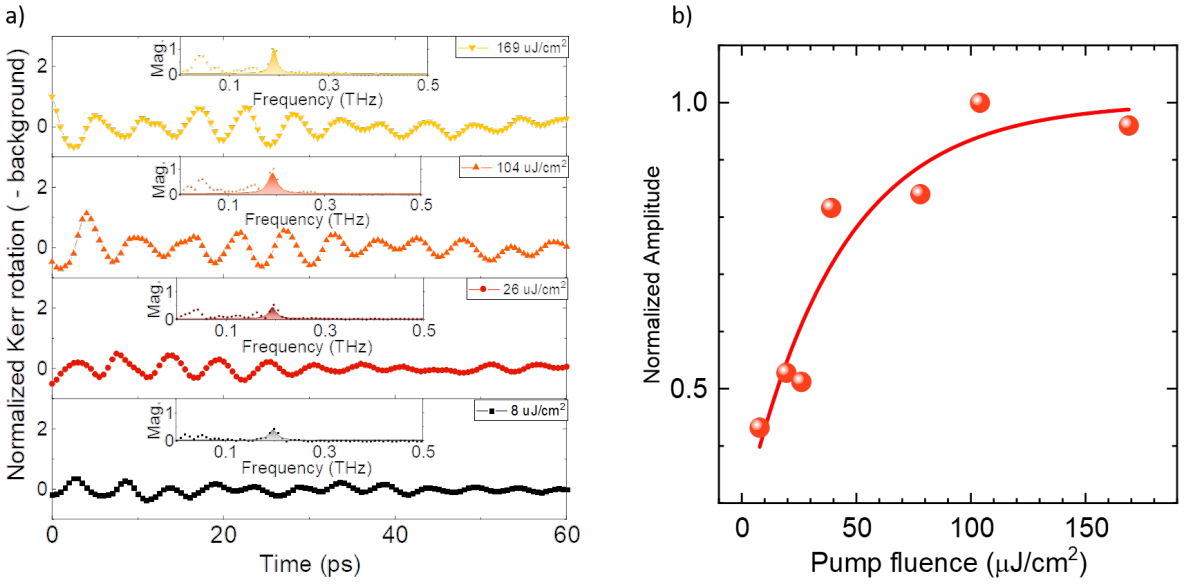

Figure 4.5: a) Spin wave signals measured for a variety of pump fluences. b) Magnitude of the peak in the spectrum as a function of pump fluence. The solid line shows a guide to the eye.

$100\,\mu J/cm^2$. The solid line shows a guide to the eye through the data, that was obtained by fitting with an exponential saturation function. This saturation implies a high efficiency of the spin wave excitation, from a non-thermal effect, as was discussed in the previous section. As a result, the magnon propagation may be intrinsically nonlinear. In the following section, we further examine nonlinearities by performing a double pump-probe spectroscopy experiment.

4.8 Conclusion

In this chapter, we discussed some preliminary experiments on the experimental generation and detection of propagating magnons in the canted antiferromagnet $HoFeO_3$. We found that the the spin waves are generated through non-thermal magneto-optical effects with confined laser pulses and detected the spin waves in a time resolved MOKE experiment, through the Brillouin condition theoretically considered in Chapter 3. By varying our probe wavelength, we could map out a broadband of components of the wavepacket, and detected frequencies of up to more than 200 % of the antiferromagnetic resonance frequency, and found supersonic spin wave propagation with velocities approaching 22 km/s. Moreover, in contrast to the previously reported experiment in Ref. [70] we observed both modes corresponding to the k=0 and k≠0 precession. From this observation the question arises how these two modes interact. In the following chapter, we will expand on the experiment performed here, and demonstrate a way to convert these modes into each other by using a second pump pulse.

Chapter 5

Ultrafast nonlinear optical Conversion of propagating magnons in $HoFeO_3$

In this chapter, we will discuss a nonlinear interaction of the $k = 0$ magnon and the $k \neq 0$ magnon, mediated through photons. We realize this experimentally by introducing a second pump pulse, using the double pump-probe spectroscopy technique. The first pump will launch the spin dynamics as discussed in the previous chapter. We will demonstrate that the second pump introduces a nonlinear interaction that exerts an additional torque on the spins that allows for the up-conversion of the quasi-uniform precession mode to higher frequency modes of the propagating wavepackets.

5.1 Introduction

One of the fundamental questions in antiferromagnetic magnonics is how to demonstrate nonlinearities in the magnon-magnon interaction, for example in the demonstration of magnon transistors or logic gates. Despite the fact that progress towards the realization of such devices has been made over the last years [86, 139], the studies on magnonics have so far been limited to the studies on either ferromagnetic materials, possessing relatively low GHz resonance frequencies and/or relatively long wavelengths of the spin waves. On the other hand, the antiferromagnets with high resonance frequencies have until recently shown the lack of propagation of the magnons [70], restricting the magnons to the center of the Brillouin zone. As a result, the potential of antiferromagnetic materials for magnon-based devices has not yet been extensively investigated. In particular, for such devices nonlinear interactions are required. Here, we will demonstrate a method of nonlinear control of magnons by using the double pump-probe spectroscopy technique, extending on the experiments discussed

in Chapter 4. As illustrated in figure 5.1, we will see that this double excitation technique allows for the conversion between the magnon modes. The first pumps launches a spin wave that propagates normal the sample boundary into the material with high frequencies f_k, as theoretically discussed in Chapter 3 and experimentally shown in Chapter 4. Simultaneously, this pump drives a static $k = 0$ quasi-uniform precession mode at frequency f_0 The second pump pulse introduces a nonlinear interaction that allows for the up-conversion of this quasi-uniform precession mode into a new wavepacket of propagating spin waves with higher frequencies f_k.

5.2 Experimental setup

The operational principle of the setup is largely similar to the setup described in Chapter 4, with a few modifications. The experimental scheme is shown in figure 5.2.

In this experiment, we introduced a second pump pulse by splitting the beam with a beam splitter that reflects 50% and transmits 50% of the pulse intensity. The beam was sent in an Michelson-Interferometer, using two back-reflecting mirrors that were placed on translation stages. We kept one of the stages in a fixed position, whereas the other stage could be moved to control the time delay $\tau = t_1 - t_2$ between the two pumps [162]. In figure 5.2, the fixed stage is referred to as the 'x-stage' and the stage that was moved to control the time delay is referred to as the 'y-stage'. An optical chopper was placed in the setup. As discussed in Chapter 2, the optical chopper is used to modulate the pump at a frequency of 500 Hz, which is synchronized to the lock-in amplifier. As a result, only the signals that are induced by the pump pulse will be detected, and all signals and noise occurring at different modulation frequencies are filtered out. In our experiment, we placed this optical chopper at two different positions. Firstly, the optical chopper was placed after the interferometer arm. As a result, both of the pumps coming from the x-stage and y-stage are modulated with the lock-in frequency, and we could expect to see the coherent interaction between the two excited spin waves in the form of interference. Additionally, nonlinear interactions in the signal can be isolated by placing the chopper in the static interferometer arm. In this configuration, the signals induced by the pump coming from the time delayed y-stage are invisible, and only the nonlinear effect on the signals induced by the pump from the x-stage are observable. In this configuration we performed two-dimensional spectroscopy experiments. We measured the spin waves similarly to described in Chapter 4 for various time delays between the two pumps.

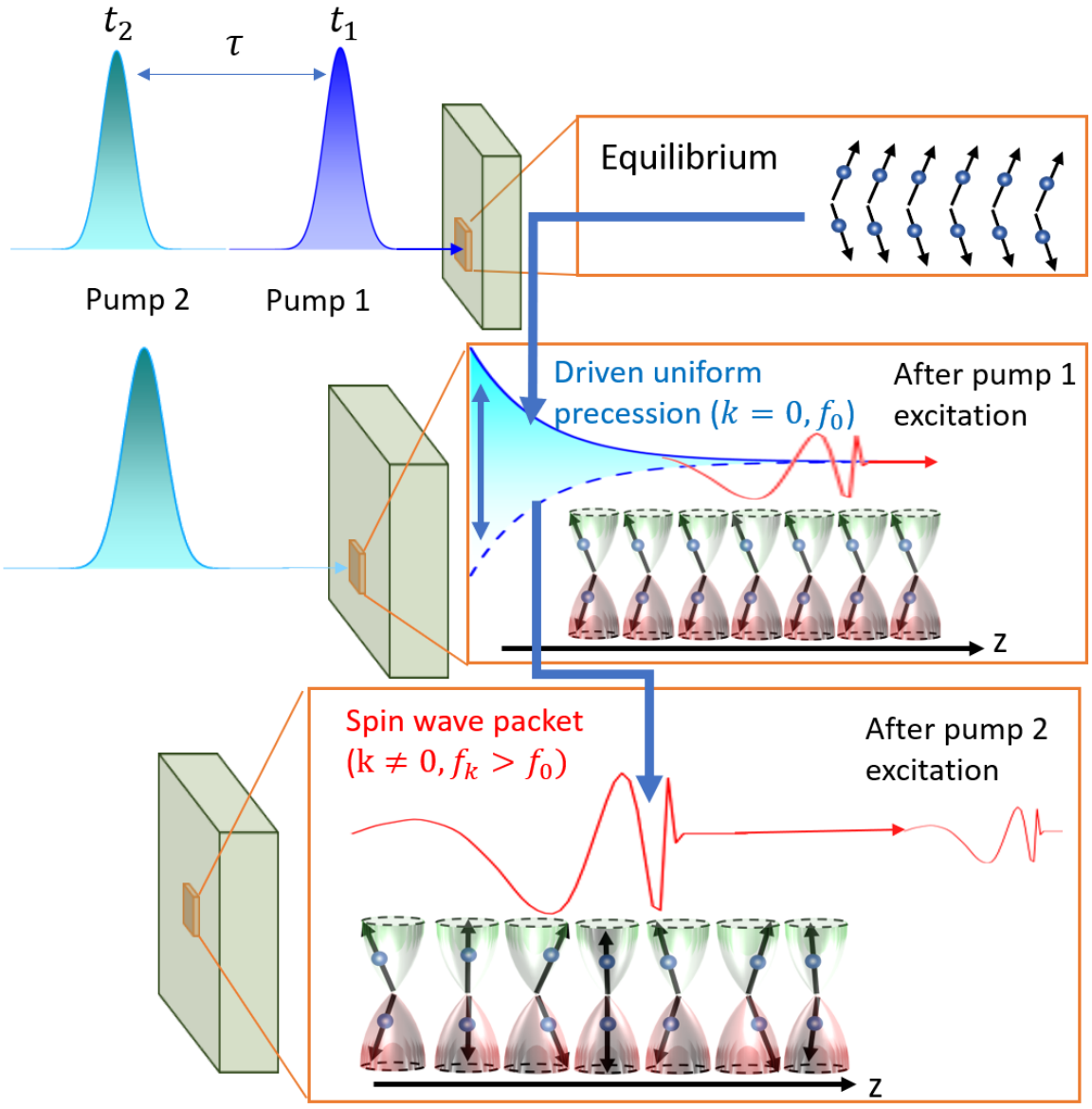

Figure 5.1: Schematic of the up-conversion of the quasi-uniform precession to the propagating magnon modes. Top panel: before the arrival of the first pump, the spin system is in equilibrium. Middle panel: The first pump, arriving at $t = t_1$ excites spin dynamics, consisting of the quasi-uniform precession with intrinsic resonance frequency f_0, (blue) and a propagating magnon wave-packet with higher frequencies (red). Bottom panel: At the time of arrival of the second pump $t_2 = t_1 + \tau$, the wave-packet excited by pump 1 has propagated away, and the remaining quasi-uniform precession is converted in an amplified spin wave.

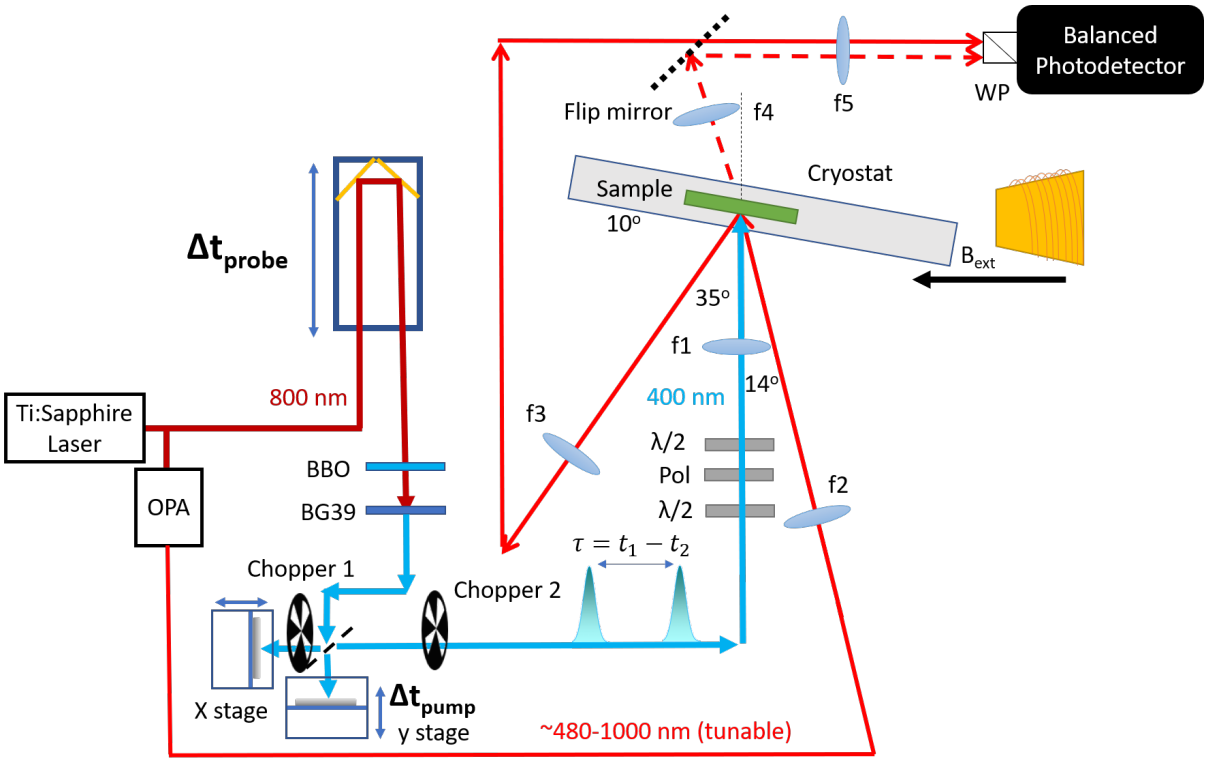

Figure 5.2: Schematic of the double-pump probe setup used to demonstrate the nonlinear conversion of magnon modes. The lenses are indicated with f_1 to f_5, and the half wave plates, polarizer and Wollaston Prism are indicated by $\lambda/2$, Pol, and WP respectively. Note the similarities with the setup depicted in figure 4.1. The second pump is introduced by separating the input pump beam in an interferometer, containing of two moveable mirrors on the x-stage and y-stage. A time delay $\tau = t_1 - t_2$ is created by moving the mirror on the y-stage.

5.3 Experimental results

To extract the nonlinearity from the time domain signals, we need to perform Fourier Transformations of the experimental data, to illustrate how the amplitudes and frequencies of the signals are modulated. As the nonlinear response in our experiment is induced by the second pump pulse, only the signals after the arrival of the second pump pulse will be considered. As was mentioned in Chapter 4, the signals are also associated with a step due to the light-induced phase transitions. Therefore, we fit the signals with a polynomial after the arrival of the second pump to remove zero-frequency components, and neglect the signals before this pump arrives. Note that the output of the OPA that is used as the probe is not passing through any delay lines, and therefore has a fixed arrival time. On the other hand, the time delay between the pump from the static x-stage and probe (Δt_{probe})is introduced by the delay line, and the time delay between the x-stage pump and y-stage pump is created by moving the back-reflecting mirror on the y-stage. As the two delay lines are in the same path, the delay between the two pumps $\tau = t_1 - t_2$ will also affect the temporal overlap of the pump from the y-stage with the probe pulse.

We started our 2-dimensional pump-probe spectroscopy experiment by investigating the coherent control, or interference, of the spin waves. To this end, the optical chopper was placed after the beams passed through the interferometer, such that both of the pumps are modulated. The probe wavelength used in these measurements was 660 nm, and the data was measured at the temperature of T=44 K. This temperature corresponds to the temperature close to the spin reorientation phase transition. The data measured in this configuration are shown in figure 5.3. Note that as compared to the temperature dependence data presented in Chapter 4, there is a shift in temperature, which we attribute to the fact that these measurements were performed at a later time and in different experimental configuration. The losses in power in the Michelson-interferometer stage may reduce the heating on the sample, resulting in a temperature shift in the data as compared to the single pump experiment.

The data presented in figure 5.3a) shows the measured MOKE signals for various delays between the two pumps. The signals in this figure are normalized with respect to the signal that was obtained for synchronous arrival times of the two pump pulses. Figure 5.3 shows the corresponding Fourier transforms. These results show a clear modulation of the amplitude of the spin waves. At first glance, one may argue that the observed amplification and suppression of the spin waves is simply a result of the linear superposition of the two pump-induced signals. However, upon closer inspection, we see that the oscillations can also invert their sign, which cannot be explained solely by interference. We further investigated this modulation

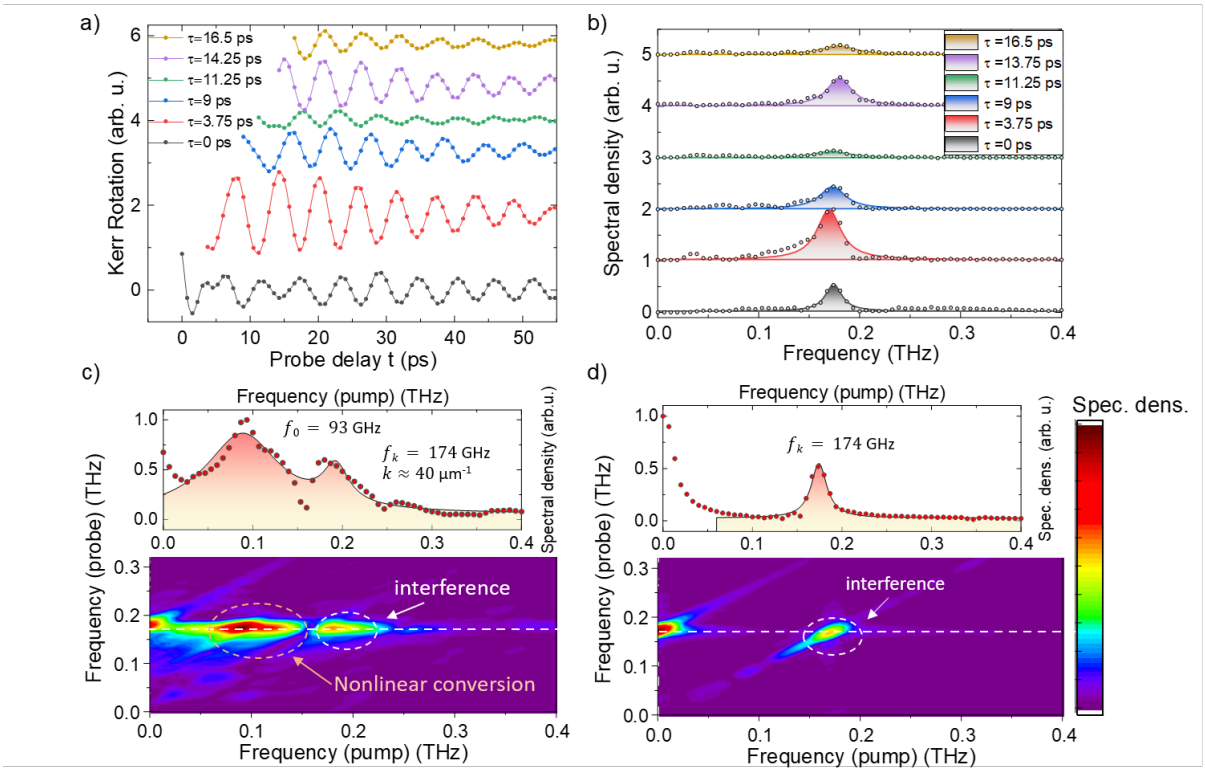

Figure 5.3: a) Normalized probe polarization rotation traces, for various delays between the 2 pump pulses. Both of the pumps are modulated, and the data are shown after the arrival of the second pump pulse. The non-oscillatory background signal is subtracted. b) Fourier transforms of the traces in a). c) 2D Fourier transform of the data measured in a), with the Fourier transform along the probe delay t on the vertical axis and the Fourier transform along the pump delay τ on the horizontal axis. The upper part shows the spectrum along the pump frequency at the magnon frequency detected by the probe. d) Reference 2D Fourier transform obtained by adding two single pump reference scans.

frequency by performing a 2-dimensional Fourier Transformation. Figure 5.3c) shows the obtained 2D-spectrum, with the Fourier transform along the probe delay on the vertical axis and the Fourier transform along the pump delay along the horizontal axis. Indeed, we see the presence of a diagonal peak in this spectrum, at the frequencies (f_k, f_k) which can exactly be explained by interference of the $k \neq 0$ magnon modes. In principle, a nonlinear interaction may also be featured in this diagonal peak, however it is impossible to confirm this in this experimental configuration. In addition, an off-diagonal peak is detected in the 2D-spectrum. The frequencies at which this feature occurs corresponds to the (f_0, f_k) frequencies. Thus, we see that the frequency at which the spin wave amplitude $k \neq 0$ is modulated beyond interference and the modulation occurs through a nonlinear interaction between the $k = 0$ uniform precession mode and the $k \neq 0$ magnon mode. This implies that the quasi-uniform precession mode f_0 is converted into the higher frequency modes of the propagating wavepacket f_k. We checked carefully whether this off-diagonal feature is the result of artifacts in our analysis procedure, by creating a reference map that is created by adding two single pump signals obtained from the x-stage and the y-stage. This generated reference map only shows the diagonal feature, as would be expected from the linear response resulting from the interference of the two pump-induced signals. Thus, we confirmed that the modulation of amplitude is indeed caused by a nonlinear interaction. Besides, we notice that the spectral weight of the off-diagonal peak is stronger than the peak corresponding to the interference, thus indicating the strongly nonlinear regime of magnon propagation.

To further confirm that the observed features are a result of nonlinear magnon interactions, we repeated the experiment by placing the optical chopper in the static interferometer arm, such that only the linear signal emanating from the static pump pulse and the nonlinear signal introduced by the second pump pulse will be observable. The results of this experiment are depicted in figure 5.4.

Similarly to our observation in the previously described experimental configuration, figure 5.4a) and figure 5.4b) shows the amplification and suppression of the spin waves depending on the time delay between the two pump pulses. In this experiment, this modulation cannot be explained by the linear superposition of the spin waves as must thus be a result of a nonlinear interaction. We performed a similar 2D frequency analysis, and observed the features at the exact same frequencies. Interestingly, now the emergence of the diagonal (f_k, f_k) peak cannot be ascribed to the coherent superposition of the spin wave signals. Thus, this feature may be also be attributed to the similar interaction allowing for the amplification and suppression of the propagating magnon modes.

Finally, we checked that the modulation of the amplitudes is not a result from amplitude

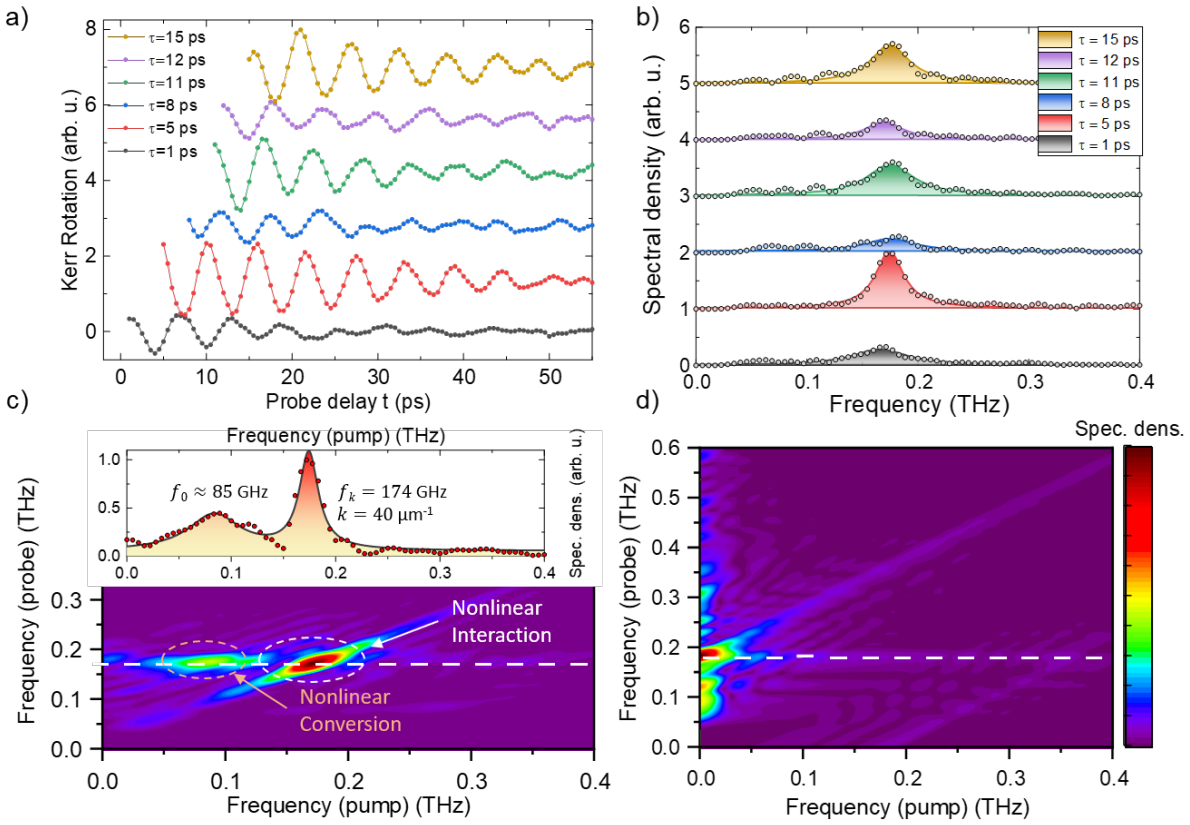

Figure 5.4: a) Normalized probe polarization rotation traces, for various delays between the 2 pump pulses. Only one of the pumps is modulated and the data are shown after the arrival of the second pump pulse. The non-oscillatory background signal is subtracted. b) Fourier transforms of the traces in a). c) 2D Fourier transform of the data measured in a), with the Fourier transform along the probe delay on the y-axis and the Fourier transform along the pump delay on the x-axis. The upper part shows the spectrum along the pump frequency at the magnon frequency detected by the probe. d) Reference 2D Fourier transform obtained by adding two single pump reference scans.

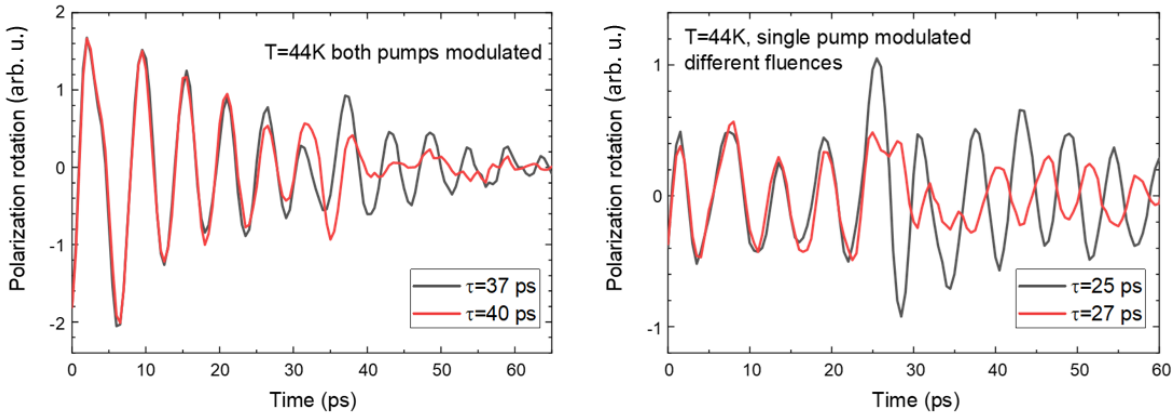

Figure 5.5: Comparison of the amplitudes of the spin waves before and after arrival of the second pump pulse. The left panel shows example data for the case when both pumps are modulated (figure 5.3), and the right panel shows the data for the case of the single pump modulated with different fluences for both pumps (figure 5.6d).

fluctuations already induced by the first pump, by looking at the residuals before and after the arrival of the second pump simultaneously for various pump delays for some example data sets, as shown in figure 5.5.

These results clearly illustrate nearly identical waveforms before the second pump arrives. On the other hand, we see that a small change in arrival time of the second pump can drastically modulate the amplitude, and that indeed the amplitude of the oscillation can be enhanced or suppressed by the second pump pulse.

Comparisons for different experimental conditions

We have repeated the experiments for a variety of experimental conditions, such as different probe wavelength, pump fluences, and temperatures, and consistently observed the peaks in the 2D-spectrum appearing at (f_k, f_k) diagonal frequencies and (f_0, f_k) off-diagonal frequencies. These findings are summarized in figure 5.6. This conversion was most clearly seen at the temperatures at the temperature of T=44 K, which is close to the phase transition temperature, where the spin wave amplitudes at this temperatures were maximized (see Chapter 4). Also, at this temperature, the frequency of the $k \neq 0$ propagating magnon mode is roughly double the frequency of the $k = 0$ magnon mode, $f_k \approx 2f_0$, which may further enhance the efficiency of the conversion through parametric amplification [163]. Moreover, we see that the frequency of the oscillations slightly decrease using the high fluence for both pumps. This can be attributed to the heating of the sample, which effect is expected to be strongly present when using the strongly absorbed 400 nm photons.

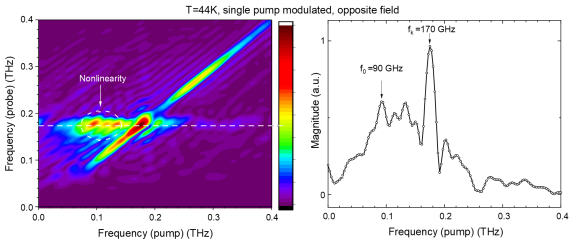

(a) Experimental 2D map, for similar conditions as the data in the main text, with opposite polarity of the external magnetic field.

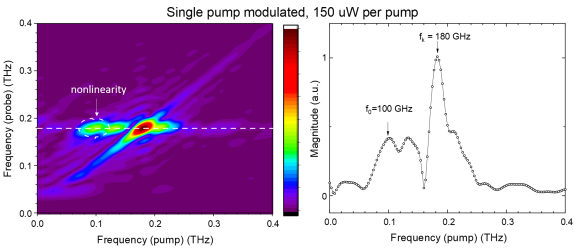

(b) Experimental 2D map, for T=44 K, one modulated pump, and low fluences of 0.04 mJ/cm^2 of both pumps.

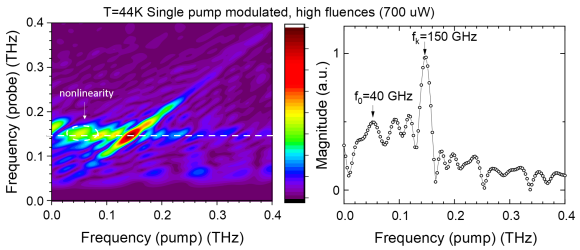

(c) Experimental 2D map, for T=44 K, one modulated pump, and high fluences of 0.2 mJ/cm^2 of both pumps.

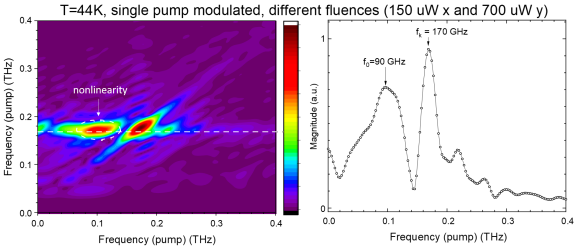

(d) T=44 K, single pump modulated, mixed fluences of 0.04 mJ/cm^2 for the modulated pump, and 0.2 mJ/cm^2 for the other pump.

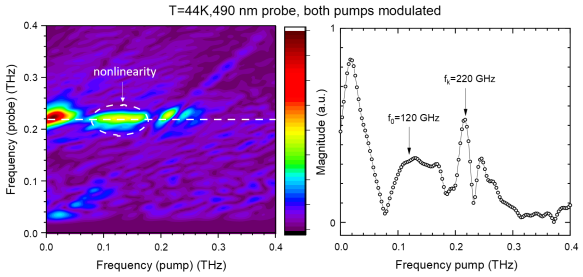

(e) T=44 K, both pumps modulated, probe wavelength 490 nm.

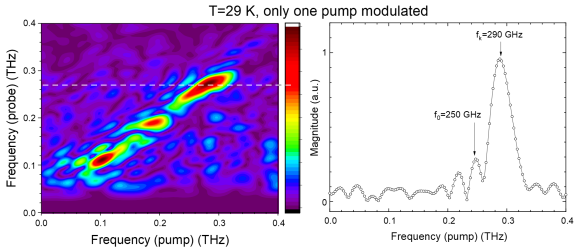

(f) T=29 K, single pump modulated, probe wavelength 660 nm.

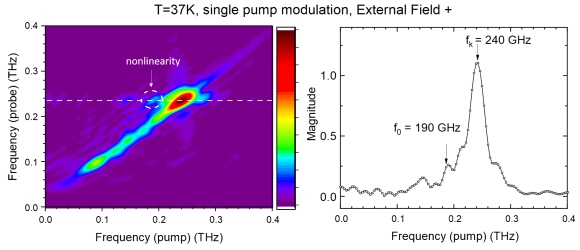

(g) T=37 K, single pump modulated, 660 nm probe wavelength, external field positive.

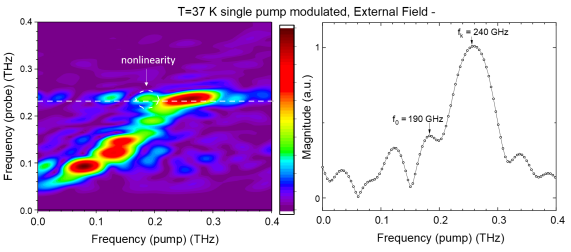

(h) T=37 K, 660 nm probe, single pump modulated, external field negative.

Figure 5.6: Summary of additionally measured data sets for various experimental conditions. The left panels show the 2D spectra obtained from magneto-optical detection experiments, and the right panels show the cross-sections highlighted by the dashed white line. The frequencies of the propagating magnon mode f_k and the uniform precession mode f_0 are indicated.

5.4 Simulations on the origin of nonlinear conversion

5.4.1 The light-induced nonlinear torque

To confirm our interpretation of the experimental data, we extended the theoretical formalism for the spin wave generation and detection as discussed in Chapter 2. Initially, we performed the linearization procedure to be able to find the linear solution, and omitted all terms containing products of $m(t)$, $l(t)$, and $h(t)$. In order to understand nonlinear interactions, we need to solve the Landau-Lifshitz-Gilbert equations while retaining the some nonlinear terms. In particular, in our double pump experiment we introduce the coupling between the dynamics magnetization components $m(t)$ and the effective magnetic field by the second light pulse $h(t)$.

The dynamics of the components of the **M** and **L** vector were previously shown in equation (1.20). To include the nonlinear interaction, we again used this set of equations as the starting point. We proceed with the solution by considering our experimental conditions. At the low temperatures at which the experiments were performed, the $HoFeO_3$ sample is in the Γ_2 phase, such that **M** aligns with the x-axis and **L** aligns with the z-axis. Moreover, as we saw in Chapter 4, the spin dynamics is excited through the Inverse Cotton-Mouton effect. The only non-zero component of the effective field induced by this effect will be directed along the x-axis [40, 41]. As a result, we obtain for the dynamics of the q-AFM mode:

$$\begin{aligned} \frac{1}{\gamma}\frac{dm_x}{dt} &= L_0[(K_z - K_x) + q\nabla^2]l_y \\ \frac{1}{\gamma}\frac{dl_y}{dt} &= L_0[J - q'\nabla^2]m_x + L_0 D l_z - L_0 h_x - l_z h_x \\ \frac{1}{\gamma}\frac{dl_z}{dt} &= -L_0\frac{D}{J}[(K_y - K_x) - q\nabla^2]l_y + l_y h_x \end{aligned} \tag{5.1}$$

The terms highlighted in red are the nonlinear terms containing the coupling between the magnons and the photons and thus indicate the terms that were neglected in the linear spin wave theory.

Moreover, we again assume small spin deflections such that we can write the spin deflections as follows in terms of angle (see also figure 5.7)

$$\begin{aligned} l_y(t) = L_y(t) - L_0^y = L_0 \sin(\phi(t)) \approx L_0\phi(t) \\ l_z(t) = L_y(t) - L_0^z = L_0 \cos(\phi(t)) \approx L_0(1 - \phi(t)^2/2) - L_0 \approx 0. \end{aligned} \tag{5.2}$$

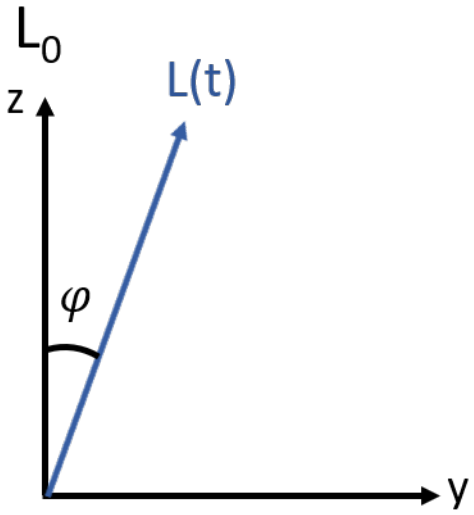

Figure 5.7: Schematic of the spin deflection in the Γ_2 phase.

In this approximation, we retrieve the nonlinear Klein-Gordon equation

$$\frac{d^2\phi(z,t)}{dt^2} = (\omega_E\omega_A + v_{sw}^2\nabla^2)\phi(z,t) - \omega_h\frac{dh_x(z,t)}{dt} + \omega_D\omega_h\phi(z,t)\tilde{h}(z,t). \tag{5.3}$$

Thus, the second pump pulse interacts with the magnon mode to create an additional torque on the spin system, which is given by $\omega_D\omega_h\phi(z,t)\tilde{h}(z,t)$. Here, $\omega_D = \gamma L_0 D$ is a parameter containing the Dzyaloshinskii-Moriya interaction. Note that this torque is only present during the arrival of the second pump pulse, as initially $\phi(z,t) = 0$, and this effect can be expected to only be observable in the canted antiferromagnets.

5.4.2 Magneto-Optical detection of the converted magnons

The spin dynamics is probed by the Brillouin scattering of the probe pulse, as described in Chapter 2. To understand the detection of the converted magnons, we apply a similar description for the detection of the converted propagating magnon modes. Here, the focus will be mainly on the explanation for the emergence of the off-diagonal peak in the 2D-spectrum as a result from the spin wave amplitude at frequency f_0.

We start the derivation by reminding ourselves that the MOKE rotation of a linearly polarized probe pulse due to the precessing magnetization is given by

$$\theta_K = i\frac{ak_0^2}{2k}\frac{t_0\tilde{t}_0}{r_0}\int_0^\infty dz' e^{2ikz'}M(z',t). \tag{5.4}$$

The linear solution which is induced by the first pump pulse was also derived in Chapter 3:

$$\phi_1(z,t) = \int_{-\infty}^{\infty} \left(A_{1f}(\omega) e^{-ik_{\mathrm{sw}}(\omega)z} + A_{1p}(\omega) e^{-z/d} \right) e^{i\omega t} d\omega, \tag{5.5}$$

where the first term and second terms correspond to the freely propagating solution and the driven precession respectively, which are related by the exchange boundary conditions.

$$\begin{aligned} A_{1p}(\omega) &= \frac{-i\omega\omega_h \tilde{h}(\omega)}{-\omega^2 + \omega_0^2 + 2i\alpha\omega - v_{\mathrm{sw}}^2/d^2} \\ A_{1f}(\omega) &= \frac{1/d - \xi}{\xi - ik_{\mathrm{sw}}(\omega)} A_{1p}(\omega) \end{aligned} \tag{5.6}$$

Now we return to the nonlinear Klein-Gordon equation and assume the form of the effective fields from the first and second laser pulse $h_1(z,t)$ and $h_2(z,t)$ to be identical. We consider the simplest case of the impulsive excitation arriving at time t_2 and the absorption of the pulse in a nanoscale region d near the surface ($\tilde{h}_{1,2}(z,t) = \delta(t - t_{1,2}) e^{-z/d}$).

The nonlinear Klein-Gordon equation for the spin deflection induced by the second pump pulse will be

$$\frac{\partial^2 \phi_2(z,t)}{\partial t^2} + (\omega_0^2 - v_{\mathrm{sw}}^2 \nabla^2)\phi_2(z,t) + 2\alpha \frac{\partial \phi_2(z,t)}{\partial t} = -\omega_h \frac{\partial h_2(z,t)}{\partial t} + \omega_D \omega_h \phi_1(z,t) \tilde{h}_2(z,t). \tag{5.7}$$

For simplicity, we define the arrival time of the first pump $t_1 = 0$ such that the second pump arrives at time $t_2 = \tau$. Because the linear solution is already known, in the following we will consider focus on the nonlinear torque. At a later stage, the effect of interference can be reintroduced by adding a similar linear solution including an additional phase factor $e^{i\omega\tau}$ to the solution induced by pump pulse 1. We can now again Fourier transform the Klein-Gordon equation with the nonlinear torque to obtain

$$(-\omega^2 + \omega_0^2 + 2i\alpha\omega - v_{\mathrm{sw}}^2 \nabla^2)\phi_2(\omega, z) = \omega_D \omega_h \phi_1(z,\tau) e^{-z/d} e^{-i\omega\tau}. \tag{5.8}$$

The solution to equation (5.8) will be similar to the linear solution, with modified amplitude. Besides, the nonlinear torque will be effectively confined to a region $d/2$ from the surface.

$$\phi_2(\omega, z) = A_{2f}(\omega) e^{-ik_{\mathrm{sw}}(\omega)z} + A_{2p}(\omega) e^{-2z/d} \tag{5.9}$$

We can again find the amplitude $A_{2p}(\omega)$ directly from equation (5.8) and relate the amplitude $A_{2f}(\omega)$ through the exchange boundary condition. The resulting amplitudes are

$$\begin{aligned} A_{2p}(\omega) &= \frac{\omega_D \omega_h \int_{-\infty}^{+\infty} p_1(\Omega) e^{-i(\omega-\Omega)\tau} d\Omega}{-\omega^2 + \omega_0^2 + 2i\alpha\omega - 4v_{\mathrm{sw}^2}/d^2} \\ A_{2f}(\omega) &= \frac{2/d - \xi}{\xi - ik_{\mathrm{sw}}(\omega)} A_{2p}(\omega) \end{aligned} . \tag{5.10}$$

Here the integral over Ω represents the Fourier Transform over the delay between the two pumps, which in essence represents the state of the spin deflection at the arrival time of the second pump τ.

Finally, as we measure in MOKE configuration and directed the probe pulse along the x-axis, we are sensitive to the x-component of the magnetization (this corresponds to the q-AFM mode in the Γ_2 phase.) Therefore, we convert the spin deflection of the antiferromagnetic moment to the x-component of the weak ferromagnetic moment using equation (5.1) and (5.2).

$$m_x(\omega, z) = \frac{1}{i\omega}(\omega_A - \frac{v_{\mathrm{sw}}^2}{\omega_E}\nabla^2)\phi(\omega, z) \tag{5.11}$$

We can now combine equations (5.4), (5.9), (5.10), and (5.11) to obtain the MOKE spectrum.

We will consider separately the detection of the driven component and the freely propagating component, which are

$$\theta_K^p(\omega, \Omega) = i\frac{ak_0^2}{2k}\frac{\tilde{t}_0 t_0}{r_0}\frac{1}{i\omega}(\omega_A - \frac{4v_{\mathrm{sw}}^2}{d^2\omega_E})(\frac{1}{2k + 2i/d})\frac{\omega_D\omega_h p_1(\Omega)e^{-i\omega\tau}}{-\omega^2 + \omega_0^2 + 2i\alpha\omega - 4v_{\mathrm{sw}}^2/d^2} \tag{5.12}$$

and

$$\begin{aligned} \theta_K^f(\omega, \Omega) = i\frac{ak_0^2}{2k}\frac{\tilde{t}_0 t_0}{r_0}\frac{1}{i\omega}(\omega_A + \frac{v_{\mathrm{sw}}^2 k_{\mathrm{sw}}(\omega)^2}{\omega_E})(\frac{2/d - \xi}{\xi - ik_{\mathrm{sw}}(\omega)}) \\ \times (\frac{1}{2k - k_{\mathrm{sw}}(\omega)})\frac{\omega_D\omega_h p_1(\Omega)e^{-i\omega\tau}}{-\omega^2 + \omega_0^2 + 2i\alpha\omega - 4v_{\mathrm{sw}}^2/d^2}. \end{aligned} \tag{5.13}$$

The full solution resulting exclusively from the nonlinear torque will then be given by the inverse Fourier Transform of the sum of equation (5.12) and (5.13). Finally, we reintroduced

the effect of interference by adding the linear solution (3.28) multiplied by a factor $(1+e^{i\omega\tau})$ to account for the arrival time of the second pump pulse. Using these expressions, we plotted a 2-dimensional spectrum, corresponding to the Fourier transforms along the probe delay ($t \rightarrow \omega$) and the pump delay ($\tau \rightarrow \Omega$). The spectrum obtained with this calculation is illustrated in figure 5.8. The numerical values of the parameters that were used are shown in table 5.1. Most of the values that were used in the simulations are material parameters and can be estimated from literature, or are controlled with the experimental conditions. The only parameters that are not accurately known are the confinement depth d and the effective field h_{eff}. The ratio of the excitation depth d and the spin wave velocity v_{sw} slightly affects the exact frequency of the antiferromagnetic resonance. In principle variation of these parameters allows for optimization of the match with the experimental data. We find that a good match is achieved for a excitation depth of $d = 60$ nm and spin wave velocity of $v_{\text{sw}} = 20$ km/s, which is very close to the reported parameters for $DyFeO_3$ [70]. Finally, we see that the amplitude of the nonlinear torque is proportional to the Dzyaloshinskii-Moriya interaction strength, the magnitude of the effective field, and the amplitude of spin precession, which itself is linear with the magnitude of the driving effective field. Therefore, in order to make the nonlinear conversion and interference simultaneously visible in the modelled spectrum, the effective field parameter needs to be tuned appropriately. We found that to see the nonlinearity in the simulations, a small effective field of no more than 10 Gauss is required. Note that this value is lower than the previously reported values for effective fields in pump probe experiments for studying ultrafast spin dynamics [39], which agrees with the fact that low fluences sufficed for launching the spin waves in $HoFeO_3$ (see Chapter 4).

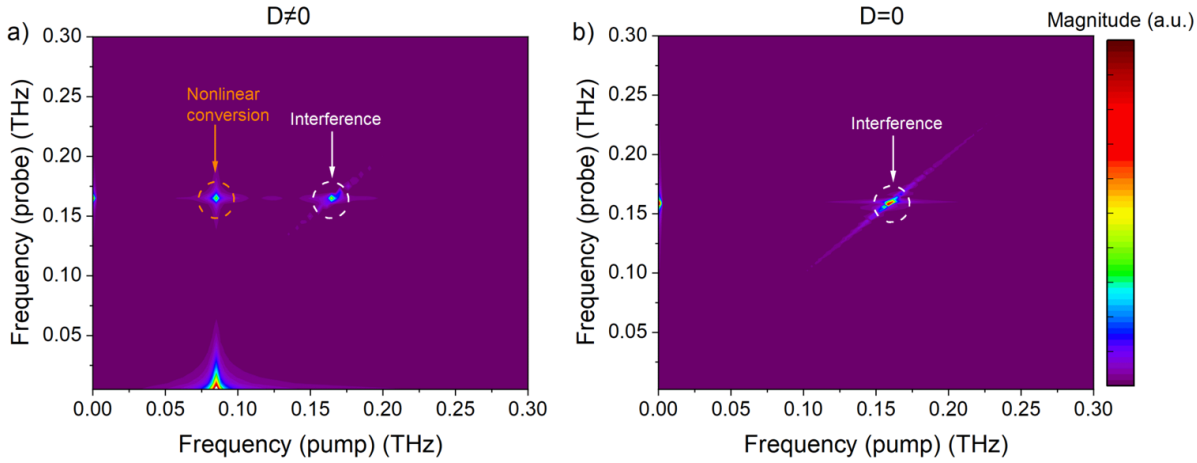

Figure 5.8: Calculated 2D MOKE spectrum for the experimentally relevant parameters for a) canted antiferromagnets with a nonzero Dzyaloshinskii-Moriya interaction ($D \neq 0$) and b) in the absence of the Dzyaloshinskii-Moriya interaction ($D = 0$).

Parameter	Value
ω_0	$2\pi * 100\,\mathrm{GHz}$
d	60 nm
v_{sw}	20 km/s
λ	660 nm
n	2.23
β	24°
α	$10^{-2}\omega_0$
h_{eff}	10 G
L_0	$2000\,\mathrm{emu/cm^3}$
M_0	$20\,\mathrm{emu/cm^3}$
J	$10^7/L_0$
K	$10^3/L_0$
D	$M_0/L_0 * J$
ξ	$\rightarrow\infty$

Table 5.1: Table summarizing the relevant parameters used in the simulations.

5.5 Conclusion

To conclude, we have demonstrated a strongly nonlinear effect in the canted antiferromagnet $HoFeO_3$ using the double-pump probe spectroscopic technique. This nonlinear effect is induced by the coupling between magnons excited by the first pump pulse and the second pump pulse, and is governed by the Dzyaloshinskii-Moriya interaction. This effect allows for amplification and supression of the propagating magnon modes, and the conversion from the static to the propagating magnon modes. We modeled the 2D-spectra in the MOKE experiment and found that the model agrees qualitatively accurately with the experimental observations. In very recent experiments, breakthroughs were made to demonstrate nonlinear interactions between light-induced magnetic, phononic, and electronic excitations, all these experiments were restricted to studying magnons at the center of the Brillouin zone [107, 164–166], thus not exhibiting any characteristics of magnon propagation. The findings discussed in this chapter hold the potential for realizing future magnonic data processing devices operating at THz frequencies, for which the nonlinear control of magnons is a crucial requirement.

Chapter 6

THz driven spin dynamics in $ErFeO_3$ and $TmFeO_3$

In this chapter, we employ the intense THz pulse setup that was introduced in Chapter 2, to search for high amplitude spin dynamics in the orthoferrites through direct resonant excitations. We study $ErFeO_3$ and $TmFeO_3$ samples that have very similar magnetic properties. We will show that despite the similarities in magnetic structure, the spin dynamics in the Spin Reorientation Transition (SRT) region shows a completely different behaviour. In $ErFeO_3$, we observe a drastic increase in spin dynamic amplitudes in the SRT region, which is absent in $TmFeO_3$, highlighting the role of the rare-earth ions in the spin dynamics of the iron ion spins.

6.1 Introduction

Intense THz pulses have been proposed to be an efficient tool to achieve efficient control over electronic spins, with the potential for resonantly driving high amplitude and high frequency spin dynamics. The electric field of such pulses couple to the electronic charge degree of freedom and has been shown to be able to induce insulator to metal phase transitions [167], while the magnetic field component of couples to the spin degree of freedom [104]. The electric-dipole interaction is generally an order of magnitude stronger than the magnetic-dipole contribution, making the control over the spin degree of freedom through the Zeeman interaction with the THz magnetic field relatively inefficient [113]. Thus, to achieve control over magnetism through direct resonant light-spin coupling, intense THz pulses are required. This has triggered research towards other indirect pathways to control magnetization through the electric field component of THz pulses.

Moreover, in particular in the orthoferrites, the energy scale of the electronic levels of the rare-earth ions lies in the meV (THz) range such that electronic transitions can be selectively excited with the electric fields of broadband THz pulses [113].

Recent studies have already shown promising results towards spin switching in antiferromagnets, using a metallic antenna mounted on a $TmFeO_3$ sample to locally enhance the THz field up to 10 MV/cm. Electric fields of this amplitudes were reported to be sufficient to drive the spins over their potential barrier to bring them in a new equilibrium orientation [168].

Here we study $ErFeO_3$ and $TmFeO_3$ in the search for high amplitude spin dynamics, and will highlight that the rare-earth ions play a decisive role in the spin dynamics of the iron spin system.

6.2 Magnetic Properties of $ErFeO_3$ and $TmFeO_3$

The magnetic properties of the orthoferrites were already introduced in Chapter 1, but the specific properties of the $ErFeO_3$ and $TmFeO_3$ will be summarized here. Both of these orthoferrites have a very similar magnetic structure. At room temperature, the iron spins are ordered antiferromagnetically, with a small canting angle due to the Dzyaloshinskii-Moriya interaction. At low temperatures $T < T_1$, both orthoferrites are in the Γ_2 phase, such that the weak ferromagnetic moment **M** is aligned along the crystallographic a-axis and the antiferromagnetic vector **L** is aligned the c-axis. At high temperatures $T > T_2$, the spin system is in the Γ_4 phase, with **M** along the c-axis and **L** along the a-axis. In the intermediate temperature region $T_1 < T < T_2$, the spin reorientation transition (SRT) occurs, where **M** gradually rotates from the a-axis to the c-axis. This magnetic phase is the Γ_{24} phase, and the angle of **M** with respect to the crystallographic a-axis is given by [113]

$$\theta_0 = \arcsin\left(\sqrt{\frac{T - T_2}{T_1 - T_2}}\right). \tag{6.1}$$

For $ErFeO_3$, the boundaries of the SRT region are $T_1 = 88\,\mathrm{K}$ and T_2=97 K [169], and for $TmFeO_3$ these temperatures are $T_1 = 85\,\mathrm{K}$ and $T_2 = 93\,\mathrm{K}$ [170]. The AFMR contains two modes, the q-FM mode and the q-AFM mode (see also Chapter 3). The q-FM mode corresponds to the precession of **M**, and the q-AFM mode are the oscillations in the length of the **M**. This SRT and the modes of AFMR are summarized in figure 6.1.

Although the rare-earth magnetic moments are paramagnetic, the rare-earth 4f moments are polarized by the antiferromagnetic ordering of the iron spins. Only below the Néel temperature for the rare-earth ions, the spins in the rare-earth order antiferromagnetically.

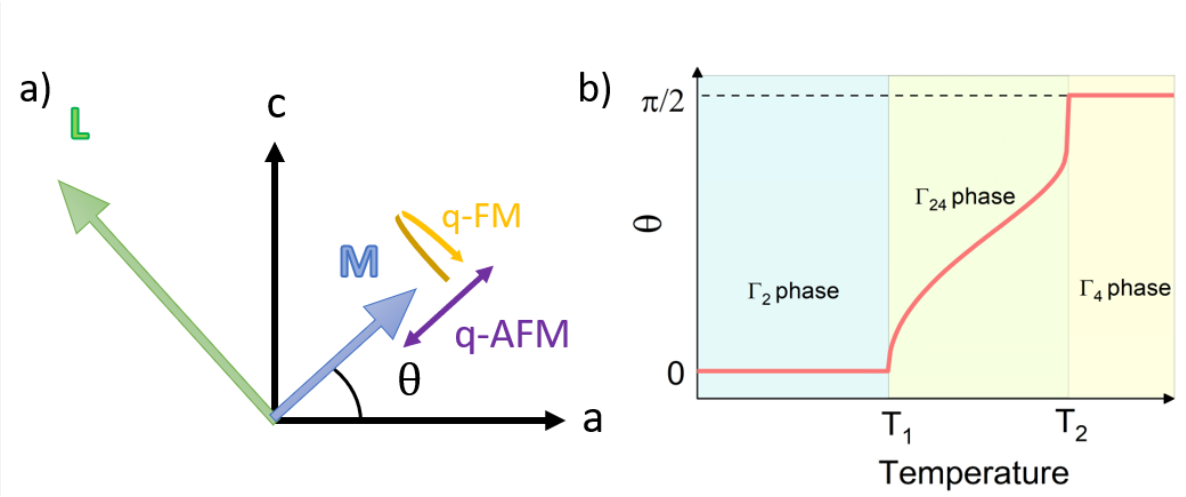

Figure 6.1: a) Illustration of the SRT of the $ErFeO_3$ and $TmFeO_3$ with an indication of the two modes of AFMR. b) Angle θ of the weak ferromagnetic moment **M** with respect to the a-axis as a function of temperature.

The Néel temperature of the Er sublattice is $T_N \approx 4$ K for $ErFeO_3$ [171] and antiferromagnetic ordering of the Tm sublattice has not been observed at temperatures above 1.6 K in $TmFeO_3$ [172].

The 4f spins in the rare-earth ions play an important role in the static and dynamic properties of the iron 3d spins due to their strong coupling [173].

The interaction of the rare-earth electrons with the surrounding crystal field leads to splitting of the rare-earth 4f electronic levels. On top of this splitting, if the rare-earth is a Kramers ion with an odd number of electrons in the 4f shell, the d-f exchange further breaks the symmetry and further lifts the degeneracy of the energy levels [174, 175].

The splitting of the Kramers doublets introduces an important difference between the $ErFeO_3$ and $TmFeO_3$. The Er^{3+} ion has an odd number of electrons in the 4f shell, and is thus a Kramers ion that shows the crystal field splitting of the energy levels into doublets. In contrast, the 4f shell of the Tm^{3+} ion contains an even number of electrons, and is thus a non-Kramers ion in which the crystal field removes the degeneracy entirely.

As a result, the energy level structure of the 4f electrons in $ErFeO_3$ is more complex than in $TmFeO_3$, and contains a multitude of possible high frequency transitions, ranging from 1.2-1.5 THz, and low frequency transitions (due to the Kramers doublet splitting) of approximately 100 GHz [58, 176]. In $TmFeO_3$, the crystal field splitting results in energy levels that are 0.55 THz, 1.2 THz and 2.1 THz from the ground state [170]. On top of this, in $RFeO_3$, impurity Fe^{3+} transitions around 300 GHz have been reported [177].

Thus, we see that besides resonant coupling of the magnetic field of THz pulses to the

AFMR, the electric field component can also be used to excite electronic transitions of the rare-earth ions. This fact has been exploited previously to demonstrate nonlinear spin dynamics, due to THz-induced changes to the magnetic anisotropy [113].

6.3 Experimental Setup

In our experiment, we drive the spin dynamics in $ErFeO_3$ and $TmFeO_3$ with intense THz pulses generated by Optical Rectification and focused on the sample by a set of three parabolic mirrors, and probe the spin dynamics by measuring the Faraday rotation of time delayed probe pulses using a Wollaston prism and a pair of balanced photodetectors, as was described in Chapter 2. A schematic of the experiment is illustrated in figure 6.2. We measured the THz pulse with EOS, and obtained an electric field strength of about 300 kV/cm, such that the corresponding magnetic field is approximately 0.1 T (see figure 6.2b). The samples were placed in a closed cycle liquid Helium cryostat, allowing us achieve temperatures down to 3.5 K.

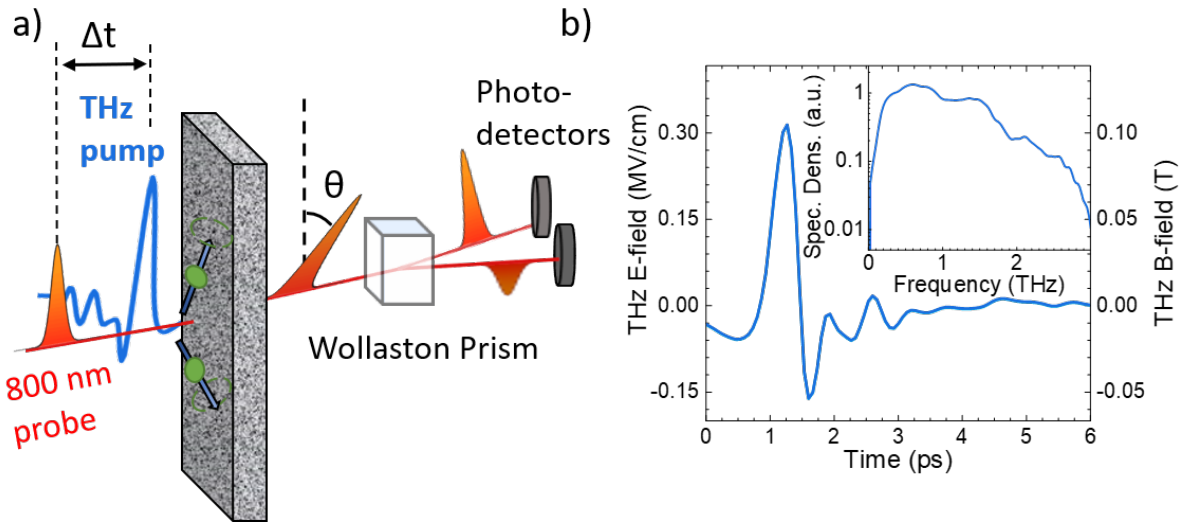

Figure 6.2: a) Illustration of the THz pump-optical probe experiment (more details in Chapter 2). b) Time resolved THz pulse by EOS and its spectrum (inset).

We used a pair of wire-grids polarizers to control the THz fluence. Moreover, the combination of two wire-grids polarizers allowed us to control the polarization of the THz pulses.

6.4 THz-induced spin dynamics in $ErFeO_3$

In our experiment, we studied a b-cut $ErFeO_3$ sample, such that the wire grids polarizers allowed us to set the magnetic field of the THz pulse either along the a-axis or along the c-axis. We measured the temperature dependence for a wide range of temperatures, across the SRT. Indicative results of the measured spin dynamics are shown in figure 6.3.

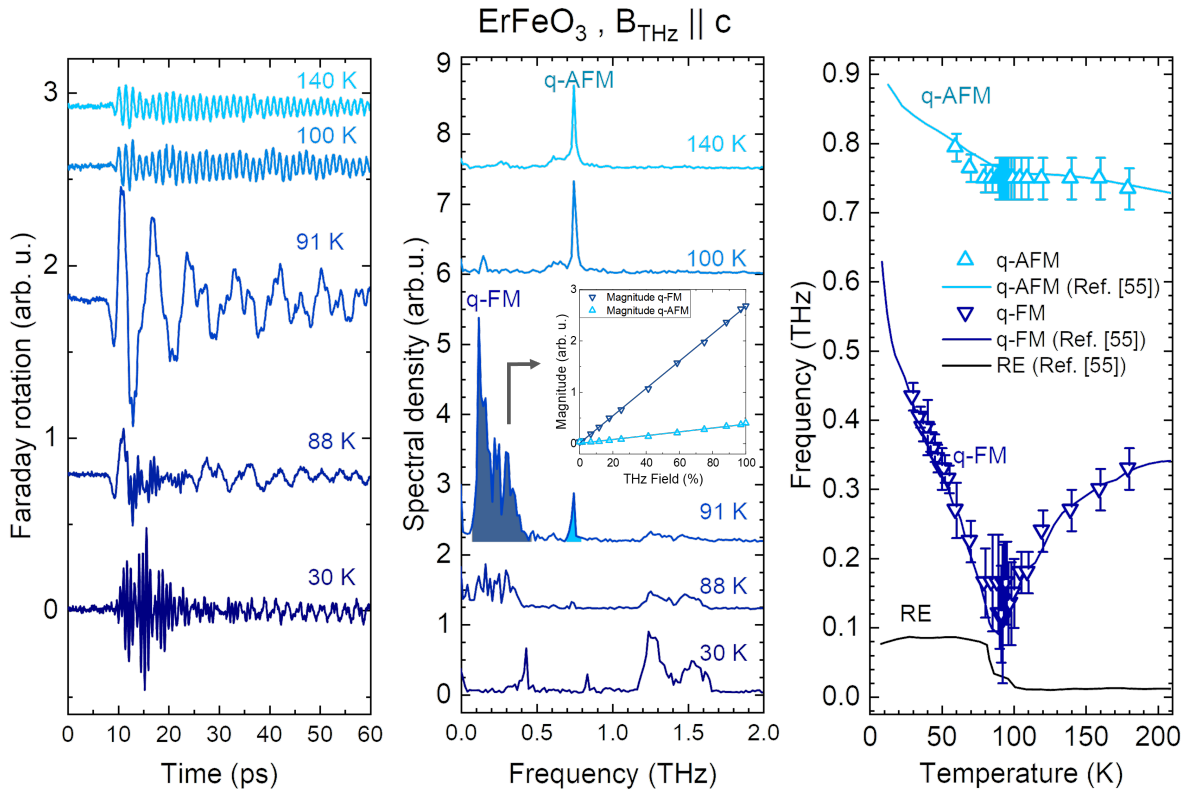

Figure 6.3: a) Temperature dependence of the THz-driven spin dynamics in $ErFeO_3$. b) Fourier transforms of the time domain data in a). The inset shows the amplitude of the q-FM and the q-AFM mode as a function of the THz fluence, extracted as the integrated spectral weight of the shaded regions. c) Extracted frequencies of the q-FM and q-AFM mode extracted from the spectra. The error bars indicate an estimation of the FWHM of the peaks. The solid lines indicate digitized data from reference [55].

In figure 6.3a), we see a distinct short envelope with high frequency oscillations at low temperatures. The Fourier transformation (figure 6.3b) demonstrates that these oscillations correspond to a broad feature of modes, centered around 1.2 THz and 1.5 THz. This feature is suppressed upon approaching the SRT temperature. We attribute these high frequency oscillations to the magnetic-dipole active transitions of the crystal-field split Er^{3+} energy levels, which are resonantly excited by the magnetic field of the THz pulse.

Besides this high frequency mode, we also observe the q-FM mode and the q-AFM mode. In our experiment, the THz magnetic field component was polarized along the crystallographic c-axis, thus in the Γ_2 phase, the magnetic field $\mathbf{B}_{\mathrm{THz}}$ was orthogonal to the weak ferromagnetic moment **M**. In the high temperature Γ_4 phase, **M** is oriented such that is parallel with $\mathbf{B}_{\mathrm{THz}}$. In our experiment, the q-FM mode is dominant in the Γ_2 phase, whereas in the high temperature Γ_4 phase, the q-AFM mode is dominant. This is in accordance with the selection rules [166] and can be seen from equations (1.21) and (1.22).

We tracked the frequencies of the q-FM mode and the q-AFM mode as a function of temperature from the spectra, as shown in figure 6.3c). We see that the frequencies of the AFMR modes match excellently with previously reported data [55].

Furthermore, from the literature data one can observe that the frequencies of one of the rare-earth mode and the q-FM mode display an avoided crossing around the SRT temperature. This is an indication of the strong interaction between the iron spins and rare-earth orbitals at this temperature.

Interestingly, across the SRT, we observe a giant enhancement in the q-FM amplitude, with a maximum in the middle of the SRT around T=91 K. At these temperatures, the q-FM mode seems to merge in a broadband feature of modes, which we may attribute to the interaction of the magnetic mode corresponding to the low frequency transitions in the split Kramers doublets with the q-FM mode.

At the same time, we see a gradual increase of the q-AFM amplitude across the SRT. This can be simply understood by the fact that the **M** gradually rotates towards the c-axis. Thus, the projection of the magnetic field component of the THz pulse on **M** increases, resulting in an increased excitation of the q-AFM mode.

The increase in the q-FM amplitude is actually unexpected, as the projection of **M** on the axes orthogonal to $\mathbf{B}_{\mathrm{THz}}$ decreases.

To propose a potential mechanism for the enhancement of the q-FM mode, we checked how the amplitudes were affected by the THz fluence. To this end, we controlled the electric field strength of the THz pulses with a pair of wire-grid polarizers, which were carefully calibrated using EOS. The obtained results are shown in the inset in figure 6.3b).
Furthermore, we investigated the probe polarization dependence to elucidate the detection mechanism of these various modes. We measured the spin dynamics for various probe polarization both at T=42 K and T=92 K, and extracted the amplitudes while accounting for the phase from the real part of the Fourier transformation. The polarization dependencies are shown in figure 6.4.

We see that at T=42 K, the oscillations barely depend on the incident probe polarization.

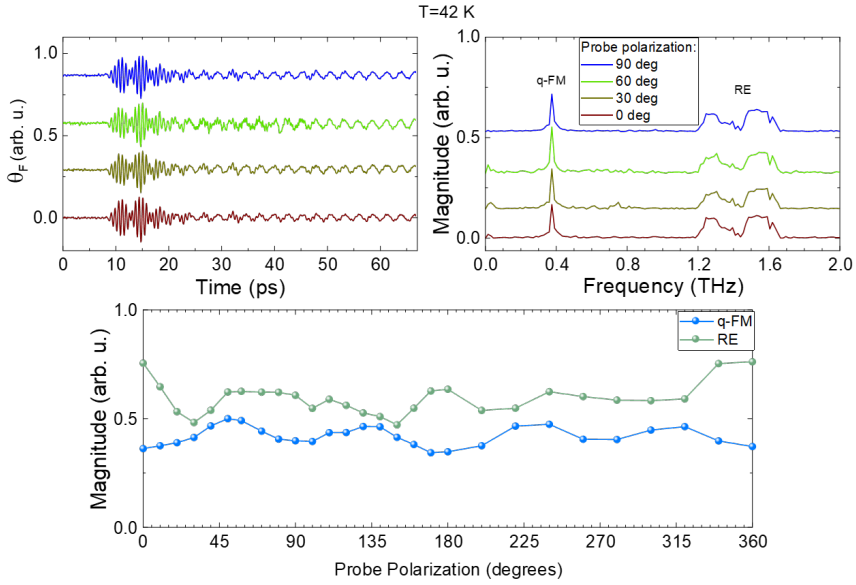

(a) Probe polarization dependence at T=42 K

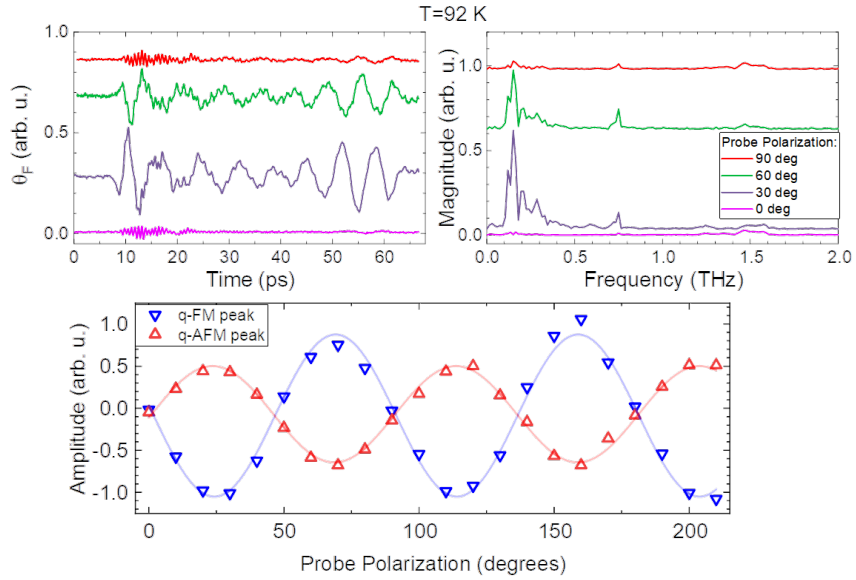

(b) Probe polarization dependence at T=92 K.

Figure 6.4: Probe Polarization dependencies at T=42 K and T=92 K. The top left panel shows the measured Faraday rotation, and the Fourier transforms are shown in the right panel. The amplitude of the oscillations were extracted from the real part of the Fourier transforms, to account for the changes in sign. The amplitude as function of probe polarization angle is plotted in the bottom panels.

This scenario implies that the detection mechanism is dominated by the Faraday effect. On the other hand, at T=92 K, we see a strong dependence of the amplitudes of both the q-FM and q-AFM mode on the incident probe polarization. This corresponds to the dominant Cotton Mouton Effect for the detection. Therefore, it is important to note that the enhancement in the amplitude of the q-FM mode is only detectable at the appropriate probe polarization.

To check the polarization dependence, we rotated the sample by 90 degrees, such that the a-axis was aligned with the magnetic field component of the THz, and measured the spin dynamics at various temperatures. The results are shown in figure 6.5.

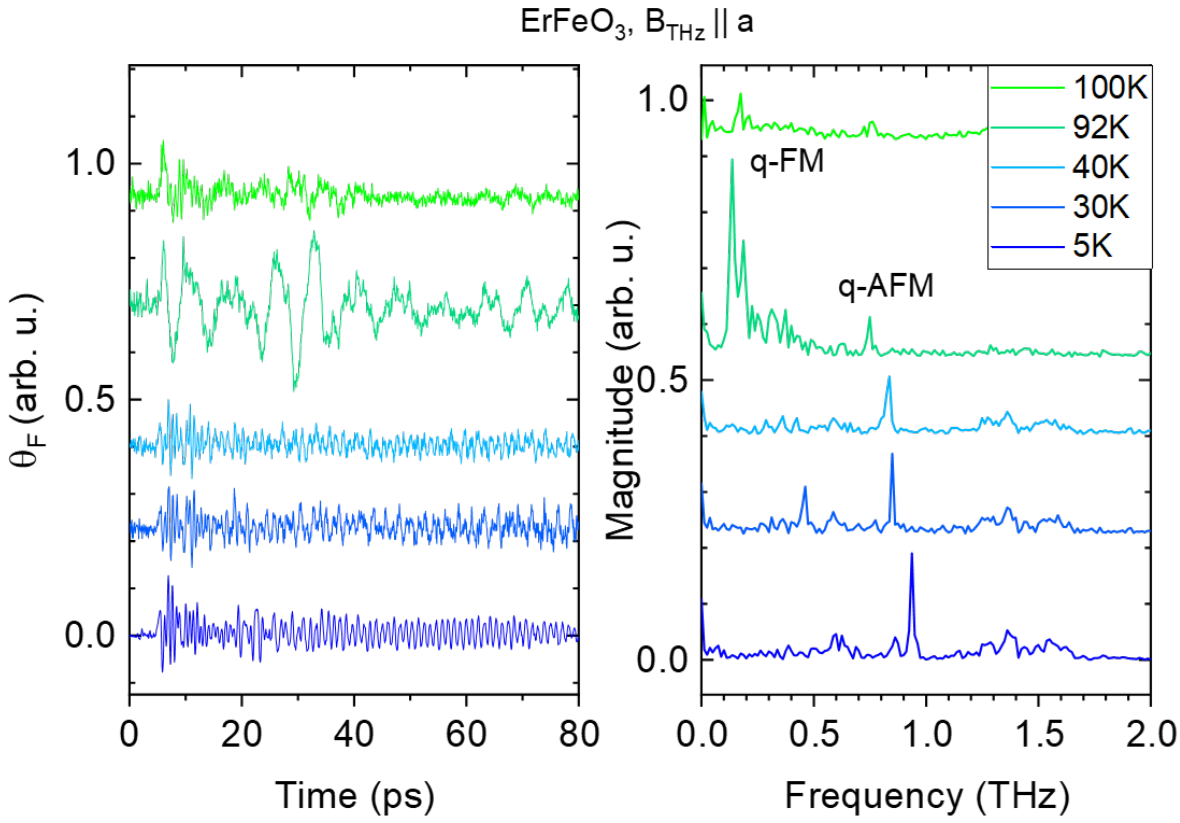

Figure 6.5: a) Faraday rotation as a result of THz-induced spin dynamics for various temperatures. b) Fourier transforms of the data in panel a).

For this orthogonal orientation of the sample, we observe an opposite pattern in the emergence of the modes of AFMR. In this case, in the low temperature Γ_2 phase, **M** aligns with the magnetic field of the THz and thus the q-AFM mode is excited. In the high temperature Γ_4 phase, **M** is orthogonal to $\mathbf{B}_{\mathrm{THz}}$, thus the q-FM mode is excited. In the middle of the SRT, the amplitude of the q-FM mode is again maximized. Moreover, we see that the excitation of the rare-earth modes is strongly polarization dependent. These modes are only excited in

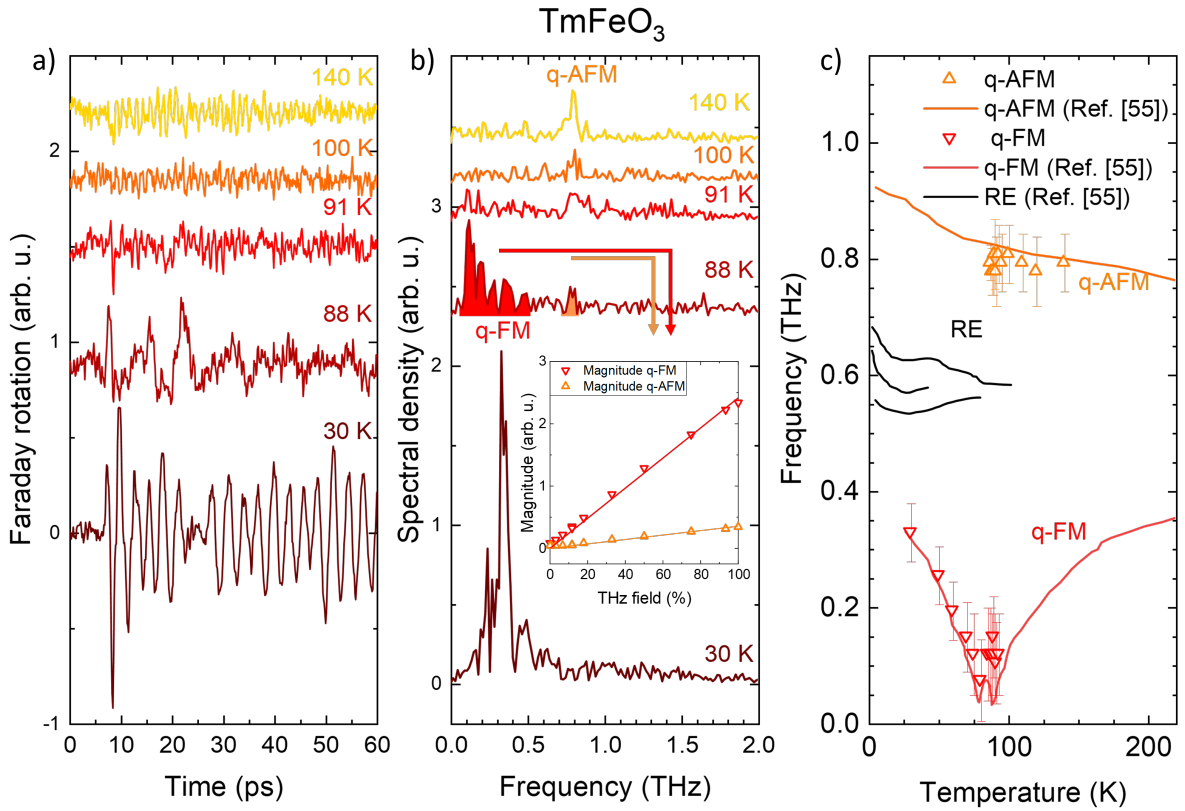

Figure 6.6: a) Temperature dependence of the THz-driven spin dynamics in $TmFeO_3$. b) Fourier transforms of the time domain data in a). c) Extracted frequencies of the q-FM and q-AFM mode extracted from the spectra. The error bars indicate an estimation of the FWHM of the peaks. The solid lines indicate digitized data from reference [55].

the low temperature phase, when the THz magnetic field is aligned with the crystallographic a-axis.

6.5 THz-induced spin dynamics in $TmFeO_3$

To see if a similar enhancement can be observed in other orthoferrites, we additionally studied a sample of $TmFeO_3$, whose properties are very similar to $ErFeO_3$. The indicative results are shown in figure 6.6.

In our $TmFeO_3$ sample, the a-axis was aligned perpendicular to the magnetic field of the THz, such that similarly to $ErFeO_3$, we again observe the q-FM mode in the Γ_2 phase and the q-AFM mode in the Γ_4 phase. In contrast to the $ErFeO_3$ measurements however, we find that the q-FM mode is actually suppressed in the $TmFeO_3$. This can be understood as the projection of the $\mathbf{B}_{\mathrm{THz}}$ on $\mathbf{M}$ increases as the magnetization rotates over the SRT. Besides, no

features of the rare-earth modes are visible in $TmFeO_3$.

As a nonlinearity in the q-FM amplitude was previously observed in $TmFeO_3$ [113], we checked the dependence of the amplitude on the THz fluence. As shown in the inset in figure 6.6, the amplitude of the q-FM mode scales linearly. This may be attributed to the fact the the measurements were performed with a lower THz magnetic field than the ones reported in [113], as in that report the $LiNbO_3$ was cryocooled, which gives rise to a broader THz spectrum with higher peak amplitudes.

6.6 Comparison between $ErFeO_3$ and $TmFeO_3$ and theoretical interpretation

In the previous sections, we already indicated differences of the spin dynamics in $ErFeO_3$ and $TmFeO_3$, particularly in the amplitude of the q-FM mode in spite of the similar properties of these orthoferrites. Here, we will make a direct comparison of the amplitudes of the modes in , and provide a theoretical explanation for the enhancement of the q-FM mode in $ErFeO_3$, and the lack thereof in $TmFeO_3$.

To compare the results directly, we extracted the ampltidudes of the q-FM and q-AFM modes from figures 6.3 and 6.6. These are plotted in figure 6.7. As the spin dynamics is driven resonantly, and the spectral weight of the THz pulse varies strongly, particularly for low frequencies below 300 GHz (see figure 6.2b), we normalized the amplitudes with respect to the spectral amplitude of the THz pulse.

As mentioned before, we can explain the increase of the q-AFM mode, by the increased projection of $\mathbf{M}$ on $\mathbf{B}_{\mathrm{THz}}$, $\sin(\theta_0(T))$, as $\mathbf{M}$ rotates in the SRT. The discrepancies of the experimentally obtained amplitudes with the expected torque due to the projection may be explained by the fact that the detection can also be affected by the rotation of the magnetization, especially since a strong dependence of the amplitudes on the incident polarization was observed.

The giant amplitudes of the q-FM mode in the middle of the SRT cannot be explained by such means. The dome-like structure of the q-FM as a function of temperature can be well fitted with a function $\sin(\theta_0(T))\cos(\theta_0(T))$, where $\theta_0(T)$ is the angle of $\mathbf{M}$ with the a-axis (see figure 6.1) and is given by equation (6.1). In the following section, we propose a theory that can explain this observed trend.

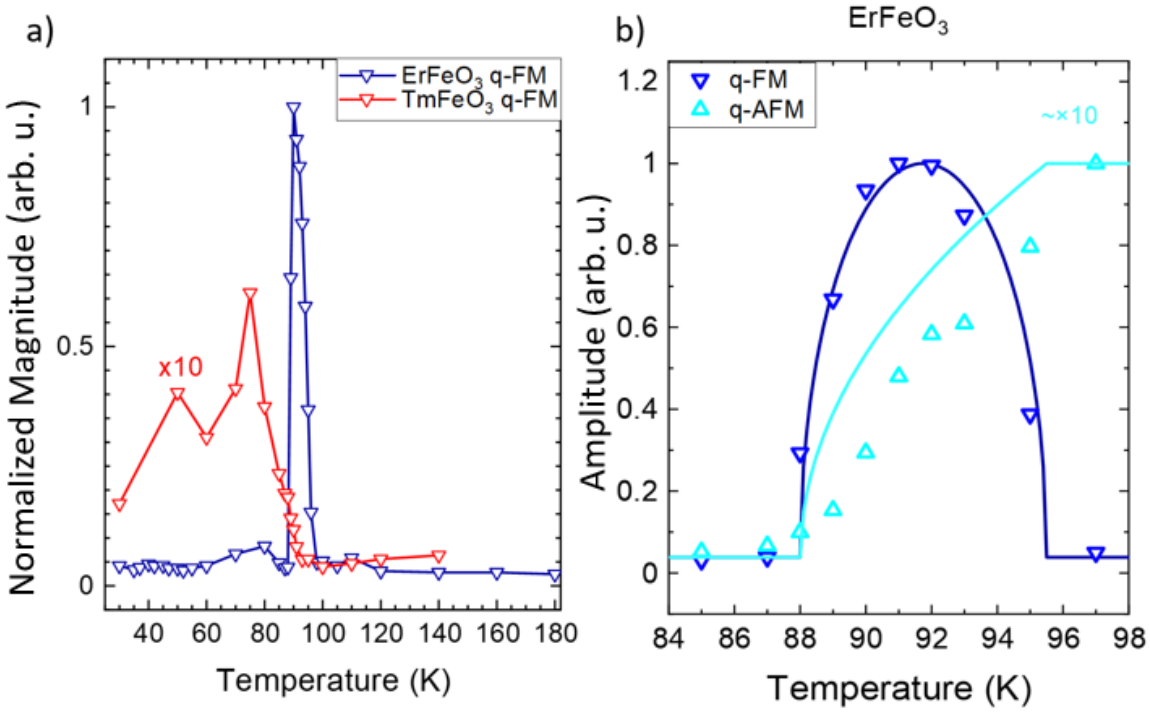

Figure 6.7: Comparison of the amplitudes of a) the q-FM mode in $ErFeO_3$ and $TmFeO_3$ and b) the q-FM mode and q-AFM mode as a function of temperature. The solid lines in b) are guides to the eye drawn from the theoretical model. The amplitudes are normalized with the spectral weight of the THz pulse. The q-FM amplitudes of $TmFeO_3$ are magnified for better visibility.

Theory of the effect of the Rare-Earth on the q-FM mode

As we have seen a completely different trend in the amplitude of the q-FM mode in $ErFeO_3$ and $TmFeO_3$ across the SRT, we propose here a theoretical explanation by considering the interaction of the iron spins with the rare-earth ions.

The free energy of the orthoferrites is determined by the interactions between the spins of the d-electrons in Fe^{3+} and the f-electrons in the Er^{3+} ions. The full magnetic energy density of the system is

$$\mathscr{F}_m = \mathscr{F}_{\text{d-d}} + \mathscr{F}_{\text{d-f}} + \mathscr{F}_{\text{f-f}}. \tag{6.2}$$

Here, $\mathscr{F}_{\text{d-d}}$ is the energy density of the Fe^{3+} 3d-electron spin system and $\mathscr{F}_{\text{f-f}}$ is the free energy density of the 4f-electron spin system on the rare-earth ions. The free energy density from the interaction between these d-electrons and f-electrons is given by [173]

$$-\frac{\mathscr{F}_{\text{d-f}}}{N} = f_x[\mu_x(H_x + aF_x) + B'_z G_z] + f_y\mu_y(H_y + aF_y) + f_z[\mu_z(H_z + aF_z) + B_x G_x] \\ + c_x\mu_{xy}(H_y + aF_y) + c_y[\mu_{yx}(H_x + aF_x) + B''_z G_z] + c_z B_y G_y. \quad (6.3)$$

Here, f and c indicate the ferromagnetic and antiferromagnetic moment of the rare-earth f-spins respectively, and F and G indicate the ferromagnetic and antiferromagnetic moment of the iron spins respectively. The isotropic exchange constants is denoted by a, and the anisotropic exchange constants are denoted by B.

With the energy of the d-f electrons interactions known, the ground state can be found by minimizing the free energy with respect to the four magnetic vectors. It was shown in reference [173] that in this case, the orientation of the magnetic moments of the rare-earth ions are defined by the orientation of the magnetic moments in the iron ions. The only nonzero components are then

$$\begin{aligned} F_x &= F_0 G_z \\ F_z &= -F_0 G_x \\ f_x &= \frac{(a\mu_x F_x + B'_z G_z)\lambda'_5 + (a\mu_{yx} F_x + B''_z G_z)\lambda_7}{\lambda'_1\lambda'_5 - \lambda_7^2} \\ f_z &= \frac{a\mu_z F_z + B_x G_x}{\lambda'_3} \\ c_y &= \frac{(a\mu_{xy} F_x + B''_z G_z)\lambda'_1 + (a\mu_x F_x + B'_z G_z)\lambda_7}{\lambda'_1\lambda'_5 - \lambda_7^2} \end{aligned} \quad (6.4)$$

In the Γ_{24} phase, we can parametrize the magnetic moments of the Fe^{3+} spins in terms of the rotation angle. These magnetic moments can be written as

$$\begin{aligned} G_x &= G\cos(\theta) \qquad F_x = -F\sin(\theta) \\ G_z &= G\sin(\theta) \qquad F_z = F\cos(\theta) \end{aligned} \quad (6.5)$$

Using the free energy of the spin system, we can obtain the equation of motion for the angle of the spin deflection of the magnetic moments of the iron spins as is given by the Lagrangian formalism [113].

Substituting the expressions (6.5) into the equilibrium components of the rare earth moments in equation (6.4), one can see that the components f_x and c_y are proportional to

$\sin(\theta)$, and f_z is proportional to $\cos(\theta)$.

We now assume that the THz pump pulse induces spin dynamics of the ferromagnetic vector **f** and antiferromagnetic vector **c** of the rare-earth subsystem, thus bringing the rare-earth spins out of their equilibrium orientation. We assume that the deflection from equilibrium is small, and that at the same time, the iron spins are frozen. Thus, effectively the orientation angle of the rare earth moments will become $\theta \rightarrow \theta + \delta\theta$. Substitution of this THz induced spin deflection in the components of the rare earth moments and applying the sum rules assuming $\delta\theta << 1$ yields

$$\begin{aligned} f_x &= K_1 \sin(\theta + \delta\theta) \approx K_1 \left[\sin(\theta) + \delta\theta \cos(\theta)\right] \\ f_z &= K_2 \cos(\theta + \delta\theta) \approx K_2 \left[\cos(\theta) - \delta\theta \sin(\theta)\right] \\ c_y &= K_3 \sin(\theta + \delta\theta) \approx K_3 \left[\sin(\theta) + \delta\theta \cos(\theta)\right] \end{aligned} \tag{6.6}$$

Here K_1, K_2 and K_3 are proportionality constants that are extracted from equation (6.4).

Due to the coupling between the iron spins and the rare-earth spins, the deflection of the rare-earth spins changes the free energy and will therefore act as an additional torque on the magnetic moments of the iron ions.

This torque can be found from the Euler-Lagrange equation, which reads

$$\frac{d}{dt}\left(\frac{d\mathscr{L}}{d\dot{\theta}}\right) - \frac{d\mathscr{L}}{d\theta} = 0. \tag{6.7}$$

The Lagrangian is given by $\mathscr{L} = \mathscr{T} - \mathscr{F}$, where $\mathscr{T}$ is the kinetic energy of the system and $\mathscr{F}$ is the free energy of the system. The equations of motion are already well known for the iron system in the orthoferrites, and will yield the Klein-Gordon equations in the linear regime, or the sine-Gordon equations in the nonlinear regime [66].

The extra torque induced by the small spin deflection of the rare-earth moments $\delta\theta$ will arise from the term $\frac{d\mathscr{L}}{d\delta\theta}$, or $-\frac{d\mathscr{F}}{d\delta\theta}$. For simplicity, we now assume that the magnetic field of the THz only acts at $t = 0$ and then induces free precession of the rare-earth moments, such that we can neglect the magnetic field components in the expression for the free energy. Moreover, the neglection of the magnetic field may be justified by the fact that the magnetic field of the THz pulse is orders of magnitude smaller than the typical exchange fields.

Now, the expanded non-zero components can be substituted in our expression for the free energy, yielding

$$-\frac{\mathscr{F}_{\text{d-f}}}{N} = K_1\big[\sin(\theta)+\delta\theta\cos(\theta)\big]\big(\mu_x aF+B_z'G\big)\sin(\theta)+K_2\big[\cos(\theta)-\sin(\theta)\delta\theta\big]\big(\mu_z aF+B_xG\big)\cos(\theta)$$
$$+K_3\big[\sin(\theta)+\delta\theta\cos(\theta)\big]\big(\mu_{yx}aF+B_z"G\big)\sin(\theta). \quad (6.8)$$

Calculating the derivative of the free energy with respect to the spin deflection angle of the rare earth moment $\delta\theta$ yields the following torque:

$$\Delta\mathscr{T} = \frac{d\mathscr{L}}{d\theta} = [-K_1(\mu_x aF+B_z'G)-K_2(\mu_z aF+B_xG)+K_3(\mu_{yx}aF+B_z"G)]\sin(\theta)\cos(\theta). \quad (6.9)$$

Thus, we see that the strength of this torque is determined by the angle θ in the ac-plane and follows the symmetry of $\cos(\theta)\sin(\theta)$. This torque due to the d-f coupling is thus maximized when $\theta = \pi/4$, which occurs exactly at the midpoint of the Γ_{24} phase. The temperature dependence of the amplitude of the q-FM mode that we found experimentally is in excellent agreement with this symmetry.

The theoretical explanation described above can well explain why the enhancement occurs only in $ErFeO_3$ and not in $TmFeO_3$. We already saw from the digitized literature data in figure 6.3 that the frequencies of the rare-earth mode and the q-FM mode cross, suggesting a strong interaction between the iron spins and the rare-earth spins. The crossing of the frequencies of these two modes allow for the efficient resonant transfer of the rare-earth spin precession to the iron spin precession. Thus, the low energy splitting of the Kramers doublets in $ErFeO_3$ that gives rise to the low frequency rare-earth modes plays a crucial role in the enhancement of the q-FM mode.

6.7 Observation of second harmonics in $ErFeO_3$

Further optimizations of the experimental setup allowed us to observe clear features of the second harmonic of the q-FM mode, as summarized in figure 6.9.

All throughout the Γ_2 phase where the q-FM mode is most pronounced, we see the emergence of an additional high frequency oscillations, next to the small q-AFM feature (figure 6.9b). We tracked the frequency of the modes and see that the additional peak consistently appears at double the frequency of the q-FM mode, and overlaps with the q-AFM mode at low temperatures. (figure 6.9c). In the SRT, the feature becomes hidden in the broad structure

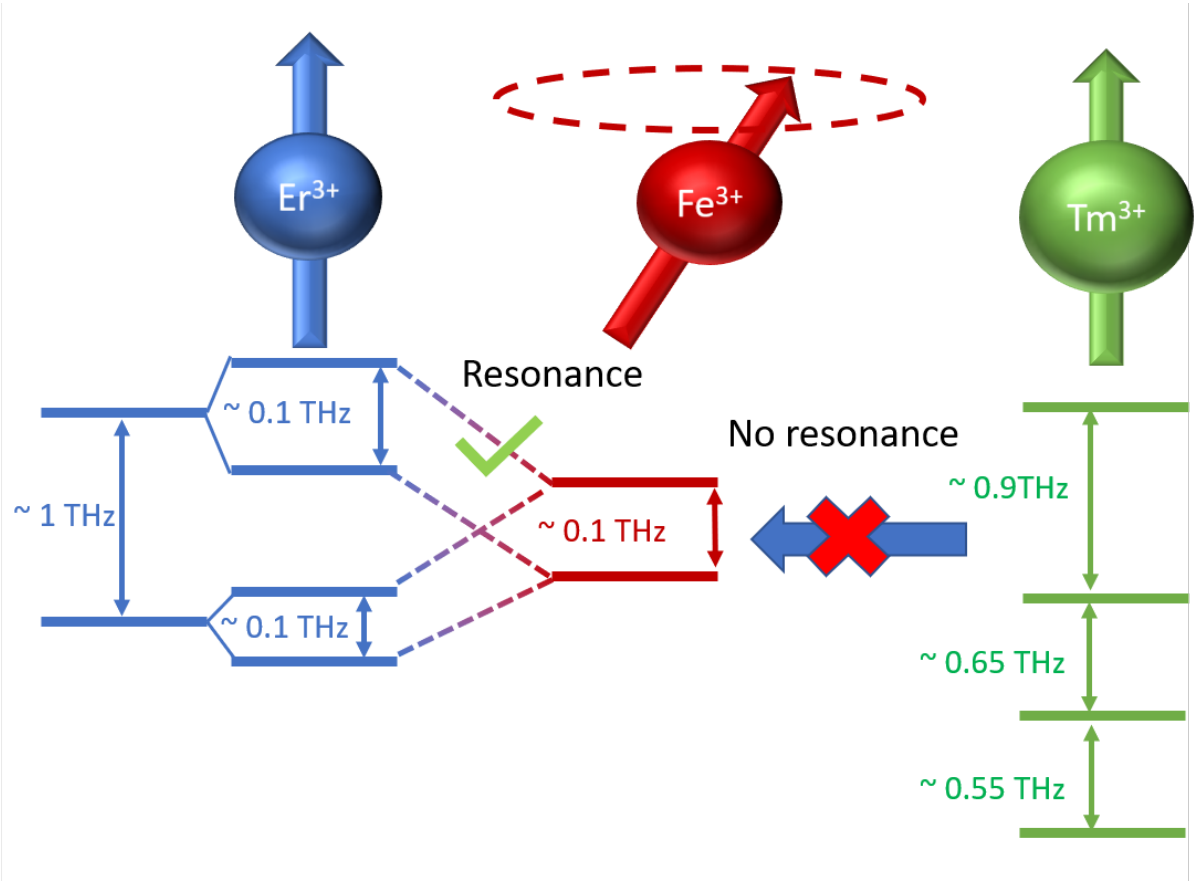

Figure 6.8: Schematic of energy level diagrams of the $ErFeO_3$ and $TmFeO_3$ and the mechanism of the resonant enhancement of the q-FM mode in the SRT in $ErFeO_3$ and the lack thereof in $TmFeO_3$.

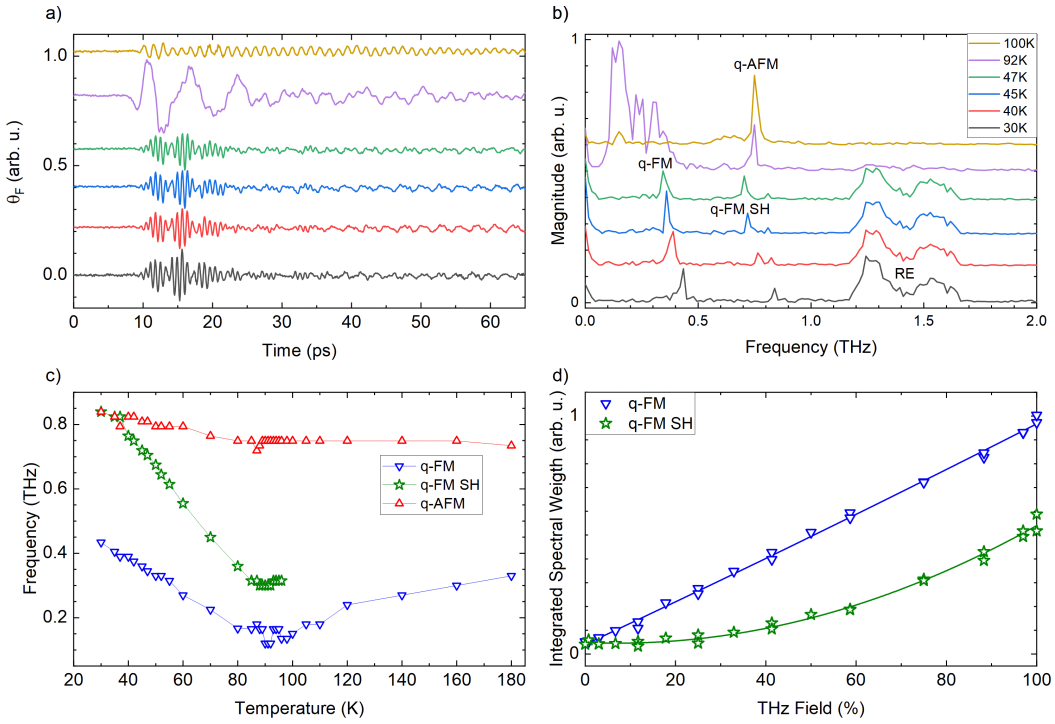

Figure 6.9: Observation of the second harmonic of the q-FM mode in $ErFeO_3$. a) Time traces of the Faraday rotation at various temperatures. b) The corresponding Fourier transforms, highlighting the observed q-FM mode and its Second Harmonic (SH), the q-AFM and the Rare-Earth (RE) modes. c) Extracted frequencies of the q-FM mode the q-FM SH, and the q-AFM mode. d) Dependence of the amplitude of the q-FM mode and its SH as a function of the THz electric field strength.

of low frequency peaks. The observation of Second Harmonics (SH) is a clear signature of nonlinearity, potentially indicating the achievement of high amplitude spin precession. To confirm this nonlinearity, we checked the dependence of the amplitudes of the q-FM mode and the SH on the THz field strength, and find that the amplitude of the q-FM mode again scales linearly with the $\mathbf{E}_{\mathrm{THz}}$. In contrast, the q-FM SH mode scales quadratically with the $\mathbf{E}_{\mathrm{THz}}$.

Similar nonlinearities have been reported previously in similar experiments, for instance in the ferromagnetic resonance of thin metallic films [178] and in other orthoferrites [166,179]. In the orthoferrites, this observation was attributed to the quadratic magnetorefractive effect due to the interaction of the spin system and the probe pulse [180], where the quadratic dependence of the detected rotation as a function of the amplitude of the deflection results in double frequency features in the spectrum.

6.8 Low Temperature SRT in $ErFeO_3$

The emergence of the antiferromagnetic ordering below the Néel temperature of 4 K in $ErFeO_3$ is associated with an additional phase transition. This phase transition is the $\Gamma_2 \rightarrow \Gamma_{12}$ phase transition, where the antiferromagnetic vector starts to rotate out of plane towards the b-axis [181]. We extended the above described measurements to the low temperatures below 4 K, and again performed the measurements for the different orientations of the sample. The results obtained with the THz magnetic field aligned along the c-axis are shown in figure 6.10.

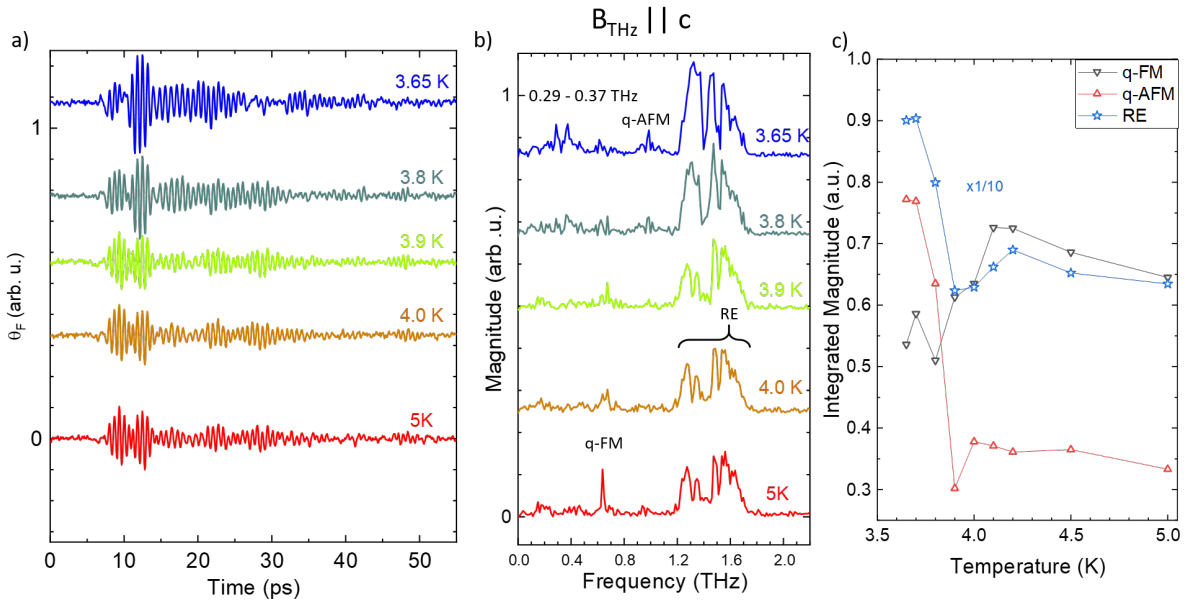

Figure 6.10: Low temperature measurements of THz induced spin dynamics in $ErFeO_3$ below the Néel temperature, with the THZ magnetic field aligned along the c-axis. a) Shows the signals in the time domain, b) shows the Fourier transforms, and c) the extracted amplitude of the three observed modes of AFMR.

The rare-earth modes are again pronounced around 1.3-1.5 THz when $\mathbf{B}_{THz}$||c. As the temperature is further decreased, we see a further increase in the amplitude of the rare-earth modes, particularly of the mode around 1.3 THz and the rare-earth mode structure becomes narrower and more resolved. Besides, we see that two features around 0.3 THz start to appear at 3.65 K. These frequencies match with the difference frequencies of the rare-earth modes, possibly indicating transitions between the more closely separated energy levels. This increased resolution in the rare-earth peak structure and the emergence of low-energy transitions is likely due to the increasing population of the ground state at low temperatures. Moreover, we see that upon decreasing temperature, the q-FM feature disappears and a q-AFM feature starts to emerge.

We repeated the measurements for the orthogonal sample orientation, such that the a-axis is aligned with $\mathbf{B}_{\mathrm{THz}}$. As the q-AFM mode was already visible in the Γ_2 phase, this allowed us to study the evolution of this mode in more detail. The results are shown in figure 6.11.

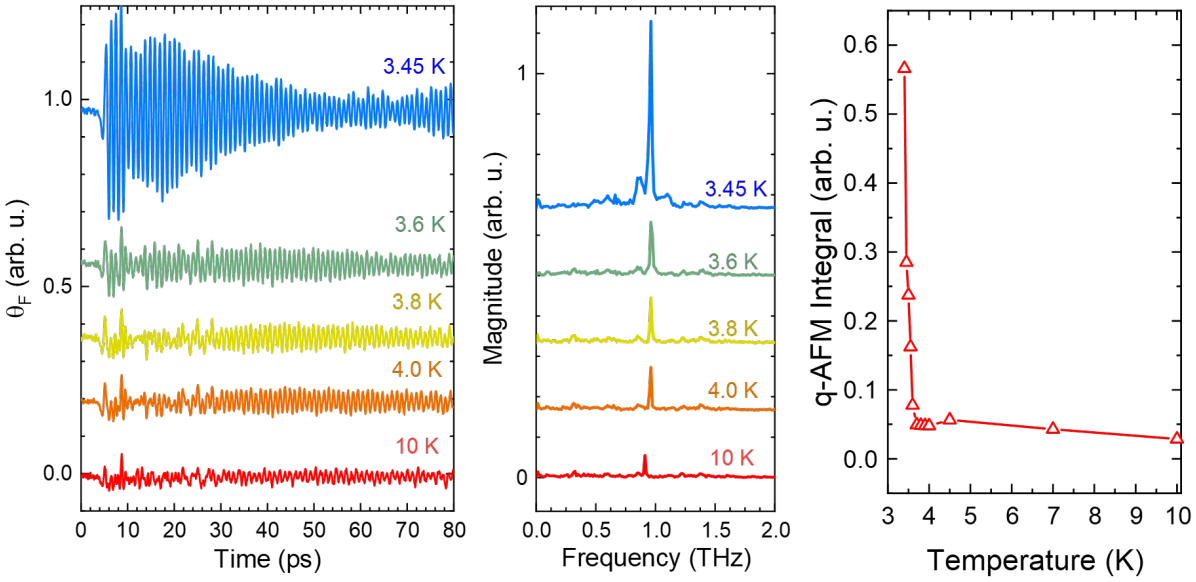

Figure 6.11: Low temperature measurements of THz induced spin dynamics in $ErFeO_3$ below the Néel temperature, with the THz magnetic field aligned along the a-axis. a) Shows the signals in the time domain, b) shows the Fourier transforms, and c) the extracted amplitude of the q-AFM mode.

In this experimental configuration, we see very clean oscillations at the q-AFM frequency, that increase rapidly in amplitude upon cooling down into the Γ_{12} phase. This observation is not trivial, as the weak ferromagnetic moment rotates away from the axis along which the THz magnetic field is aligned, thus reducing the torque that excites the q-AFM mode.

The mechanism through which this enhancement occurs must be different than the one that enhances the the q-FM mode in the Γ_{24} phase, as no efficient coupling between the rare-earth modes and the q-AFM mode is expected, due to the large gap in their frequencies.

The low-temperature enhancement in the Γ_{12} phase may be explained by the increase of the magnetic permeability in this phase. Such an orders of magnitude enhancement of the permeability has been previously reported in the Γ_{12} phase of $HoFeO_3$ [182].

6.9 Conclusions

In this chapter, we studied the spin dynamics in orthoferrites induced by intense THz pulses in the search for nonlinearities in the spin dynamics. Although nonlinear spin dynamics was not yet observed in contrast to the previous report [113], likely due to insufficiently high

peak amplitudes of the THz pulse, we observed a great enhancement of the q-FM mode in the middle of the SRT in $ErFeO_3$. $TmFeO_3$, in which the iron spin system has a very similar magnetic structure, did not reveal a similar behavior in the SRT. We attributed this difference to the effect of the rare-earth ions on the iron spins. From calculations, including a coupling between the rare-earth spin and the iron spins, we found that this d-f interaction acts as an additional torque on the iron spins, which is maximized exactly in the center of the SRT. We found that the symmetry of this torque matches the experimentally measured data very well.

Further improvements in our setup have shown some first signs of nonlinearities. We have observed the second harmonic of the q-FM modes in the Γ_2 phase. Moreover, we have achieved spin dynamics measurements at extremely low temperatures, below the ordering temperature of the rare-earth spins, which induces another SRT, bringing the iron spins in the Γ_{12} phase.

Recent further improvements to our experimental setup allowed us to achieve tighter focusing of the THz pulse, due to which the peak THz field can now exceed 1 MV/cm. As the electric field is estimated to be more than doubled, the experiments may be repeated to find nonlinear effects and drive the spin dynamics with even higher amplitudes.

Chapter 7

Summary and Outlook

7.1 Summary

In this thesis, we have investigated spin dynamics in antiferromagnetic oxides, the orthoferrites, which were recently proposed to be considered as altermagnets. The orthoferrites are of great interest due to their canted antiferromagnetic moments, providing high-frequency resonances characteristic for the antiferromagnets, while retaining a weak ferromagnetic moment and high magneto-optical responses. This makes them excellent candidates for high-speed, and all-optical, energy-efficient data storage and processing. Although magnons in ferromagnets have already been under intensive investigation, until recently, exciting and controlling nanoscale wavelength and THz frequency magnons has remained challenging.

The work and achievements presented in this thesis are summarized as follows:

- We have developed a theoretical formalism to understand how magnons in antiferromagnets can be generated by strongly absorbed light pulses, and how they can be detected by light pulses.
- We have performed ultrafast pump-probe spectroscopy to study the magnons experimentally in $HoFeO_3$.
- We have applied a novel 2D spectroscopy technique to study magnons, which has shown to allow for the conversion of the uniform precession mode into the propagating modes.
- We have designed and built a novel experimental terahertz pump - optical probe spectroscopy, allowing for the resonant excitation of the orthoferrites at cryogenic temperatures down to 3 K.

In the first part of the thesis, we have shown how the challenge of generating magnons in antiferromagnets can be overcome. Through the solution of the Klein-Gordon equation for antiferromagnetic spin dynamics, which can be derived from the Lagrangian formalism, we showed that one can exploit the strong absorption band in the insulating orthoferrites, to achieve nanoscale confinement of the spin excitations by optical stimuli. Consequently, spins in this region are quasi-uniformly excited by the effective field of the light pulse acting on the spins, and propagating packets of high-frequency spin waves with nanometer scale wavelengths are emitted from the region of excitation. In addition, we modeled the magneto-optical detection of such propagating spin waves and found that the spin waves act as a propagating diffraction grating for a probe light pulse, that results in the polarization rotation of the probe pulse. Through the emergence of the Brillouin/Bragg condition, this rotation is selectively enhanced for the right matching between the wave numbers of the probe pulse and the magnon, thus allowing for selective detection of the magnon. We found that our theory provides an excellent agreement with the first experiment that reported such spin waves in $DyFeO_3$ [70].

We then reported the observation of the propagating magnons in another orthoferrite, $HoFeO_3$, and addressed a second major challenge in THz magnonics. This challenge involves the demonstration of nonlinearities of magnons, that allow for the control of the properties of one magnon by another unit, which is essential for mimicking transistor-like operations using magnons instead of electric charge. More specifically, we have shown that we can achieve such nonlinear control in the canted antiferromagnets, through magnon-photon interactions. Our experiment using the double-pump probe spectroscopy technique, showed that the low-frequency quasi-uniform precession modes can be up-converted to higher frequency and higher wavenumber modes of a propagating wavepacket. This effect is proportional to the strength of the Dzyaloshinskii-Moriya Interaction, and can thus only be found in canted antiferromagnets, making the orthoferrite a suitable system for the investigation of this nonlinearity.

In the last part of this thesis, we returned to uniform $k = 0$ spin dynamics and searched for high amplitude spin dynamics in the orthoferrites $ErFeO_3$ and $TmFeO_3$ using intense THz pulses generated through optical rectification with tilted pulse fronts in $LiNbO_3$. The magnetic field component of these THz frequency pulses can couple directly and resonantly to the spins through magnetic dipole coupling, but previous reports [69] have also demonstrated resonant nonlinear pathways for the control of spins through the electric field in $TmFeO_3$.

We studied the spin dynamics at various temperatures and found the two different modes

of antiferromagnetic resonance, the q-FM and q-AFM mode, in both samples, depending on the temperature and sample orientation. In $ErFeO_3$, a giant increase in amplitude of the q-FM mode was observed upon crossing the Spin Reorientation Transition temperature region, with the maximum amplitude in the center. In contrast, in $TmFeO_3$ the amplitude of this mode decreased over this region, despite the fact that the macroscopic magnetic properties of the iron systems in these orthoferrites are nearly identical.

We attributed this discrepancy between these two materials to the effect of the rare-earth spins on the spin dynamics of the iron spin system. We confirmed our interpretation from a theoretical perspective, by calculating the torque on the iron spins as a consequence of their interaction with the rare-earth ions, and found that this torque is maximized in the center of the Spin Reorientation Transition.

In spite of the large amplitude of the q-FM mode in $ErFeO_3$, we observed a linear dependence on the THz field. Our proposed model for the enhancement is in agreement with the observed linear dependence.

Owing to the capabilities of our experimental setup, we have also been able to observe another phase transition in $ErFeO_3$ at low temperatures below the Néel temperature of 4 K where the rare-earth sublattice starts to order antiferromagnetically. In this phase transition, we observed a large enhancement of the q-AFM mode, which we attributed to the increase of magnetic susceptibility in this phase.

Moreover, we observed second harmonics in $ErFeO_3$, which is a signature of nonlinear spin dynamics. We found that the modes at double the frequency of the q-FM mode scale quadratically with the THz field amplitude.

7.2 Outlook

This section will provide an outlook for potential further continuation of the research presented in this thesis. We have seen that the generation of the spin waves in the antiferromagnets requires a strong nanoscale confinement of the pump. In the work presented here, this was achieved with strongly absorbed light pulses, which provide a substantial risk of damaging the samples. Therefore, we may search for other sources on confinement. For instance, by using micro-objectives, tight focusing of optical excitations may be achieved. Besides, as the spin waves in this thesis propagate into the material, they are only indirectly detectable through the Brillouin condition. Combining the confined pulses with nanometer scale focused pulses allows the spin waves to propagate along the surface. The propagation of such surface spin waves can be more directly monitored with time-resolved imaging

techniques.

Further studies on the nonlinear conversion mechanism may also be performed. Although we have investigated the dependence of the nonlinear conversion on many parameters, we have not studied the dependence on the pump wavelength dependence of the individual pumps. For instance, we may investigate whether the confinement of the first pump pulse is relevant. This can be done by using pulses in the transparency region, for instance using 800 nm pulses. This excites the quasi-uniform precession throughout the thickness of the sample, and we can investigate how the spin waves excited by the second pump propagate and are modulated as a function of the time delay.

Although we have seen in Chapter 6 that the THz field drives strongly enhanced spin dynamics in the Spin Reorientation Transition by resonantly pumping transition in the rare-earth system, we still observe that the amplitude scales linearly with the THz magnetic field, in contrast with previous reported measurements on $TmFeO_3$. The origin of this discrepancy requires further study. For instance, the crystal-cut may be relevant for the observation of the nonlinear effect, and thus crystals of different cuts. Moreover, further improvements to the THz pulses may be made, for instance by cooling the $LiNbO_3$ in a cryostat. This may result in higher peak amplitudes and broader spectra, where the high frequencies may be relevant for the excitations of the nonlinearities.

7.3 THz pumping of metallic thin films

Although the work presented in this thesis was devoted to the study of the antiferromagnetic oxides, which are insulators, here we will demonstrate that our intense THz setup is also suitable for the study of metals. To this end, some recent measurements on thin FeRh metallic films will be highlighted in this section. FeRh is an interesting material, as it is an antiferromagnet at room temperature, but undergoes a phase transition to the ferromagnetic phase at 370 K upon heating, which is accompanied by an expansion of the crystallographic lattice [183]. This phase transition shows hysteresis, and the material returns to the ferromagnetic state at 340 K upon cooling [184].

Many studies to date have utilized the optical pump to drive the spin dynamics, and have been shown to drive demagnetization in the ferromagnetic phase [185], or induce magnetization in the antiferromagnetic phase [186].

In our experiments, we explored how the intense THz pulses interact in this material in both the high-temperature ferromagnetic phase, and the room temperature antiferromagnetic phase.

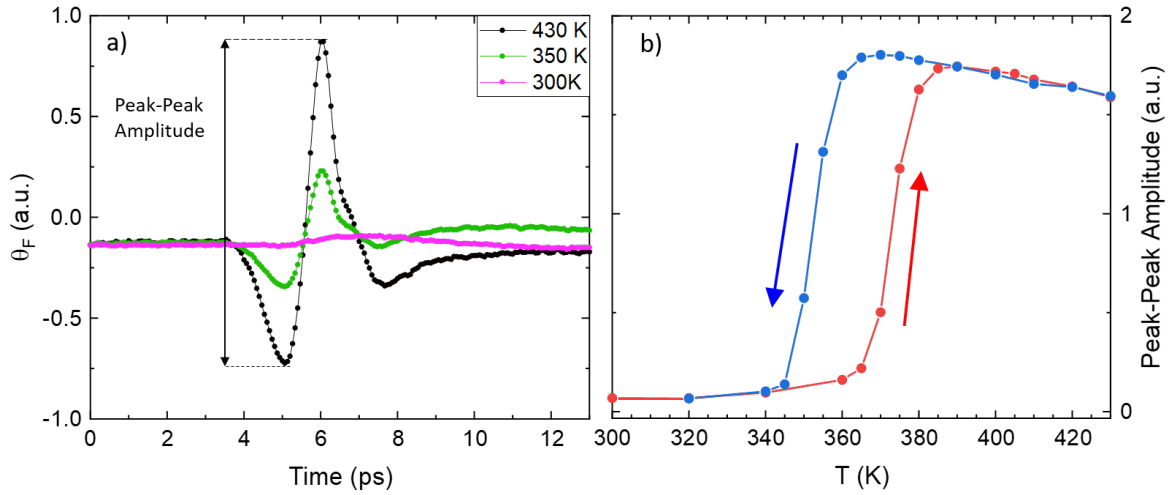

Figure 7.1: a) Short range THz-induced spin dynamics in FeRh at various temperatures (upon cooling). b) Temperature hysteresis curve for the cooling (blue) and heating (red) cycles, extracted from the peak values in a).

We mounted the sample on a heater, and applied a vertical external magnetic field, such that the horizontal magnetic field component of the THz pulse applies a torque on the magnetization. This torque will be proportional to the length of the magnetization vector, allowing is to monitor the phase transition with THz pulses, as shown in figure 7.1.

We see that the dynamics of the magnetization in the ferromagnetic phase closely follows the shape of the THz pulse, thus indicating the direct Zeeman torque coupling of the THz pulse to the spins.

Moreover, we observe a small step in the negative and positive time delays, which can be an indication of demagnetization of the ferromagnetic domains, or nucleation of extra ferromagnetic domains, or this can be a sign of low frequency oscillations of the ferromagnetic moment. We therefore investigated the dynamics at long time delays in two different configurations. The configuration with the external magnetic field applied in plane allows us to detect the oscillations of the ferromagnetic vector. To increase our experimental sensitivity to the changes in the length of the ferromagnetic vector, corresponding to demagnetization or induction of magnetization, we applied the magnetic field out of plane.

The temperature dependence of the long range dynamics is shown in figure 7.2.

In these measurements, we started in the high temperature ferromagnetic phase, and cooled down the sample. When the magnetic field is applied in plane, we can observe clear low frequency oscillations, at a frequency of about 14 GHz, which matches well with the frequency of ferromagnetic resonance that can be expected with our applied external magnetic field [187]. We see that during the phase transition, the oscillations disappear, and

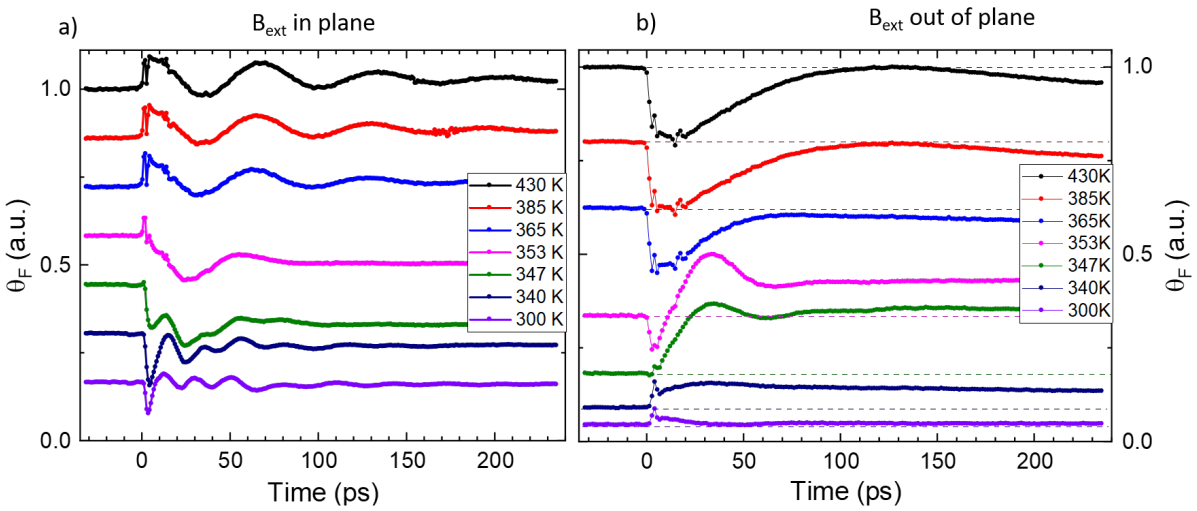

Figure 7.2: a) Measured long range spin dynamics in FeRh at various temperatures with the external magnetic field applied in plane. b) Measured long range spin dynamics in FeRh at various temperatures with the magnetic field applied out of plane.

upon cooling into the antiferromagnetic phase, higher frequency oscillations appear with a frequency of about 50 GHz. Such room temperature oscillations were not observed before, and the origin of these oscillations is not yet known.

When the field is applied out of plane, we clearly see that at in the high temperature ferromagnetic phase, the Faraday rotation signal temporarily decreases strongly before relaxing back to the initial state, indicating the demagnetization. As the temperature is decreased, the step in the signal changes sign, thus implying that the ferromagnetic order can be enhanced by the use of THz pulses.

Thus, this section has shown that the intense THz pulses are not only a suitable tool for control of magnetization in insulating antiferromagnetic oxides, but can also be utilized for the control and study of metallic films.

References

[1] Y. Yamamoto, *Pull Of History: The Human Understanding Of Magnetism And Gravity Through The Ages*. World Scientific, 2017.

[2] S. Blundell, "Quantum magnetism," in *Magnetism: A Very Short Introduction*, Oxford University Press, 06 2012.

[3] L. Šmejkal, J. Sinova, and T. Jungwirth, "Emerging research landscape of altermagnetism," *Physical Review X*, vol. 12, no. 4, p. 040501, 2022.

[4] I. Mazin *et al.*, "Altermagnetism—a new punch line of fundamental magnetism," *Physical Review X*, vol. 12, no. 4, p. 040002, 2022.

[5] A. Kimel, A. Zvezdin, *et al.*, "Universal orthoferrites and orthoferrites as a universe," *Photonics Insights*, vol. 1, no. 2, pp. C03–C03, 2023.

[6] E. Spain and A. Venkatanarayanan, "13.02 - review of physical principles of sensing and types of sensing materials," in *Comprehensive Materials Processing* (S. Hashmi, G. F. Batalha, C. J. Van Tyne, and B. Yilbas, eds.), pp. 5–46, Oxford: Elsevier, 2014.

[7] M. Dayarathna, Y. Wen, and R. Fan, "Data center energy consumption modeling: A survey," *IEEE Communications Surveys & Tutorials*, vol. 18, no. 1, pp. 732–794, 2016.

[8] J. Koomey *et al.*, "Growth in data center electricity use 2005 to 2010," *A report by Analytical Press, completed at the request of The New York Times*, vol. 9, no. 2011, p. 161, 2011.

[9] K. M. U. Ahmed, M. H. Bollen, and M. Alvarez, "A review of data centers energy consumption and reliability modeling," *IEEE Access*, vol. 9, pp. 152536–152563, 2021.

[10] J. Judge, J. Pouchet, A. Ekbote, and S. Dixit, "Reducing data center energy consumption," *Ashrae Journal*, vol. 50, no. 11, p. 14, 2008.

[11] D. Burg and J. H. Ausubel, "Moore's Law revisited through Intel chip density," *PloS one*, vol. 16, no. 8, p. e0256245, 2021.

[12] R. Schaller, "Moore's law: past, present and future," *IEEE Spectrum*, vol. 34, no. 6, pp. 52–59, 1997.

[13] P. Ball, "Semiconductor technology looks up," *Nature Materials*, vol. 21, no. 2, pp. 132–132, 2022.

[14] J. Cho and K. E. Goodson, "Cool electronics," *Nature Materials*, vol. 14, no. 2, pp. 136–137, 2015.

[15] I. Žutić, J. Fabian, and S. D. Sarma, "Spintronics: Fundamentals and applications," *Reviews of modern physics*, vol. 76, no. 2, p. 323, 2004.

[16] A. Chumak, A. Serga, and B. Hillebrands, "Magnonic crystals for data processing," *Journal of Physics D: Applied Physics*, vol. 50, no. 24, p. 244001, 2017.

[17] W. Sibbett, A. Lagatsky, and C. Brown, "The development and application of femtosecond laser systems," *Optics Express*, vol. 20, no. 7, pp. 6989–7001, 2012.

[18] J. Lloyd-Hughes, P. M. Oppeneer, T. P. Dos Santos, A. Schleife, S. Meng, M. A. Sentef, M. Ruggenthaler, A. Rubio, I. Radu, M. Murnane, *et al.*, "The 2021 ultrafast spectroscopic probes of condensed matter roadmap," *Journal of Physics: Condensed Matter*, vol. 33, no. 35, p. 353001, 2021.

[19] M. Dąbrowski, S. Guo, M. Strungaru, P. S. Keatley, F. Withers, E. J. Santos, and R. J. Hicken, "All-optical control of spin in a 2D van der Waals magnet," *Nature Communications*, vol. 13, no. 1, p. 5976, 2022.

[20] C. Shank and E. Ippen, "Subpicosecond kilowatt pulses from a mode-locked cw dye laser," *Applied Physics Letters*, vol. 24, no. 8, pp. 373–375, 1974.

[21] E. Beaurepaire, J.-C. Merle, A. Daunois, and J.-Y. Bigot, "Ultrafast Spin Dynamics in Ferromagnetic Nickel," *Physical Review Letters*, vol. 76, pp. 4250–4253, May 1996.

[22] A. Kirilyuk, A. V. Kimel, and T. Rasing, "Ultrafast optical manipulation of magnetic order," *Reviews of Modern Physics*, vol. 82, no. 3, p. 2731, 2010.

[23] M. van Kampen, C. Jozsa, J. T. Kohlhepp, P. LeClair, L. Lagae, W. J. M. de Jonge, and B. Koopmans, "All-Optical Probe of Coherent Spin Waves," *Physical Review Letters*, vol. 88, no. 22, p. 227201, 2002.

[24] A. V. Kimel, A. Kirilyuk, A. Tsvetkov, R. V. Pisarev, and T. Rasing, "Laser-induced ultrafast spin reorientation in the antiferromagnet $TmFeO_3$," *Nature*, vol. 429, no. 6994, pp. 850–853, 2004.

[25] J.-U. Thiele, M. Buess, and C. H. Back, "Spin dynamics of the antiferromagnetic-to-ferromagnetic phase transition in FeRh on a sub-picosecond time scale," *Applied Physics Letters*, vol. 85, no. 14, pp. 2857–2859, 2004.

[26] M. O. Ellis, E. E. Fullerton, and R. W. Chantrell, "All-optical switching in granular ferromagnets caused by magnetic circular dichroism," *Scientific reports*, vol. 6, no. 1, pp. 1–9, 2016.

[27] T. Ostler, J. Barker, R. Evans, R. Chantrell, U. Atxitia, O. Chubykalo-Fesenko, S. El Moussaoui, L. Le Guyader, E. Mengotti, L. Heyderman, *et al.*, "Ultrafast heating as a sufficient stimulus for magnetization reversal in a ferrimagnet," *Nature Communications*, vol. 3, no. 1, p. 666, 2012.

[28] C. Davies, J. Janušonis, A. Kimel, A. Kirilyuk, A. Tsukamoto, T. Rasing, and R. Tobey, "Towards massively parallelized all-optical magnetic recording," *Journal of Applied Physics*, vol. 123, no. 21, p. 213904, 2018.

[29] B. Ivanov, "Spin dynamics for antiferromagnets and ultrafast spintronics," *Journal of Experimental and Theoretical Physics*, vol. 131, pp. 95–112, 2020.

[30] I. Fina and X. Marti, "Electric control of antiferromagnets," *IEEE Transactions on Magnetics*, vol. 53, no. 2, pp. 1–7, 2016.

[31] A. Kimel, A. Kalashnikova, A. Pogrebna, and A. Zvezdin, "Fundamentals and perspectives of ultrafast photoferroic recording," *Physics Reports*, vol. 852, pp. 1–46, 2020.

[32] P. Wadley, B. Howells, J. Železnỳ, C. Andrews, V. Hills, R. P. Campion, V. Novák, K. Olejník, F. Maccherozzi, S. Dhesi, *et al.*, "Electrical switching of an antiferromagnet," *Science*, vol. 351, no. 6273, pp. 587–590, 2016.

[33] K. Olejník, T. Seifert, Z. Kašpar, V. Novák, P. Wadley, R. P. Campion, M. Baumgartner, P. Gambardella, P. Němec, J. Wunderlich, *et al.*, "Terahertz electrical writing speed in an antiferromagnetic memory," *Science advances*, vol. 4, no. 3, p. eaar3566, 2018.

[34] S. Y. Bodnar, L. Šmejkal, I. Turek, T. Jungwirth, O. Gomonay, J. Sinova, A. Sapozhnik, H.-J. Elmers, M. Kläui, and M. Jourdan, "Writing and reading antiferromagnetic Mn_2Au

by Néel spin-orbit torques and large anisotropic magnetoresistance," *Nature Communications*, vol. 9, no. 1, p. 348, 2018.

[35] A. V. Kimel, C. D. Stanciu, P. A. Usachev, R. V. Pisarev, V. N. Gridnev, A. Kirilyuk, and T. Rasing, "Optical excitation of antiferromagnetic resonance in $TmFeO_3$," *Physical Review B*, vol. 74, no. 6, 2006.

[36] J. A. de Jong, A. V. Kimel, R. V. Pisarev, A. Kirilyuk, and T. Rasing, "Laser-induced ultrafast spin dynamics in $ErFeO_3$," *Physical Review B*, vol. 84, no. 10, 2011.

[37] J. Hohlfeld, T. Gerrits, M. Bilderbeek, T. Rasing, H. Awano, and N. Ohta, "Fast magnetization reversal of gdfeco induced by femtosecond laser pulses," *Physical Review B*, vol. 65, no. 1, p. 012413, 2001.

[38] C. Vicario, C. Ruchert, F. Ardana-Lamas, P. M. Derlet, B. Tudu, J. Luning, and C. P. Hauri, "Off-resonant magnetization dynamics phase-locked to an intense phase-stable terahertz transient," *Nature Photonics*, vol. 7, no. 9, pp. 720–723, 2013.

[39] A. Kimel, A. Kirilyuk, P. Usachev, R. Pisarev, A. Balbashov, and T. Rasing, "Ultrafast non-thermal control of magnetization by instantaneous photomagnetic pulses," *Nature*, vol. 435, no. 7042, pp. 655–657, 2005.

[40] A. M. Kalashnikova, A. V. Kimel, R. V. Pisarev, V. N. Gridnev, A. Kirilyuk, and T. Rasing, "Impulsive generation of coherent magnons by linearly polarized light in the easy-plane antiferromagnet $FeBO_3$," *Physical Review Letters*, vol. 99, no. 16, 2007.

[41] A. M. Kalashnikova, A. V. Kimel, R. V. Pisarev, V. N. Gridnev, P. A. Usachev, A. Kirilyuk, and T. Rasing, "Impulsive excitation of coherent magnons and phonons by subpicosecond laser pulses in the weak ferromagnet $FeBO_3$," *Physical Review B*, vol. 78, no. 10, 2008.

[42] A. K. Zvezdin and V. A. Kotov, *Modern magnetooptics and magnetooptical materials*. CRC Press, 1997.

[43] P. Pershan, "Nonlinear optical properties of solids: energy considerations," *Physical Review*, vol. 130, no. 3, p. 919, 1963.

[44] M. Fox, *Optical properties of solids*. Oxford University Press, 2010.

[45] J. Van der Ziel, P. S. Pershan, and L. Malmstrom, "Optically-induced magnetization resulting from the inverse Faraday effect," *Physical Review Letters*, vol. 15, no. 5, p. 190, 1965.

[46] F. Pedrotti and L. Pedrotti, *Introduction to Optics*. Prentice Hall international editions, Prentice Hall, 1993.

[47] R. Mikhaylovskiy, E. Hendry, and V. Kruglyak, "Ultrafast inverse Faraday effect in a paramagnetic terbium gallium garnet crystal," *Physical Review B*, vol. 86, no. 10, p. 100405, 2012.

[48] E. Schmoranzerová, T. Ostatnickỳ, J. Kimák, D. Kriegner, H. Reichlová, R. Schlitz, A. Baďura, Z. Šobáň, M. Münzenberg, G. Jakob, *et al.*, "Giant quadratic magneto-optical response of thin $Y_3Fe_5O_{12}$ films for sensitive magnetometry experiments," *Physical Review B*, vol. 106, no. 10, p. 104434, 2022.

[49] C. Rizzo, A. Rizzo, and D. M. Bishop, "The Cotton-Mouton effect in gases: experiment and theory," *International Reviews in Physical Chemistry*, vol. 16, no. 1, pp. 81–111, 1997.

[50] G. Y. Guseynov, R. Levitin, K. Mukimov, V. Nekvasil, A. Popov, N. Vedernikov, and A. Zvezdin, "Magnetic linear birefringence in paramagnetic rare-earth garnets YbAG, YbGG, and GdGG in high magnetic fields and at low temperatures," *Czechoslovak Journal of Physics B*, vol. 37, pp. 98–107, 1987.

[51] A. M. Kalashnikova, A. V. Kimel, and R. V. Pisarev, "Ultrafast opto-magnetism," *Physics-Uspekhi*, vol. 58, no. 10, p. 969, 2015.

[52] G. Deng, P. Guo, W. Ren, S. Cao, H. E. Maynard-Casely, M. Avdeev, and G. J. McIntyre, "The magnetic structures and transitions of a potential multiferroic orthoferrite $ErFeO_3$," *Journal of Applied Physics*, vol. 117, no. 16, p. 164105, 2015.

[53] X. Li, D. Kim, Y. Liu, and J. Kono, "Terahertz spin dynamics in rare-earth orthoferrites," *Photonics Insights*, vol. 1, no. 2, pp. R05–R05, 2023.

[54] T. Yamaguchi, "Theory of spin reorientation in rare-earth orthochromites and orthoferrites," *Journal of Physics and Chemistry of Solids*, vol. 35, no. 4, pp. 479–500, 1974.

[55] A. Balbashov, G. Kozlov, A. Mukhin, and A. Prokhorov, "Submillimeter spectroscopy of antiferromagnetic dielectrics. Rare-earth orthoferrites," *High Frequency Processes in Magnetic Materials*, vol. 56, 1995.

[56] A. Moskvin, "Dzyaloshinskii interaction and exchange-relativistic effects in orthoferrites," *Journal of Experimental and Theoretical Physics*, vol. 132, pp. 517–547, 2021.

[57] K. Momma and F. Izumi, "Vesta: a three-dimensional visualization system for electronic and structural analysis," *Journal of Applied crystallography*, vol. 41, no. 3, pp. 653–658, 2008.

[58] D. Wood, L. Holmes, and J. Remeika, "Exchange fields and optical zeeman effect in $ErFeO_3$," *Physical Review*, vol. 185, no. 2, p. 689, 1969.

[59] I. Dzyaloshinsky, "A thermodynamic theory of "weak" ferromagnetism of antiferromagnetics," *Journal of physics and chemistry of solids*, vol. 4, no. 4, pp. 241–255, 1958.

[60] T. Moriya, "Anisotropic superexchange interaction and weak ferromagnetism," *Physical Review*, vol. 120, no. 1, p. 91, 1960.

[61] S. Li, X. Wang, and T. Rasing, "Magnetic skyrmions: Basic properties and potential applications," *Interdisciplinary Materials*, vol. 2, no. 2, pp. 260–289, 2023.

[62] M. Johnson, P. Bloemen, F. Den Broeder, and J. De Vries, "Magnetic anisotropy in metallic multilayers," *Reports on Progress in Physics*, vol. 59, no. 11, p. 1409, 1996.

[63] H. Kirchmayr, *Magnetic anisotropy*. 2001.

[64] R. V. Mikhaylovskiy, E. Hendry, A. Secchi, J. H. Mentink, M. Eckstein, A. Wu, R. V. Pisarev, V. V. Kruglyak, M. I. Katsnelson, T. Rasing, and A. V. Kimel, "Ultrafast optical modification of exchange interactions in iron oxides," *Nature Communications*, vol. 6, p. 8190, 2015.

[65] C. Wynn, M. Girtu, W. Brinckerhoff, K.-I. Sugiura, J. S. Miller, and A. Epstein, "Magnetic dipole- dipole interactions and single-ion anisotropy: revisiting a classical approach to magnets," *Chemistry of materials*, vol. 9, no. 10, pp. 2156–2163, 1997.

[66] A. Zvezdin, "Dynamics of domain walls in weak ferromagnets," *ZhETF Pisma Redaktsiiu*, vol. 29, p. 605, 1979.

[67] L. Landau and E. Lifshitz, "On the theory of the dispersion of magnetic permeability in ferromagnetic bodies," in *Perspectives in Theoretical Physics*, pp. 51–65, Elsevier, 1992.

[68] T. Gilbert, "A phenomenological theory of damping in ferromagnetic materials," *IEEE Transactions on Magnetics*, vol. 40, no. 6, pp. 3443–3449, 2004.

[69] S. Baierl, J. H. Mentink, M. Hohenleutner, L. Braun, T.-M. Do, C. Lange, A. Sell, M. Fiebig, G. Woltersdorf, T. Kampfrath, *et al.*, "Terahertz-driven nonlinear spin response of

antiferromagnetic nickel oxide," *Physical Review Letters*, vol. 117, no. 19, p. 197201, 2016.

[70] J. R. Hortensius, D. Afanasiev, M. Matthiesen, R. Leenders, R. Citro, A. V. Kimel, R. V. Mikhaylovskiy, B. A. Ivanov, and A. D. Caviglia, "Coherent spin-wave transport in an antiferromagnet," *Nature Physics*, vol. 17, no. 9, pp. 1001–1006, 2021.

[71] E. Mashkovich, K. Grishunin, R. Mikhaylovskiy, A. Zvezdin, R. Pisarev, M. Strugatsky, P. Christianen, T. Rasing, and A. Kimel, "Terahertz optomagnetism: nonlinear THz excitation of GHz spin waves in antiferromagnetic $FeBO_3$," *Physical Review Letters*, vol. 123, no. 15, p. 157202, 2019.

[72] J. Wang, H. Duan, X. Lin, V. Aguilar, A. Mosqueda, and G.-m. Zhao, "Temperature dependence of magnetic anisotropy constant in iron chalcogenide Fe_3Se_4: Excellent agreement with theories," *Journal of Applied Physics*, vol. 112, no. 10, p. 103905, 2012.

[73] K. O'Grady, J. Sinclair, K. Elphick, R. Carpenter, G. Vallejo-Fernandez, M. Probert, and A. Hirohata, "Anisotropy in antiferromagnets," *Journal of Applied Physics*, vol. 128, no. 4, p. 040901, 2020.

[74] F. Bloch, "Zur theorie des ferromagnetismus," *Zeitschrift für Physik*, vol. 61, no. 3-4, pp. 206–219, 1930.

[75] G. Venkat, D. Kumar, M. Franchin, O. Dmytriiev, M. Mruczkiewicz, H. Fangohr, A. Barman, M. Krawczyk, and A. Prabhakar, "Proposal for a standard micromagnetic problem: Spin wave dispersion in a magnonic waveguide," *IEEE Transactions on Magnetics*, vol. 49, no. 1, pp. 524–529, 2012.

[76] V. Kruglyak, S. Demokritov, and D. Grundler, "Magnonics," *Journal of Physics D: Applied Physics*, vol. 43, no. 26, p. 264001, 2010.

[77] A. Serga, A. Chumak, and B. Hillebrands, "Yig magnonics," *Journal of Physics D: Applied Physics*, vol. 43, no. 26, p. 264002, 2010.

[78] A. V. Chumak, V. I. Vasyuchka, A. A. Serga, and B. Hillebrands, "Magnon spintronics," *Nature Physics*, vol. 11, no. 6, pp. 453–461, 2015.

[79] A. Barman, G. Gubbiotti, S. Ladak, A. O. Adeyeye, M. Krawczyk, J. Grafe, C. Adelmann, S. Cotofana, A. Naeemi, V. I. Vasyuchka, B. Hillebrands, S. A. Nikitov, H. Yu, D. Grundler, A. V. Sadovnikov, A. A. Grachev, S. E. Sheshukova, J. Y. Duquesne, M. Marangolo,

G. Csaba, W. Porod, V. E. Demidov, S. Urazhdin, S. O. Demokritov, E. Albisetti, D. Petti, R. Bertacco, H. Schultheiss, V. V. Kruglyak, V. D. Poimanov, S. Sahoo, J. Sinha, H. Yang, M. Munzenburg, T. Moriyama, S. Mizukami, P. Landeros, R. A. Gallardo, G. Carlotti, J. V. Kim, R. L. Stamps, R. E. Camley, B. Rana, Y. Otani, W. Yu, T. Yu, G. E. W. Bauer, C. Back, G. S. Uhrig, O. V. Dobrovolskiy, B. Budinska, H. Qin, S. van Dijken, A. V. Chumak, A. Khitun, D. E. Nikonov, I. A. Young, B. W. Zingsem, and M. Winklhofer, "The 2021 Magnonics Roadmap," *Journal of Physics-Condensed Matter*, vol. 33, no. 41, p. 413001, 2021.

[80] P. Pirro, V. I. Vasyuchka, A. A. Serga, and B. Hillebrands, "Advances in coherent magnonics," *Nature Reviews Materials*, vol. 6, no. 12, pp. 1114–1135, 2021.

[81] T. Satoh, Y. Terui, R. Moriya, B. A. Ivanov, K. Ando, E. Saitoh, T. Shimura, and K. Kuroda, "Directional control of spin-wave emission by spatially shaped light," *Nature Photonics*, vol. 6, no. 10, pp. 662–666, 2012.

[82] Y. Au, M. Dvornik, T. Davison, E. Ahmad, P. S. Keatley, A. Vansteenkiste, B. Van Waeyenberge, and V. V. Kruglyak, "Direct excitation of propagating spin waves by focused ultrashort optical pulses," *Physical Review Letters*, vol. 110, no. 9, 2013.

[83] A. A. Kolosvetov, M. A. Kozhaev, I. V. Savochkin, V. I. Belotelov, and A. I. Chernov, "Concept of the Optomagnonic Logic Operation," *Physical Review Applied*, vol. 18, no. 5, p. 054038, 2022.

[84] I. Bertelli, J. J. Carmiggelt, T. Yu, B. G. Simon, C. C. Pothoven, G. E. Bauer, Y. M. Blanter, J. Aarts, and T. Van Der Sar, "Magnetic resonance imaging of spin-wave transport and interference in a magnetic insulator," *Science advances*, vol. 6, no. 46, p. eabd3556, 2020.

[85] N. E. Khokhlov, P. I. Gerevenkov, L. A. Shelukhin, A. V. Azovtsev, N. A. Pertsev, M. Wang, A. W. Rushforth, A. V. Scherbakov, and A. M. Kalashnikova, "Optical excitation of propagating magnetostatic waves in an epitaxial galfenol film by ultrafast magnetic anisotropy change," *Physical Review Applied*, vol. 12, no. 4, p. 044044, 2019.

[86] T. Schneider, A. A. Serga, B. Leven, B. Hillebrands, R. L. Stamps, and M. P. Kostylev, "Realization of spin-wave logic gates," *Applied Physics Letters*, vol. 92, no. 2, p. 022505, 2008.

[87] C. S. Davies and V. Kruglyak, "Graded-index magnonics," *Low Temperature Physics*, vol. 41, no. 10, pp. 760–766, 2015.

[88] N. Whitehead, S. Horsley, T. Philbin, and V. Kruglyak, "A luneburg lens for spin waves," *Applied Physics Letters*, vol. 113, no. 21, p. 212404, 2018.

[89] J. Jorzick, S. Demokritov, B. Hillebrands, M. Bailleul, C. Fermon, K. Y. Guslienko, A. Slavin, D. Berkov, and N. Gorn, "Spin wave wells in nonellipsoidal micrometer size magnetic elements," *Physical Review Letters*, vol. 88, no. 4, p. 047204, 2002.

[90] C. Davies, A. Francis, A. Sadovnikov, S. Chertopalov, M. Bryan, S. Grishin, D. Allwood, Y. P. Sharaevskii, S. Nikitov, and V. Kruglyak, "Towards graded-index magnonics: Steering spin waves in magnonic networks," *Physical Review B*, vol. 92, no. 2, p. 020408, 2015.

[91] A. Khitun, "Multi-frequency magnonic logic circuits for parallel data processing," *Journal of Applied Physics*, vol. 111, no. 5, p. 054307, 2012.

[92] R. V. Mikhaylovskiy, E. Hendry, and V. V. Kruglyak, "Negative permeability due to exchange spin-wave resonances in thin magnetic films with surface pinning," *Physical Review B*, vol. 82, no. 19, 2010.

[93] I. Razdolski, A. Alekhin, N. Ilin, J. P. Meyburg, V. Roddatis, D. Diesing, U. Bovensiepen, and A. Melnikov, "Nanoscale interface confinement of ultrafast spin transfer torque driving non-uniform spin dynamics," *Nature Communications*, vol. 8, pp. 1–5, 2017.

[94] P. Nemec, M. Fiebig, T. Kampfrath, and A. V. Kimel, "Antiferromagnetic opto-spintronics," *Nature Physics*, vol. 14, no. 3, pp. 229–241, 2018.

[95] S.-H. Yang, K.-S. Ryu, and S. Parkin, "Domain-wall velocities of up to 750 m s- 1 driven by exchange-coupling torque in synthetic antiferromagnets," *Nature nanotechnology*, vol. 10, no. 3, pp. 221–226, 2015.

[96] K. Grishunin, T. Huisman, G. Q. Li, E. Mishina, T. Rasing, A. V. Kimel, K. L. Zhang, Z. M. Jin, S. X. Cao, W. Ren, G. H. Ma, and R. V. Mikhaylovskiy, "Terahertz Magnon-Polaritons in $TmFeO_3$," *Acs Photonics*, vol. 5, no. 4, pp. 1375–1380, 2018.

[97] K. Kato, T. Yokoyama, and H. Ishihara, "Functionalized high-speed magnon polaritons resulting from magnonic antenna effect," *Physical Review Applied*, vol. 19, no. 3, p. 034035, 2023.

[98] A. Amo, T. Liew, C. Adrados, R. Houdré, E. Giacobino, A. Kavokin, and A. Bramati, "Exciton–polariton spin switches," *Nature Photonics*, vol. 4, no. 6, pp. 361–366, 2010.

[99] S. Das, A. Ross, X. X. Ma, S. Becker, C. Schmitt, F. Van Duijn, E. F. Galindez-Ruales, F. Fuhrmann, M. A. Syskaki, U. Ebels, V. Baltz, A. L. Barra, H. Y. Chen, G. Jakob, S. X. Cao, J. Sinova, O. Gomonay, R. Lebrun, and M. Kläui, "Anisotropic long-range spin transport in canted antiferromagnetic orthoferrite $YFeO_3$," *Nature Communications*, vol. 13, no. 1, p. 6140, 2022.

[100] R. Lebrun, A. Ross, S. A. Bender, A. Qaiumzadeh, L. Baldrati, J. Cramer, A. Brataas, R. A. Duine, and M. Kläui, "Tunable long-distance spin transport in a crystalline antiferromagnetic iron oxide," *Nature*, vol. 561, no. 7722, pp. 222–225, 2018.

[101] R. Lebrun, A. Ross, O. Gomonay, V. Baltz, U. Ebels, A. L. Barra, A. Qaiumzadeh, A. Brataas, J. Sinova, and M. Kläui, "Long-distance spin-transport across the morin phase transition up to room temperature in ultra-low damping single crystals of the antiferromagnet α-Fe_2O_3," *Nature Communications*, vol. 11, no. 1, p. 6332, 2020.

[102] M. Dąbrowski, T. Nakano, D. M. Burn, A. Frisk, D. G. Newman, C. Klewe, Q. Li, M. Yang, P. Shafer, E. Arenholz, T. Hesjedal, G. Van Der Laan, Z. Q. Qiu, and R. J. Hicken, "Coherent Transfer of Spin Angular Momentum by Evanescent Spin Waves within Antiferromagnetic NiO," *Physical Review Letters*, vol. 124, no. 21, p. 217201, 2020.

[103] K. Yamaguchi, M. Nakajima, and T. Suemoto, "Coherent control of spin precession motion with impulsive magnetic fields of half-cycle terahertz radiation," *Physical Review Letters*, vol. 105, no. 23, p. 237201, 2010.

[104] T. Kampfrath, A. Sell, G. Klatt, A. Pashkin, S. Mährlein, T. Dekorsy, M. Wolf, M. Fiebig, A. Leitenstorfer, and R. Huber, "Coherent terahertz control of antiferromagnetic spin waves," *Nature Photonics*, vol. 5, no. 1, pp. 31–34, 2011.

[105] T. Kampfrath, K. Tanaka, and K. A. Nelson, "Resonant and nonresonant control over matter and light by intense terahertz transients," *Nature Photonics*, vol. 7, no. 9, pp. 680–690, 2013.

[106] D. Afanasiev, J. Hortensius, B. Ivanov, A. Sasani, E. Bousquet, Y. Blanter, R. Mikhaylovskiy, A. Kimel, and A. Caviglia, "Ultrafast control of magnetic interactions via light-driven phonons," *Nature Materials*, vol. 20, no. 5, pp. 607–611, 2021.

[107] E. A. Mashkovich, K. A. Grishunin, R. M. Dubrovin, A. K. Zvezdin, R. V. Pisarev, and A. V. Kimel, "Terahertz light–driven coupling of antiferromagnetic spins to lattice," *Science*, vol. 374, no. 6575, pp. 1608–1611, 2021.

[108] A. Disa, J. Curtis, M. Fechner, A. Liu, A. von Hoegen, M. Först, T. Nova, P. Narang, A. Maljuk, A. Boris, *et al.*, "Photo-induced high-temperature ferromagnetism in $YTiO_3$," *Nature*, vol. 617, no. 7959, pp. 73–78, 2023.

[109] A. Stupakiewicz, C. Davies, K. Szerenos, D. Afanasiev, K. Rabinovich, A. Boris, A. Caviglia, A. Kimel, and A. Kirilyuk, "Ultrafast phononic switching of magnetization," *Nature Physics*, vol. 17, no. 4, pp. 489–492, 2021.

[110] C. Sirtori, "Bridge for the terahertz gap," *Nature*, vol. 417, no. 6885, pp. 132–133, 2002.

[111] D. Oepts, A. Van der Meer, and P. Van Amersfoort, "The free-electron-laser user facility felix," *Infrared Physics & Technology*, vol. 36, no. 1, pp. 297–308, 1995.

[112] Y.-R. Shen, "Principles of nonlinear optics," 1984.

[113] S. Baierl, M. Hohenleutner, T. Kampfrath, A. K. Zvezdin, A. V. Kimel, R. Huber, and R. V. Mikhaylovskiy, "Nonlinear spin control by terahertz-driven anisotropy fields," *Nature Photonics*, vol. 10, no. 11, pp. 715–718, 2016.

[114] T. Higuchi, N. Kanda, H. Tamaru, and M. Kuwata-Gonokami, "Selection rules for light-induced magnetization of a crystal with threefold symmetry: the case of antiferromagnetic nio," *Physical Review Letters*, vol. 106, no. 4, p. 047401, 2011.

[115] J. Nishitani, K. Kozuki, T. Nagashima, and M. Hangyo, "Terahertz radiation from coherent antiferromagnetic magnons excited by femtosecond laser pulses," *Applied Physics Letters*, vol. 96, no. 22, p. 221906, 2010.

[116] J. Nishitani, T. Nagashima, and M. Hangyo, "Coherent control of terahertz radiation from antiferromagnetic magnons in NiO excited by optical laser pulses," *Physical Review B*, vol. 85, no. 17, 2012.

[117] P. Bowlan, S. A. Trugman, D. A. Yarotski, A. J. Taylor, and R. P. Prasankumar, "Using ultrashort terahertz pulses to directly probe spin dynamics in insulating antiferromagnets," *Journal of Physics D: Applied Physics*, vol. 51, no. 19, p. 194003, 2018.

[118] J. H. Scofield, "Frequency-domain description of a lock-in amplifier," *American journal of physics*, vol. 62, no. 2, pp. 129–133, 1994.

[119] J. A. Fülöp, S. Tzortzakis, and T. Kampfrath, "Laser-driven strong-field terahertz sources," *Advanced Optical Materials*, vol. 8, no. 3, p. 1900681, 2020.

[120] T. Taniuchi and H. Nakanishi, "Collinear phase-matched terahertz-wave generation in GaP crystal using a dual-wavelength optical parametric oscillator," *Journal of Applied Physics*, vol. 95, no. 12, pp. 7588–7591, 2004.

[121] W. Zhang, H. Yu, H. Wu, and P. S. Halasyamani, "Phase-matching in nonlinear optical compounds: a materials perspective," *Chemistry of Materials*, vol. 29, no. 7, pp. 2655–2668, 2017.

[122] Y.-S. Lee, T. Meade, V. Perlin, H. Winful, T. B. Norris, and A. Galvanauskas, "Generation of narrow-band terahertz radiation via optical rectification of femtosecond pulses in periodically poled lithium niobate," *Applied Physics Letters*, vol. 76, no. 18, pp. 2505–2507, 2000.

[123] C. D. Mosley, D. S. Lake, D. M. Graham, S. P. Jamison, R. B. Appleby, G. Burt, and M. T. Hibberd, "Large-area periodically-poled lithium niobate wafer stacks optimized for high-energy narrowband terahertz generation," *Optics Express*, vol. 31, no. 3, pp. 4041–4054, 2023.

[124] J. Fülöp, L. Pálfalvi, G. Almási, and J. Hebling, "Design of high-energy terahertz sources based on optical rectification," *Optics Express*, vol. 18, no. 12, pp. 12311–12327, 2010.

[125] J. Hebling, A. Stepanov, G. Almási, B. Bartal, and J. Kuhl, "Tunable THz pulse generation by optical rectification of ultrashort laser pulses with tilted pulse fronts," *Applied Physics B*, vol. 78, pp. 593–599, 2004.

[126] U. Schlarb and K. Betzler, "Refractive indices of lithium niobate as a function of temperature, wavelength, and composition: A generalized fit," *Physical Review B*, vol. 48, no. 21, p. 15613, 1993.

[127] M. Unferdorben, Z. Szaller, I. Hajdara, J. Hebling, and L. Pálfalvi, "Measurement of refractive index and absorption coefficient of congruent and stoichiometric lithium niobate in the terahertz range," *Journal of Infrared, Millimeter, and Terahertz Waves*, vol. 36, pp. 1203–1209, 2015.

[128] J. Hebling, G. Almasi, I. Z. Kozma, and J. Kuhl, "Velocity matching by pulse front tilting for large-area THz-pulse generation," *Optics Express*, vol. 10, no. 21, pp. 1161–1166, 2002.

[129] L. Tokodi, J. Hebling, and L. Pálfalvi, "Optimization of the tilted-pulse-front terahertz excitation setup containing telescope," *Journal of Infrared, Millimeter, and Terahertz Waves*, vol. 38, pp. 22–32, 2017.

[130] H. Hirori, F. Blanchard, K. Tanaka, *et al.*, "Single-cycle terahertz pulses with amplitudes exceeding 1 MV/cm generated by optical rectification in $LiNbO_3$," *Applied Physics Letters*, vol. 98, no. 9, 2011.

[131] Y. Avestisyan, C. Zhang, I. Kawayama, H. Murakami, T. Somekawa, H. Chosrowjan, M. Fujita, and M. Tonouchi, "Terahertz generation by optical rectification in lithium niobate crystal using a shadow mask," *Optics Express*, vol. 20, no. 23, pp. 25752–25757, 2012.

[132] D. M. Slocum, E. J. Slingerland, R. H. Giles, and T. M. Goyette, "Atmospheric absorption of terahertz radiation and water vapor continuum effects," *Journal of Quantitative Spectroscopy and Radiative Transfer*, vol. 127, pp. 49–63, 2013.

[133] C. C. Davis, *Lasers and electro-optics: fundamentals and engineering*. Cambridge university press, 1996.

[134] M. R. Vaziri, F. Hajiesmaeilbaigi, and M. Maleki, "New ducting model for analyzing the gaussian beam propagation in nonlinear kerr media and its application to spatial self-phase modulations," *Journal of Optics*, vol. 15, no. 3, p. 035202, 2013.

[135] B. Wu, L. Cao, Q. Fu, P. Tan, Y. Xiong, *et al.*, "Comparison of the detection performance of three nonlinear crystals for the electro-optic sampling of a FEL-THz source," in *Proceedings of the 5th International Particle Accelerator Conference*, pp. 2891–2893, 2014.

[136] P. C. Planken, H.-K. Nienhuys, H. J. Bakker, and T. Wenckebach, "Measurement and calculation of the orientation dependence of terahertz pulse detection in znte," *JOSA B*, vol. 18, no. 3, pp. 313–317, 2001.

[137] S. Casalbuoni, H. Schlarb, B. Schmidt, P. Schmüser, B. Steffen, and A. Winter, "Numerical studies on the electro-optic detection of femtosecond electron bunches," *Physical Review Accelerators and Beams*, vol. 11, no. 7, p. 072802, 2008.

[138] N. Hekmat, T. Vogel, F. Meyer, A. Omar, Y. Wang, M. Hoffmann, and C. Saraceno, "Temperature-Dependent THz Refractive Index of GaP," in *2020 45th International*

Conference on Infrared, Millimeter, and Terahertz Waves (IRMMW-THz), pp. 1–2, IEEE, 2020.

[139] A. V. Chumak, A. A. Serga, and B. Hillebrands, "Magnon transistor for all-magnon data processing," *Nature Communications*, vol. 5, no. 1, p. 4700, 2014.

[140] K. Zakeri, "Terahertz magnonics: Feasibility of using terahertz magnons for information processing," *Physica C: Superconductivity and its applications*, vol. 549, pp. 164–170, 2018.

[141] V. Kruglyak and R. Hicken, "Magnonics: Experiment to prove the concept," *Journal of Magnetism and Magnetic Materials*, vol. 306, no. 2, pp. 191–194, 2006.

[142] V. Poimanov, A. Kuchko, and V. Kruglyak, "Magnetic interfaces as sources of coherent spin waves," *Physical Review B*, vol. 98, no. 10, p. 104418, 2018.

[143] R. Salikhov, I. Ilyakov, L. Körber, A. Kákay, R. A. Gallardo, A. Ponomaryov, J.-C. Deinert, T. V. de Oliveira, K. Lenz, J. Fassbender, *et al.*, "Coupling of terahertz light with nanometre-wavelength magnon modes via spin–orbit torque," *Nature Physics*, vol. 19, no. 4, pp. 529–535, 2023.

[144] A. Stupakiewicz, A. Maziewski, I. Davidenko, and V. Zablotskii, "Light-induced magnetic anisotropy in Co-doped garnet films," *Physical Review B*, vol. 64, no. 6, 2001.

[145] S. Kobayashi, Y. Hashimoto, and H. Munekata, "Investigation of an effective anisotropy field involved in photoinduced precession of magnetization in (Ga,Mn)As," *Journal of Applied Physics*, vol. 105, no. 7, 2009.

[146] J. H. Mentink, "Manipulating magnetism by ultrafast control of the exchange interaction," *Journal of Physics-Condensed Matter*, vol. 29, no. 45, 2017.

[147] R. R. Subkhangulov, A. B. Henriques, P. H. O. Rappl, E. Abramof, T. Rasing, and A. V. Kimel, "All-optical manipulation and probing of the d-f exchange interaction in EuTe," *Scientific Reports*, vol. 4, 2014.

[148] A. G. Gurevich and G. A. Melkov, *Magnetization oscillations and waves*. CRC press, 1996.

[149] R. Leenders and R. Mikhaylovskiy, "Theory of optical generation and detection of propagating magnons in an antiferromagnet," *Physical Review B*, vol. 107, no. 9, p. 094423, 2023.

[150] P. Gerevenkov, D. Kuntu, I. A. Filatov, L. Shelukhin, M. Wang, D. Pattnaik, A. Rushforth, A. Kalashnikova, and N. Khokhlov, "Effect of magnetic anisotropy relaxation on laser-induced magnetization precession in thin galfenol films," *Physical Review Materials*, vol. 5, no. 9, p. 094407, 2021.

[151] U. Happek, A. J. Sievers, and E. B. Blum, "Observation of Coherent Transition Radiation," *Physical Review Letters*, vol. 67, no. 21, pp. 2962–2965, 1991.

[152] K. Grishunin, E. Mashkovich, A. Kimel, A. Balbashov, and A. Zvezdin, "Excitation and detection of terahertz coherent spin waves in antiferromagnetic α- Fe_2O_3," *Physical Review B*, vol. 104, no. 2, p. 024419, 2021.

[153] X. Zeng, R. Wang, X. Xi, B. Li, and J. Zhou, "Terahertz rare-earth orthoferrite metamaterials by 3-D direct writing technology," *Optics Express*, vol. 26, no. 13, pp. 17056–17065, 2018.

[154] J. Nogues and I. K. Schuller, "Exchange bias," *Journal of Magnetism and Magnetic Materials*, vol. 192, no. 2, pp. 203–232, 1999.

[155] J. Tang, Y. J. Ke, W. He, X. Q. Zhang, W. Zhang, N. Li, Y. S. Zhang, Y. Li, and Z. H. Cheng, "Ultrafast Photoinduced Multimode Antiferromagnetic Spin Dynamics in Exchange-Coupled Fe/$RFeO_3$ (R = Er or Dy) Heterostructures," *Advanced Materials*, vol. 30, no. 27, 2018.

[156] C. Thomsen, H. T. Grahn, H. J. Maris, and J. Tauc, "Surface generation and detection of phonons by picosecond light pulses," *Physical Review B*, vol. 34, no. 6, p. 4129, 1986.

[157] C. E. Bottani and D. Fioretto, "Brillouin scattering of phonons in complex materials," *Advances in Physics: X*, vol. 3, no. 1, p. 1467281, 2018.

[158] C. Sandweg, M. Jungfleisch, V. Vasyuchka, A. Serga, P. Clausen, H. Schultheiss, B. Hillebrands, A. Kreisel, and P. Kopietz, "Wide-range wavevector selectivity of magnon gases in brillouin light scattering spectroscopy," *Review of Scientific Instruments*, vol. 81, no. 7, 2010.

[159] A. Kimel, B. Ivanov, R. Pisarev, P. Usachev, A. Kirilyuk, and T. Rasing, "Inertia-driven spin switching in antiferromagnets," *Nature Physics*, vol. 5, no. 10, pp. 727–731, 2009.

[160] Z. Habib, K. Majid, M. Ikram, K. Sultan, S. A. Mir, and K. Asokan, "Influence of ni substitution at B-site for Fe^{3+} ions on morphological, optical, and magnetic properties of $HoFeO_3$ ceramics," *Applied Physics A*, vol. 122, pp. 1–8, 2016.

[161] F. J. Kahn, P. S. Pershan, and J. P. Remeika, "Ultraviolet Magneto-Optical Properties of Single-Crystal Orthoferrites, Garnets, and Other Ferric Oxide Compounds," *Physical Review*, vol. 186, no. 3, pp. 891–918, 1969.

[162] D. Peceli, S. Webster, D. A. Fishman, C. M. Cirloganu, H. Hu, O. V. Przhonska, V. V. Kurdyukov, Y. L. Slominsky, A. I. Tolmachev, A. D. Kachkovski, *et al.*, "Optimization of the Double Pump-Probe Technique: Decoupling the Triplet Yield and Cross Section," *The Journal of Physical Chemistry A*, vol. 116, no. 20, pp. 4833–4841, 2012.

[163] A. Kamimaki, S. Iihama, K. Suzuki, N. Yoshinaga, and S. Mizukami, "Parametric amplification of magnons in synthetic antiferromagnets," *Physical Review Applied*, vol. 13, no. 4, p. 044036, 2020.

[164] X. Li, M. Bamba, N. Yuan, Q. Zhang, Y. Zhao, M. Xiang, K. Xu, Z. Jin, W. Ren, G. Ma, *et al.*, "Observation of Dicke cooperativity in magnetic interactions," *Science*, vol. 361, no. 6404, pp. 794–797, 2018.

[165] T. Makihara, K. Hayashida, G. T. Noe Ii, X. Li, N. Marquez Peraca, X. Ma, Z. Jin, W. Ren, G. Ma, I. Katayama, *et al.*, "Ultrastrong magnon–magnon coupling dominated by antiresonant interactions," *Nature Communications*, vol. 12, no. 1, p. 3115, 2021.

[166] J. Lu, X. Li, H. Y. Hwang, B. K. Ofori-Okai, T. Kurihara, T. Suemoto, and K. A. Nelson, "Coherent two-dimensional terahertz magnetic resonance spectroscopy of collective spin waves," *Physical Review Letters*, vol. 118, no. 20, p. 207204, 2017.

[167] M. Liu, H. Y. Hwang, H. Tao, A. C. Strikwerda, K. Fan, G. R. Keiser, A. J. Sternbach, K. G. West, S. Kittiwatanakul, J. Lu, *et al.*, "Terahertz-field-induced insulator-to-metal transition in vanadium dioxide metamaterial," *Nature*, vol. 487, no. 7407, pp. 345–348, 2012.

[168] S. Schlauderer, C. Lange, S. Baierl, T. Ebnet, C. P. Schmid, D. Valovcin, A. Zvezdin, A. Kimel, R. Mikhaylovskiy, and R. Huber, "Temporal and spectral fingerprints of ultrafast all-coherent spin switching," *Nature*, vol. 569, no. 7756, pp. 383–387, 2019.

[169] Y. B. Bazaliy, L. Tsymbal, G. Kakazei, A. Izotov, and P. Wigen, "Spin-reorientation in $ErFeO_3$: Zero-field transitions, three-dimensional phase diagram, and anisotropy of erbium magnetism," *Physical Review B*, vol. 69, no. 10, p. 104429, 2004.

[170] K. Zhang, K. Xu, X. Liu, Z. Zhang, Z. Jin, X. Lin, B. Li, S. Cao, and G. Ma, "Resolving the spin reorientation and crystal-field transitions in $TmFeO_3$ with terahertz transient," *Scientific Reports*, vol. 6, no. 1, p. 23648, 2016.

[171] V. Khmara, N. Kovtun, and G. Troitskii, "Spin configuration of $ErFeO_3$ below the ordering temperature of erbium," *Solid State Communications*, vol. 15, no. 11-12, pp. 1769–1771, 1974.

[172] J. Leake, G. Shirane, and J. Remeika, "The magnetic structure of thulium orthoferrite, $TmFeO_3$," *Solid State Communications*, vol. 6, no. 1, pp. 15–17, 1968.

[173] V. D. Buchel'nikov, N. Dan'shin, L. Tsymbal, and V. G. Shavrov, "Magnetoacoustics of rare-earth orthoferrites," *Physics-Uspekhi*, vol. 39, no. 6, p. 547, 1996.

[174] J. De Jong, A. Kimel, R. Pisarev, A. Kirilyuk, and T. Rasing, "Laser-induced ultrafast spin dynamics in $ErFeO_3$," *Physical Review B*, vol. 84, no. 10, p. 104421, 2011.

[175] J. M. Coey, *Magnetism and magnetic materials*. Cambridge university press, 2010.

[176] R. Mikhaylovskiy, T. Huisman, R. Pisarev, T. Rasing, and A. Kimel, "Selective excitation of terahertz magnetic and electric dipoles in Er^{3+} ions by femtosecond laser pulses in $erfeo_3$," *Physical Review Letters*, vol. 118, no. 1, p. 017205, 2017.

[177] R. V. Mikhaylovskiy, E. Hendry, V. V. Kruglyak, R. V. Pisarev, T. Rasing, and A. V. Kimel, "Terahertz emission spectroscopy of laser-induced spin dynamics in $TmFeO_3$ and $ErFeO_3$ orthoferrites," *Physical Review B*, vol. 90, no. 18, p. 184405, 2014.

[178] M. Hudl, M. d'Aquino, M. Pancaldi, S.-H. Yang, M. G. Samant, S. S. Parkin, H. A. Dürr, C. Serpico, M. C. Hoffmann, and S. Bonetti, "Nonlinear magnetization dynamics driven by strong terahertz fields," *Physical Review Letters*, vol. 123, no. 19, p. 197204, 2019.

[179] Z. Zhang, F. Sekiguchi, T. Moriyama, S. C. Furuya, M. Sato, T. Satoh, Y. Mukai, K. Tanaka, T. Yamamoto, H. Kageyama, *et al.*, "Generation of third-harmonic spin oscillation from strong spin precession induced by terahertz magnetic near fields," *Nature Communications*, vol. 14, no. 1, p. 1795, 2023.

[180] T. Kurihara, M. Bamba, H. Watanabe, M. Nakajima, and T. Suemoto, "Observation of terahertz-induced dynamical spin canting in orthoferrite magnon by magnetorefractive probing," *Communications Physics*, vol. 6, no. 1, p. 51, 2023.

[181] M. Bamba, X. Li, N. Marquez Peraca, and J. Kono, "Magnonic superradiant phase transition," *Communications Physics*, vol. 5, no. 1, p. 3, 2022.

[182] A. Balbashov, G. Kozlov, S. Lebedev, A. Mukhin, A. Y. Pronin, and A. Prokhorov, "Anomalies of high-frequency magnetic properties and new orientational transitions in $HoFeO_3$," *Zhurnal Eksperimental'noi i Teoreticheskoi Fiziki*, vol. 95, no. 3, pp. 1092–1107, 1989.

[183] G. Ju, J. Hohlfeld, B. Bergman, R. J. van de Veerdonk, O. N. Mryasov, J.-Y. Kim, X. Wu, D. Weller, and B. Koopmans, "Ultrafast generation of ferromagnetic order via a laser-induced phase transformation in FeRh thin films," *Physical Review Letters*, vol. 93, no. 19, p. 197403, 2004.

[184] R. Medapalli, G. Li, S. K. Patel, R. Mikhaylovskiy, T. Rasing, A. Kimel, and E. Fullerton, "Femtosecond photocurrents at the FeRh/Pt interface," *Applied Physics Letters*, vol. 117, no. 14, 2020.

[185] G. Li, R. Medapalli, J. Mentink, R. Mikhaylovskiy, T. Blank, S. Patel, A. Zvezdin, T. Rasing, E. Fullerton, and A. Kimel, "Ultrafast kinetics of the antiferromagnetic-ferromagnetic phase transition in FeRh," *Nature Communications*, vol. 13, no. 1, p. 2998, 2022.

[186] K. Kang, H. Omura, D. Yesudas, O. Lee, K.-J. Lee, H.-W. Lee, T. Taniyama, and G.-M. Choi, "Spin current driven by ultrafast magnetization of FeRh," *Nature Communications*, vol. 14, no. 1, p. 3619, 2023.

[187] T. Usami, M. Itoh, and T. Taniyama, "Temperature dependence of the effective Gilbert damping constant of FeRh thin films," *AIP Advances*, vol. 11, no. 4, 2021.